THE UNIVERSITY of ADELAIDE

Regional high-grade metamorphism during rift basin development: implications for burial mechanisms to lower crustal depths

Thesis submitted in accordance with the requirements of the University of Adelaide for an Honours Degree in Geology

Naomi Marie Tucker

November 2013

REGIONAL HIGH-GRADE METAMORPHISM DURING RIFT BASIN DEVELOPMENT: IMPLICATIONS FOR BURIAL MECHANISMS TO LOWER CRUSTAL DEPTHS

RUNNING TITLE: HIGH-GRADE METAMORPHISM DURING BASIN DEVELOPMENT

ABSTRACT

Crustal-scale exhumation during the intraplate Alice Springs Orogeny (c. 450–300 Ma) in central Australia has exposed the medium-pressure, high-grade metasedimentary and metabasaltic rocks of the Harts Range Group (HRG). Similarities in the detrital zircon age spectra and Lu–Hf-isotopic composition between the HRG and surrounding unmetamorphosed late Neoproterozoic–Cambrian Amadeus and Georgina basin sequences indicate the HRG is a highly metamorphosed equivalent to these basin successions. Calculated phase equilibria modelling and thermobarometry constrain peak metamorphic conditions to ~880ºC and 10.5 kbar and ~670ºC and 7 kbar in the structurally lowest and highest parts of the HRG, respectively. Peak metamorphic assemblages are associated with extensive mafic magmatism, a coarse layer-parallel fabric and NE-side-down kinematics, the combination of which points to an extensional setting. Metamorphic conditions indicate a high geothermal gradient regime also existed during burial, manifested by the prograde development of andausite-bearing metapelite mineral assemblages. Monazite within prograde-zoned garnet and the enclosing fabric yield a U–Pb age of c. 442 Ma which is interpreted to record the timing of high-grade metamorphism of the upper HRG during continuation of the late Ordovician Larapinta Event (c. 480–460 Ma). Burial and metamorphism was synchronous with Centralian Superbasin sedimentation in central Australia and accordingly the deep burial, metamorphism and deformation of the HRG to mid-lower crustal depths must be justified in the context of the broader intraplate basin evolution. The HRG seems consistent with burial by sediment loading and associated high-grade metamorphism driven by elevated heat flows in a super-deep rift. This suggests that regional medium-pressure, high-grade metamorphic terranes may be generated in deep intraplate rift basins during extension and therefore are not necessarily reflective of compressional thickening of the crust.

KEYWORDS

Deep-rift basin; intraplate deformation; regional high-grade metamorphism; zircon provenance; geochronology; Lu–Hf; pseudosection; Harts Range; Ordovician

Table of Contents

LIST OF FIGURES AND TABLES

1. INTRODUCTION

Deep burial of supracrustal sedimentary successions to mid-lower crustal depths (~25–30 km) is generally regarded as reflecting crustal thickening by large-scale compressional tectonism (Brown 1993; Friedmann and Burbank 1995; Brown 2001; Jamieson *et al.* 2002). In the absence of well-defined constraints on the palaeogeography and palaeotectonic regime, the occurrence of moderate–high pressure granulite-facies terranes are often used to suggest deep burial in a compressional tectonic setting (Robinson and Bevins 1989; Brown 1993; Vance *et al.* 1998; Clarke *et al.* 2000; Jamieson *et al.* 2002; Tam *et al.* 2012). However, deep burial of sedimentary successions can also potentially occur within sedimentary basins. In particular, deep rift basins are a logical setting for the occurrence of regional medium-pressure high-temperature metamorphism as they are commonly associated with high basal heat flows as well as magmatism (Wickham and Oxburgh 1985; Sandiford and Powell 1986; Thompson and Gibson 1994; Friedmann and Burbank 1995; Ruppel 1995; Corti *et al.* 2003).

There are a number of examples in which more than 20 km of burial has occurred within well-recognised and preserved crustal-scale rift-style basins including the late Mesoproterozoic Midcontinent Rift System in north America (Allen *et al.* 1995), the Palaeozoic Dneiper-Donets Basin located in eastern Europe (Starostenko *et al.* 1999), the Devonian–Holocene-aged Petrel Sub-basin located offshore north-western Australia (Baldwin *et al.* 2003), and the Baikal Rift system in north Asia (Puzyrev *et al.* 1978). Super-deep basins exhibit a distinctive V-shape morphology in plan view, have evidence for large amounts of localised extension, a prominent structural half-graben

asymmetry, and trend at a high angle adjacent oceanic and orogenic margins (Busby and Ingersoll 1995; Baldwin *et al.* 2003). Generally, extension is localised to long (50–100 km) and narrow (20–40 km) intracratonic depocentres hosted in larger basins within comparatively thermally stable continental lithosphere (Friedmann and Burbank 1995; Baldwin *et al.* 2003; Corti *et al.* 2003; Jolivet *et al.* 2012). The Arunta region, central Australia, may also preserve evidence for granulite-facies metamorphism in a deep-rift basin.

The Arunta region is host to a Paleoproterozoic–Paleozoic (c. 1900–300 Ma) high-grade metamorphic complex that constitutes the southern margin of the North Australian Craton (Collins and Shaw 1995; Scrimgeour *et al.* 2005; Morrissey *et al.* 2011). Until recently it had been accepted that all high-grade metamorphosed rocks within the Arunta region have Palaeo–Mesoproterozoic-aged protoliths and all mid-lower crustal rocks exhumed during the mid-Palaeozoic Alice Springs Orogeny (ASO) formed part of the basement to the Neoproterozoic–mid Palaeozoic Centralian Superbasin. Moreover, metamorphism of the Centralian Superbasin units was considered at most greenschist-facies (Shaw *et al.* 1991; Collins and Shaw 1995; Sandiford *et al.* 2001; Raimondo *et al.* 2011). However, discovery of early Ordovician (c. 480–460 Ma) medium-pressure granulite-facies metamorphism in the Harts Range Group (HRG) in the eastern Arunta region has forced a reassessment of the Palaeozoic tectonic evolution of central Australia (Hand *et al.* 1999; Mawby *et al.* 1999; Buick *et al.* 2001; Maidment *et al.* 2013). Furthermore, depositional ages and detrital zircon provenance of the protoliths to these high-grade metasedimentary rocks share strong similarities with the widespread late Neoproterozoic–Cambrian-aged sedimentary successions of the adjacent unmetamorphosed Amadeus and Georgina basins (Fig. 1; Buick *et al.* 2001; Buick *et al.*

2005; Maidment *et al.* 2013). This suggests that the HRG may be the high-grade correlative of the Centralian Superbasin sequences that are preserved in the Amadeus and Georgina basins (Buick *et al.* 2005; Buick *et al.* 2008; Maidment *et al.* 2013). If this is the case, then deep burial, metamorphism and deformation of the HRG to mid-lower crustal depths must be understood in the context of evolution of the broader basin system at this time.

This study firstly aims to provide a more robust comparison of detrital zircon age data from select units of the HRG, and Amadeus and Georgina basins to conclude whether these sequences are indeed correlatives as previously proposed by visual comparisons alone (Maidment *et al.* 2013). This is combined with structural and lithological mapping to search for direct evidence of extensional deformation, and geochronology and thermodynamic modelling of metamorphic mineral assemblages to place temporal and qualitative constraints on the metamorphic architecture of the Harts Range. This will enable assessment of the viability of sedimentary burial leading to medium-pressure, high-grade metamorphism that is otherwise considered to represent compressional orogenesis. Results from this study potentially have significant implications for the tectonic interpretation of medium-pressure, high-grade metamorphism where a palaeogeographic context is lacking.

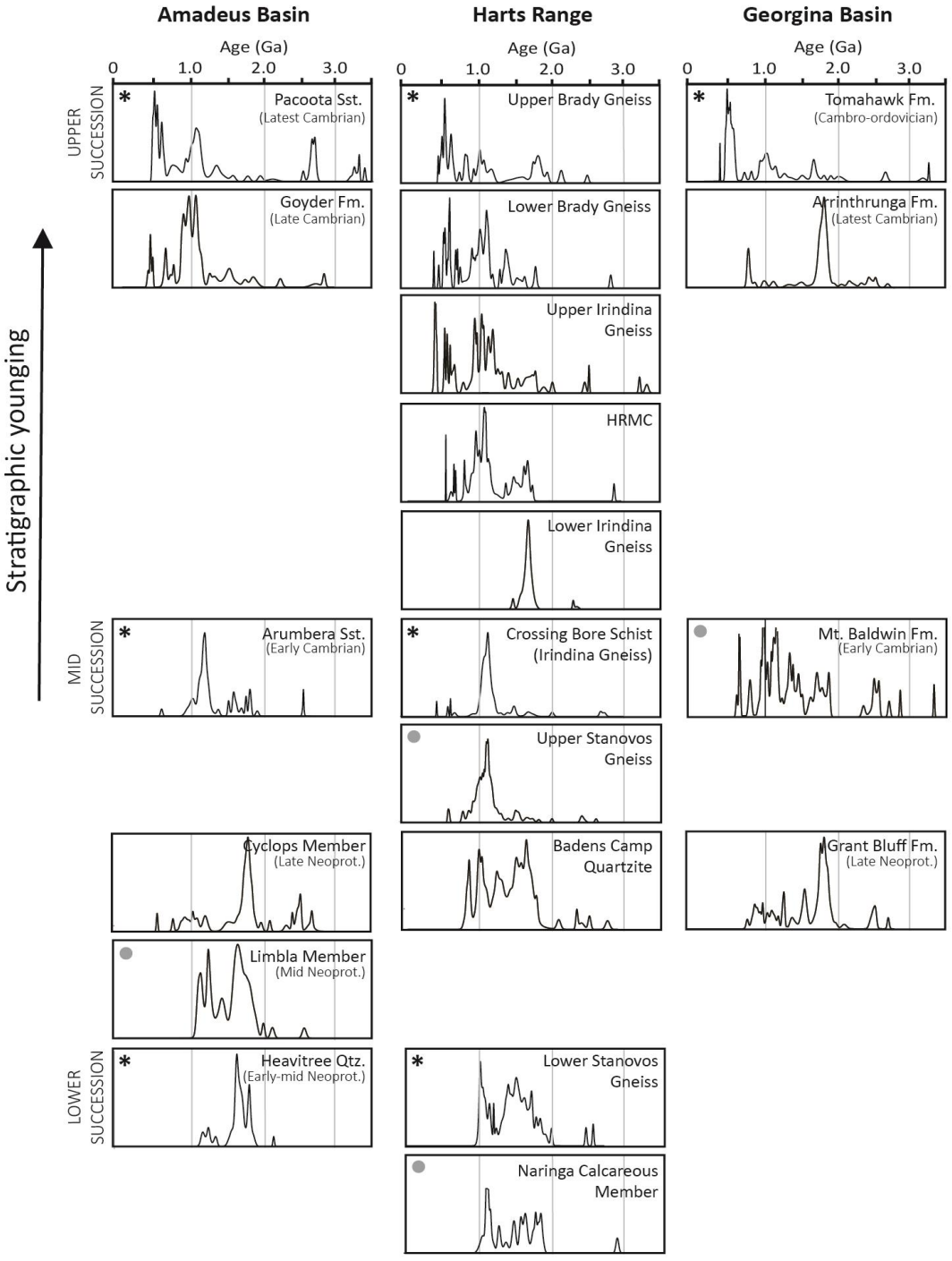

Figure 1. Relative probability density plots of detrital zircon U–Pb age data from metasedimentary rocks of the Harts Range and select Neoproterozoic–Palaeozoic sedimentary units of the NE Amadeus and SW Georgina basins. The Y-axis of each plot indicates the relative probability density; the X-axis represents age (Ga). Visual inspection reflects temporal similarities between the age of metamorphosed and unmetamorphosed units of the three successions. Units from the upper, mid and lower parts of the three successions which compare particulaily strongly are inferred stratigraphic correlatives (Maidment *et al.* 2013) – Upper Brady Gneiss, Pacoota Sandstone and Tomahawk Formation (upper); Crossing Bore Schist and Arumbera Sandstone (mid); and, Lower Stanovos Gneiss and Heavitree Quartzite (lower), and are marked with an asterisk. These units have been selected for zircon Hf-isotopic analyses and comparative age modelling in this study. Units marked with a grey circle are also used for comparative modelling. Image modified from Maidment *et al.* (2013). Age data are sourced from Maidment *et al.* (2013), Maidment *et al.* (2007) and Buick *et al.* (2005).

2. GEOLOGICAL BACKGROUND

2.1. Regional geology

The Harts Range is located in the southeastern Arunta region, approximately 150 km north-east of Alice Springs, central Australia (Fig. 2). The HRG is a localised supracrustal terrane of amphibolite–granulite-grade metasedimentary and metabasaltic rocks (Hand *et al.* 1999; Mawby *et al.* 1999; Buick *et al.* 2005; Maidment *et al.* 2013). It structurally overlies the Palaeoproterozoic-aged crystalline basement rocks of the Bruna Gneiss (1747 ± 2 Ma, Cooper *et al.* 1988) and Entia Gneiss Complex (1800–1730 Ma) which outcrop to the east of the region as the Entia Dome, and are an extension to the Palaeoproterozoic granulite-grade Strangways Metamorphic Complex to the west (Buick *et al.* 2008; Maidment *et al.* 2013). The HRG is bordered to the south and north by the Neoproterozoic to mid-Palaeozoic (c. 900–300 Ma) intractratonic Amadeus and Georgina basins, respectively, which also unconformably overly the Arunta basement, and are structural remnants of the formerly more extensive Centralian Superbasin (Shaw *et al.* 1991; Buick *et al.* 2005). The HRG consists of five lithostratigraphic units which are in structural contact (Maidment *et al.* 2013). The structurally lowermost unit comprises the metapelitic Irindina Gneiss, including three basal subdivisions - the Naringa Calcareous Member, Stanovos Gneiss Member and the Harts Range Meta-Igneous Complex (HRMC; Buick *et al.* 2005; Buick *et al.* 2008; Maidment *et al.* 2013). The HRMC consists of laterally voluminous migmatitic amphibolite and comagmatic anorthosite (centimetre-scale to 2 km) derived from basaltic-volcaniclastic precursors in an inferred intraplate rift setting (Sivell and Foden 1985; Sivell 1988). The structurally highest unit in the Harts Range area is the Brady Gneiss which is further divided into

lower metapelitic and upper calc-silicate subunits (Buick *et al.* 2005; Maidment *et al.* 2013).

Peak metamorphism occurred during the Ordovician Larapinta Event (c. 480–460 Ma; Hand *et al.* 1999; Mawby *et al.* 1999; Buick *et al.* 2001). Granulite-facies metamorphism was associated with partial melting, a pervasive layer-parallel foliation and coarse migmatitic assemblages comprised of garnet–clinopyroxene leucosomes in HRMC mafic granulite, and coarse garnet-bearing tonalitic leucosomes within metapelite (Hand *et al.* 1999; Mawby *et al.* 1999; Maidment *et al.* 2013). Peak metamorphic conditions were 9–10 kbar and 800–850ºC in the structurally lowest parts of the sequence (Oliver *et al.* 1988; Mawby *et al.* 1999; Buick *et al.* 2001) implying burial to ~30 km (Maidment *et al.* 2013). Palaeogeographical reconstructions indicate that the HRG was located at least 500 km from the eastern Australian continental margin at this time (Maidment *et al.* 2013) beneath the narrow E-W trending epicontinental Larapintine Seaway that spanned most of central Australia, and the broader shallow marine Centralian Superbasin (Webby 1978; Buick *et al.* 2005; Haines and Wingate 2007).

The present tectonic architecture of the Harts Range region is largely the consequence of the c. 450–300 Ma intraplate ASO (Flottmann and Hand 1999; Hand *et al.* 1999; Raimondo *et al.* 2011; Maidment *et al.* 2013) which exhumed the HRG and adjoining Palaeoproterozoic Arunta basement from mid-lower crustal depths (<20 km), and inverted the northeastern section of the overlying intraplate Centralian Superbasin (Collins and Teyssier 1989; Korsch and Lindsay 1989; Sandiford and Hand 1998; Sandiford *et al.* 2001). Earliest evidence for convergence linked to the ASO is found in

the HRG with reworking of Ordovician-aged structures by regional-scale shear zones and top-to-the-south thrusting (Collins and Shaw 1995; Mawby *et al.* 1999; Haines *et al.* 2001), and local emplacement of pegmatites (Buick *et al.* 2008). Despite intense deformation, the HRG remained largely in its original stratigraphic order and preserves a present-day structural thickness of ~6–7 km (Buick *et al.* 2005; Maidment *et al.* 2013).

2.2. Study area

This study focuses on a region in the northern Harts Range. This area encompasses an inferred northeastward-younging section (Maidment *et al.* 2013) from basement contact with the HRMC and metapelitic Irindina Gneiss to the Upper Brady Gneiss, approximately 2.5 km south-southwest of Atijere in the Harts Range (Fig. 2). This field location was selected to examine a sequence of key units within the HRG, determine the structural and lithological relationships, and to identify rocks suitable for metamorphic analysis. A summary of samples and sampling localities is provided in Appendix A. A geological map of the study area is shown in Figure 3 with accompanying lithological descriptions summarised in Table 1.

2.2.1. STRUCTURAL ARCHITECTURE

Structural data reflect the pervasively moderate N–NE dipping foliation and NW–NE trending lineation (Fig. 3). Peak metamorphic assemblages are associated with a poorly-lineated, coarse migmatitic fabric (S1) defined by hornblende–plagioclase ± clinopyroxene in mafic granulite and biotite ± sillimanite in metapelite which grossly parallels the lithological layering. The S1 fabric is locally cross-cut by leucosome segregations containing the peak mineral assemblages in mafic granulites, which

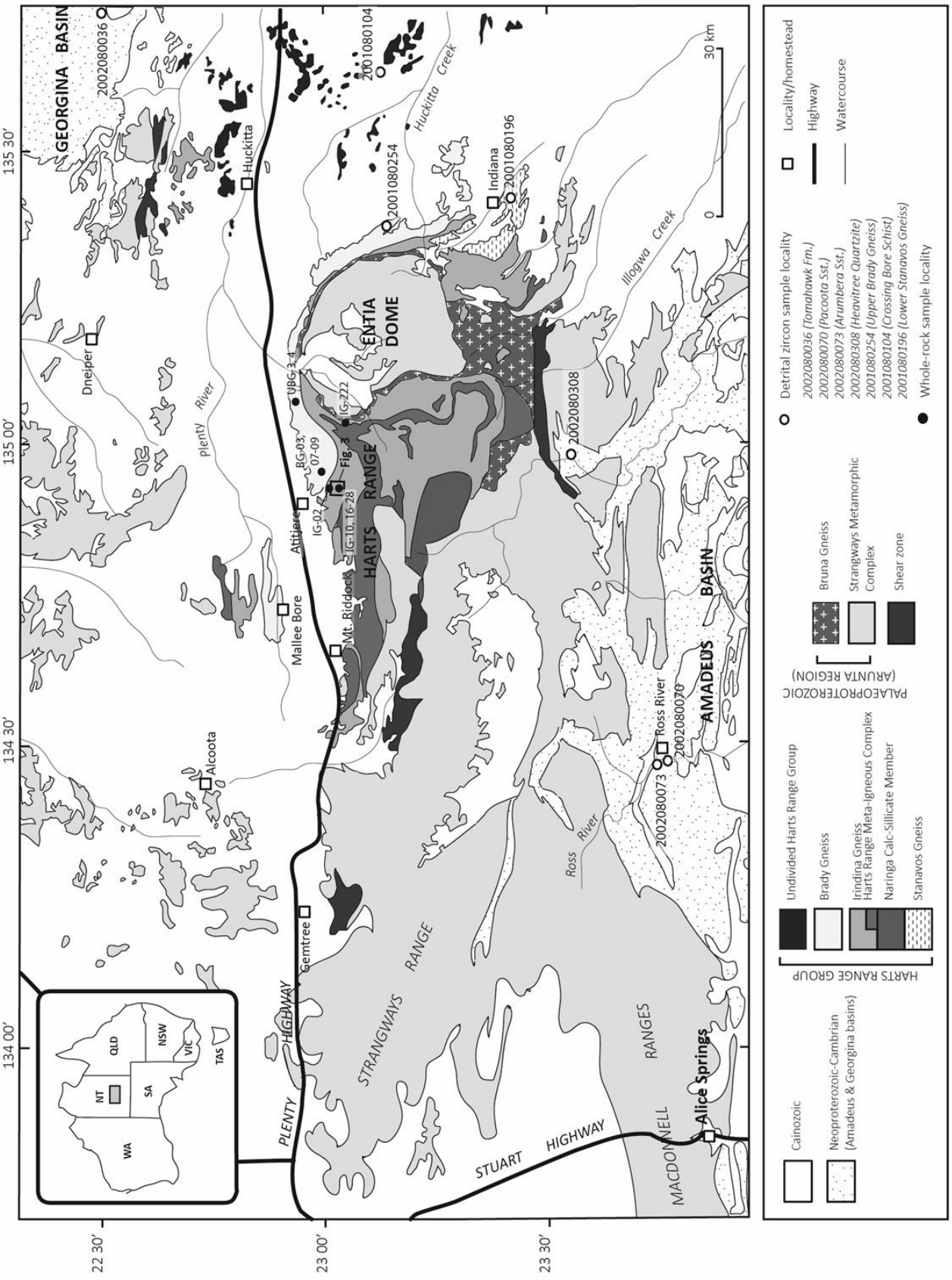

Figure 2. Regional geological map of the Harts Range region and surrounding areas
Locations of samples discussed in this study are shown. Sample number grid references are provided in Appendix A. The study area (Fig. 3) is defined by the small boxed region approximately 5 km south of Atijere community. Image modified from Maidment *et al.* (2013) and Maidment *et al.* (2005).

otherwise align with the fabric. Overprinting S2 and S3 fabrics are approximately co-planar with S1. S2 is characterised by a moderately NW–NE-wards dipping granoblastic fabric and a weakly preserved N–S trending lineation. S2 is distinguished from S1 by the presence of structurally reworked peak metamorphic segregations and locally well-defined NE-side-down normal shear sense kinematics observed parallel to L2 (Fig. 4k). In contrast, S3 is characterised by a moderate NW–NE-wards dipping mylonitic foliation (S3), a much more intensely defined N–S trending lineation (L3) and preservation of well-defined top-to-SW kinematics (Fig. 4l). The mapping area is dissected by pegmatite and coarse-grained leucogneiss units that trend NE–SW and NW–SE and reflect at least three generations of partial melting during the ASO (Buick *et al.* 2008).

2.2.2. FIELD-BASED METAMORPHIC GEOLOGY

The rocks in the selected field area are highly metamorphosed amphibolite- to granulite-facies migmatitic gneisses of the Irindina Gneiss which are increasingly interleaved to the SW with laterally extensive amphibolite horizons and coarse mafic granulite collectively termed the HRMC. Plagioclase-phyric and equigranular hornblende–plagioclase amphibolite define the abundant mafic dykes which are present through the entire area, but are not distinguishable as separate lithologies at the mapped scale (Fig. 4g–i). These dykes both parallel and cross-cut the S1 and S2 foliations. Domains of stromatic diatexite are prevalent within the migmatitic gneisses in the central and northern part of the mapped region (Fig. 4f).

Units in the southwestern third of the area are reworked mylonitic garnet–biotite ± sillimanite-bearing metapelite and retrogressed orthopyroxene-bearing amphibolite.

SHRIMP U–Pb zircon dating (Barnes 2013) indicates that these are most likely part of the Palaeoproterozoic (c. 1.78–1.71 Ga) Strangways basement (Maidment *et al.* 2005). Associated with the inferred basement units is a c. 1745 Ma (Barnes 2013) megacrystic augen gneiss.

Peak mafic granulite mineral assemblages are defined by garnet–clinopyroxene-bearing tonalitic leucosomes (garnet up to 15 cm) formed by partial melting of earlier hornblende–plagioclase assemblages (Fig. 4a & b) via the reaction:

(Eq. 1, Mawby *et al.* 1999)

hornblende + plagioclase + quartz → garnet ± clinoproxene + tonalitic melt

Reaction textures between garnet and clinopyroxene forming coarse hornblende–plagioclase assemblages in some peak metamorphic segregations implies a reversal of this reaction in an approximately isochemical migmatitic system.

In metapelite, the peak assemblage is defined by garnet-bearing leucosomes (garnet up to 8 cm) interlayered with garnet–biotite ± sillimanite gneiss (Fig. 4d). Locally, sillimanite occurs in subhedral blocky aggregates (1.5–5 cm, Fig. 4c). These are interpreted to reflect the former prescence of andalusite, now pseudomorphed by sillimanite.

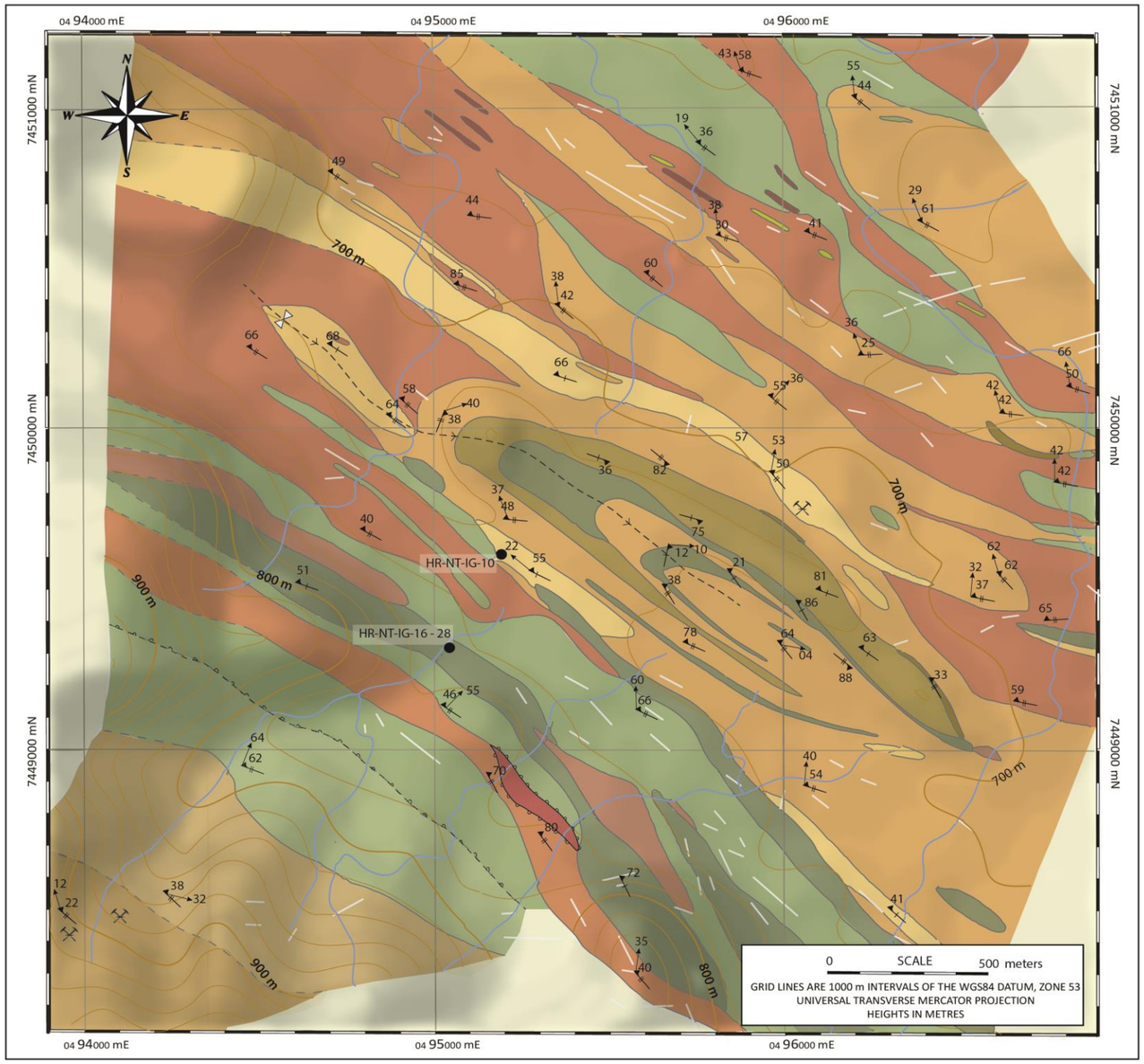

LITHOLOGICAL UNITS

- Tremolite alteration zone
- Pegmatite
- Coarse-grained leucogneiss

Harts Range Group

Irindina Gneiss Metapelite

- Quartzo-feldspathic garnet-biotite migmatitic gneiss; coarse garnet (generally <2 cm) constitutes >15% rock
- Garnetiferous garnet-biotite-sillimanite (after andalusite) migmatitic gneiss; very coarse garnet (1-8 cm) constitutes >20% rock

Stromatic diatexite - layer-parallel leucocratic-pegmatitic melt segregations intermingled with >15% mafic (amphibolite) component

- Metapelitic diatexite (>50% metapelite component)
- Mafic diatexite (>50% mafic granulite component)
- Felsic diatexite (>50% gneissic granitoid component)

Riddock Amphibolite - Harts Range Metaigneous Complex

- Coarse-grained garnet-clinopyroxene-hornblende-plagioclase (mafic) granulite
- Coarse hornblende-plagioclase amphibolite
- Very coarse-grained hornblende-plagioclase amphibolite
- Retrogressed hornblendite (chlorite after orthopyroxene?)

Basement (Strangways Metamorphic Complex)

- Megacrystic gneissic granitoid (Bruna Gneiss)
- Coarse amphibolite with retrogressed orthopyroxene
- Sub-mylonitised migmatitic garnetiferous gneiss with significant mafic dyke component (constituting 15-60% area, and decreasing gradationally towards SW)
- Sub-mylonitised migmatitic garnetiferous gneiss with minor mafic dyke component (<15%)
- Area not mapped

GEOLOGICAL & TOPOGRAPHICAL SYMBOLS

- Lithological boundary - identity and existence certain, location approximate
- Lithological boundary - identity and existance certain, location inferred
- Unconformable contact - identity and existance certain, location approximate
- Inferred unconformable contact - identity and existance inferred, location approximate
- Inferred synform - existence and location inferred, showing inferred plunge direction

Inclined (dip direction to right) metamorphic or tectonic foliation - showing strike and dip

- 35 S1 foliation - coarse foliation, no obvious associated lineation
- 35 S2 foliation - coarse foliation; associated NE-side down (vertical section) and dextral (horizontal) kinematics
- 35 S3 foliation - moderately-coarse foliation; associated N/NE-SE trending lineation and locally top-to-SW kinematics
- 12 Mineral stretching lineation - showing bearing and plunge
- Mine, open pit or glory hole; minor, abandoned
- Watercourse, seasonal/intermittent
- 700 m Topographic contour interval, height in metres

STEREOGRAPHIC PROJECTIONS OF STRUCTURAL DATA

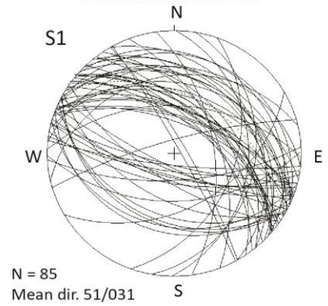

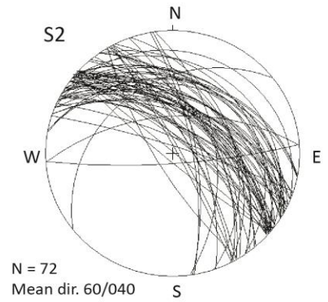

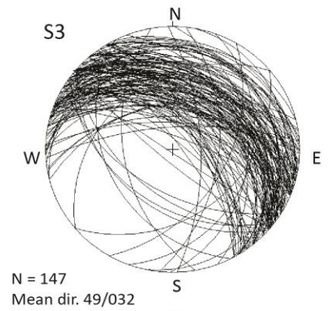

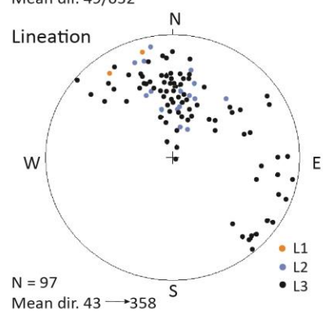

Figure 3. Simplified geological map of the study area

The field area is located between the former *Disputed Mine* to the far SW and *Brett Creek* towards the NNE, Harts Range, central Australia. The area incompasses an inferred northeast-younging section (Maidment *et al*. 2013) from basement contact with the Harts Range Meta-Igneous Complex and metapelitic Irindina Gneiss to the boundary with Brady Gneiss (approximately 1 km to the NNE). Grid references refer to WGS84 datum (Zone 53k) and UTM coordinates. The geological map has been overlaid on a terrain image to reflect the topographic relief and topographic contours are also shown. Accompanying lithological descriptions are provided in Table 1. Sampling localities from within the mapping area are shown with all sample locality coordinates also provided in Appendix A. Structural data are represented on stereonets in which the dip and dip-direction of S1–S3 foliations (refer to text) are plotted as great circles, and the dip and plunge-direction of lineations plot as points. Structural data reflect a pervasively moderate NNE dipping foliation and NW–NE trending lineation.

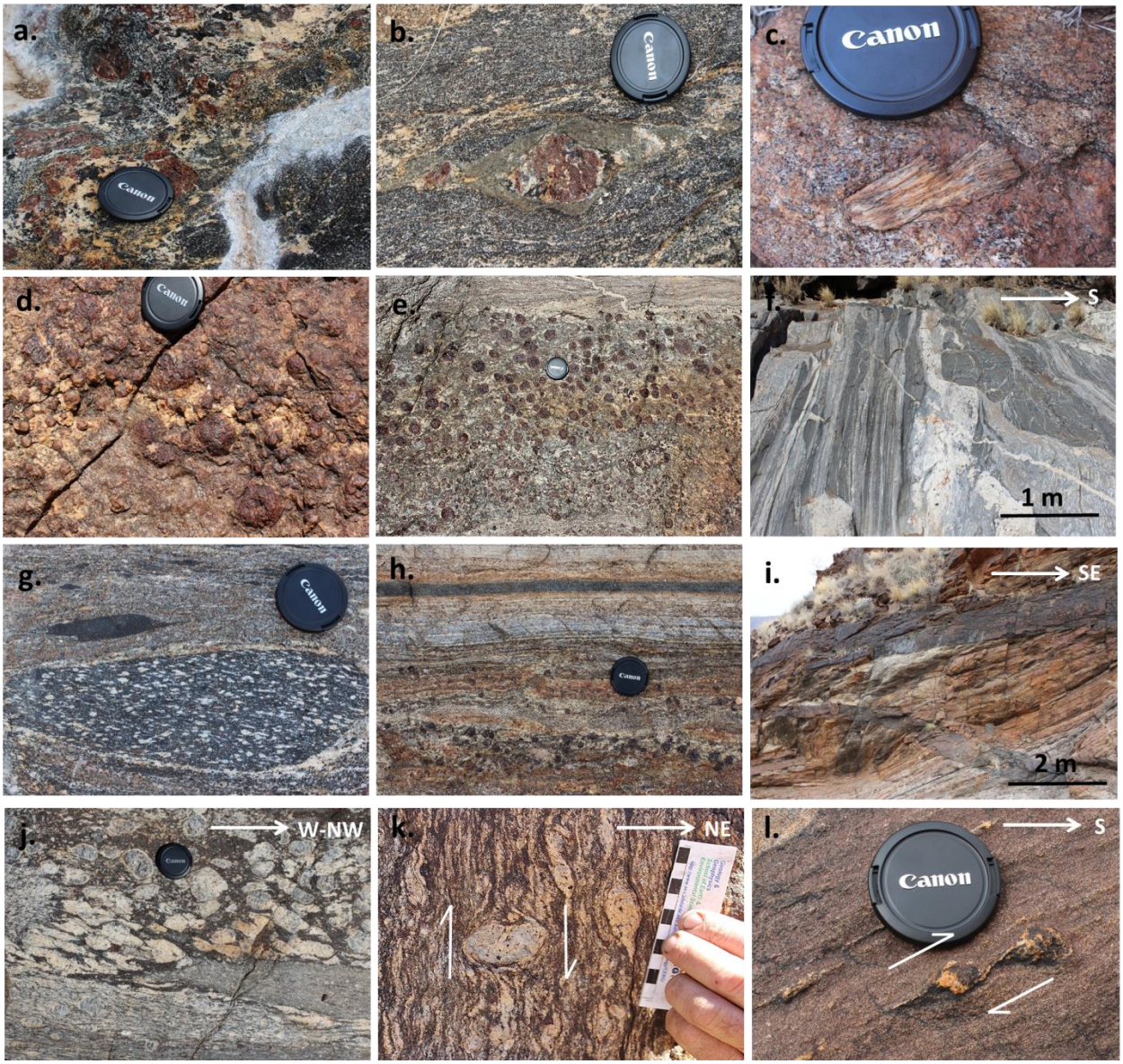

Figure 4. Field photographs from the study area
Lens cap is 6 cm in diameter. (a) & (b) Harts Range Meta-Igneous Complex (HRMC) showing coarse garnet–-clinopyroxene tonalitic segregations which define the peak metamorphic assemblage. Macro-scale reaction textures between garnet and clinopyroxene formed from and retrogressed to coarse hornblende–plagioclase assemblages are clearly visible in (b). (c) Sillimanite pseudomorphs after andalusite within garnet–biotite–sillimanite gneiss (Irindina Gneiss metapelite). (d) Coarse garnet (up to 8 cm diameter) tonalitic segregations in the garnet–biotite–sillimanite migmatitic Irindina Gneiss defining the peak mineral assemblage. (e) Coarse-grained garnet (comprising up to 80% rock) adjacent lithological contact with metapelite diatexite. (f) Mafic diatexite creek exposure. (g) Two generations of amphibolite: fine-grained eqiproportional hornblende–plagioclase amphibolite (smaller lens) and plagioclase-phyric amphibolite with a hornblende-rich matrix (larger lens), present as boudins within diatexite. (h) Amphibolite sill within the quartzofeldspathic Irindina Gneiss. (i) Discordant amphibolite dykes cross-cut quartzofeldspathic gneiss in the southern field area. (j) Mega-crystic augen gneiss at Watson's Creek approximately 3 km NW along strike of the felsic diatexite domain within the central field area. The photo incorporates a largely 'un-strained' zone grading into the felsic diatexite domain (bottom of image) where the augen are partially to completely recrystallised. (k) NE-side-down normal shear-sense (D2) indicators within the felsic diatexite. (l) Top-to-the-SW (regional D3) delta-porphyroclast kinematic indicator located within the Irindina Gneiss near the Brady Gneiss boundary just north of the field area. Shear sense of kinematic indicators is shown.

Table 1. Summary and description of lithological units in the study area

Lithological unit^	Description		Additional characteristics- outcrop style, occurrence, lithological relationships
	Mineralogy	**Textural & structural features**	
Alice Springs Orogeny (450-300 Ma)			
Tremolite alteration zone	Amphibole-gedrite and undifferentiated calc-silicate		Discontinuous outcrops within close proximity to pegmatite, leucogneiss and amphibolite. Sharp lithological contacts.
Pegmatite	Very coarse ksp–plag–qtz–bi–mus (up to 6 cm)	Occur in two orientations – NW–SE and NE–SW trending. Variable intensity of bi–mus foliation and qtz–plag mineral stretching lineation.	Cross cut all other units below. Occur in all units but more prevalent within diatexite and metapelitic Irindina gneiss.
Coarse-grained leucogneiss	Coarse plag–qtz ± ksp ± bi		
Harts Range Group			
Metapelitic Irindina Gneiss			
Quartzo-feldspathic gt–bi migmatitic gneiss	Gt–plag–bi–qtz ± sill quartzofeldspathic migmatitic gneiss. Sillimanite (< 5%) is fine-grained and defines a foliation with biotite when present, and is interspersed throughout the rock. Garnet (grains generally < 2 cm) constitutes > 10% rock.	Moderately-coarse fabric defined by bi ± sill and a mineral stretching lineation defined by plag–qtz ± sill.	Gradation to mus-bi-gt schist (over < 5 m) at contacts with metapelite diatexite. Diffuse contact with garnetiferous gneiss. Contact with mafic granulite and amphibolite is relatively sharp (< 1 m).
Garnetiferous gt–bi–sill migmatitic gneiss***** **(Peak metapelitic assemblage)**	Very-coarse gt (up to 8 cm)–bi–plag–qtz–sill. Sillimanite is interspersed throughout the rock (< 5%) and also in pseudomorphs interpreted to be after andalusite (grains 1–4 cm). The psudomorphed grains are themselves randomly oriented relative to the foliation, but the sillimanite needles parallel the long axis of the psudomorph. Garnet comprises > 20% rock.	Coarse, weak migmatitic fabric defined by bi–sill grossly parallel to the lithological layering. Lineation defined by qtz–plag is weak to absent. Gt ± bi grow in coarse tonalitic leucosomes which largely align with the fabric.	Significant increase in garnet (grains < 8 cm, comprising up to 80% rock) at contact with metapelite diatexite; gradational transition over < 8 m interval. Relatively sharp contact with amphibolite.
Stromatic diatexite	Classified on the basis of majority metapelitic, 'mafic' or 'felsic' (basement) component. Comprised of: (1) Plag–ksp–qtz ± bi leucosome segregations and pegmatite; (2) Mafic (amphibolite) component (> 15%): two endmembers - equigranular hbl–plag, and plagioclase-phyric amphibolite (3) > 30% component of metapelite, metabasite or felsic (basement) megacrystic gneiss	Leucosomes, pegmatite and amphibolite occur as intermingled roughly layer-parallel segregations. Amphibolite also occurs as isolated lenses and boudins (cm- to m-scale). Pegmatite and mafic dykes are in part deformed. Coarse, granoblastic fabric and weakly preserved lineation. Locally preserved apparent dextral shear-sense on horizontal surfaces (although lineation too weak to justify). NE-side down kinematics parallel to weak lineation in vertical section.	Gradational contact (over 1–10 m) with all surrounding lithologies. Component of metapelite, mafic or basement component is largely consistent with the surrounding lithologies.
Harts Range Meta-Igneous Complex, HRMC (Mt. Riddock Member)			
Coarse-grained hbl–plag amphibolite	Two generations: (1) Moderately-coarse, equigranular granoblastic hbl–plag rock. (2) Coarse plagioclase phenocrysts (up to 8 mm) in an equigranular hbl–-plag groundmass (< 4 mm).	Elongate hbl ± plag define a moderately-coarse foliation. Plagioclase elongate in the foliation direction defines a moderately-strong lineation.	Occur as laterally extensive units which are in part deformed and intermingle layer-parallel with metapelite and diatexite, and also occur as isolate lenses and boudins within both units. Slightly gradational (< 1 m) contact with metapelite. Finer-grained amphibolite also occurs as discordant dykes which cross-cut basement units in the SW mapping area, with distinct contacts. Relative timing relationships between endmembers is unclear. Endmembers not differentiated at the mapped scale.

Lithological unit^	Description		Additional characteristics- outcrop style, occurrence, lithological relationships
	Mineralogy	**Textural & structural features**	
Coarse-grained gt–cpx–hbl–plag (mafic) granulite* **(Peak metabasite assemblage)**	Very coarse gt (up to 15 cm)–cpx–hbl–plag-bearing tonalitic migmatitc segregations located witin coarse-grained equigranular hbl–plag amphibolite.	Weak, coarse migmatitc foliation grossly parallel to lithological layering defined by hbl–plag ± gt ± cpx. Lineation defined by hbl–plag is weak to absent. Local preservation of reaction textures showing gt–cpx growing from coarse hbl–plag assemblages. Pervasive retrogression by gt-cpx breakdown to hbl–plag.	Located in the central mapping area. Gradiational contact with very coarse-grained amphibolite; less gradational contacts with coarse-grained amphibolite. Gradational contact (over 1–10 m) with mafic diatexite. Moderately distinct contact (generally < 2 m) with metapelite.
Very-coarse hbl–plag amphibolite	Equiganular, coarse (grains ~0.5–2 cm) hbl–plag ± cpx.	Coarse, granoblastic and equigranular texture. Very-coarse, weak foliation and weak to absent lineation defined by hbl.	Restricted to the central mapping area. Gradational contacts with mafic granulite (over 1–2 m) and retrogressed hornblendite. Occurs topographically higher than, and has a distinct boundary with the surrounding metapelite.
Retrogressed hornblendite	Moderately-coarse sub-aligned hbl grains (~4 mm), dark-green bladed amphibole, and micaceous brown-weathered chl (< 2 mm) (?) replacing formerly cpx laths (?).	Coarse foliation defined by elongate hbl ± chl.	Localised outcrops located to the E–NE mapping area. Largely gradational contact with amphibolite; sharp contact with metapelite.
Palaeoproterozoic basement			
Megacrystic gneissic granitoid	Very coarse-grained (1–8 cm) blue-grey K-feldspar augen mantled by a rim of fine white plag ± qtz with rapakivi texture, within a ksp–plag–qtz–hbl–bi ± gt groundmass.	Bi±hbl foliation which wraps about ksp augen forms a discontinuous, sub-parallel gneissic layering with interlayered quartzo-feldspathic material. Locally finer-grained (phaneritic) texture observed with flattened, smaller, asymmetric augens. Higher-strain (felsic diatexite) domains are characterised by partially-completely recrystallised phenocrysts.	Contains plagioclase-phyric and fine-grained equigranular mafic dykes and lenses (cm-to meter-scale). Contact with felsic diatexite is diffuse over 2–10m.
Strangways Metamorphic Complex			
Retrogressed opx-bearing amphibolite	Porphyritic plagioclase (up to 8 mm) and red-orange (retrogressed) opx (~0.5 mm) mantled by a rim of black fine-grained hbl, in a hbl-rich hbl ± cpx ± plag groundmass. Locally regions of equigranular hbl–plag ± opx amphibolite.	Foliation defined by elongate hornblende and porphyritic plagioclase elongate parallel to the fabric and also defining a strong mineral stretching lineation.	Localised to the SW corner of map. Gradational contact (over 20 m interval) with amphibolite to the NE and sub-mylonitised gneiss to the SW. Increasing proportion of (mylonitised) metapelite component towards the SW.
Proto-mylonitised migmatitic gneiss (15 – 60% mafic dyke component)	Gt–plag–bi–qtz ± sill migmatitic gneiss with locally more gt-bi-rich segregations. Garnet (grains generally 0.5–3 cm) constitutes ~10–15% rock.	Moderately-coarse fabric defined by bi ± sill and a strong mineral stretching lineation defined by plag–qtz. Rock appears highly reworked, with locally top-to-SW kinematics.	Discordant amphibolite dykes cross-cut metapelite with gernerally distinct lithological contacts. Dykes are variable in size (up to ~10 m length and up to 2 m width). Mafic component decreases gradationally towards the SW.
Proto-mylonitised migmatitic gneiss (< 15% mafic dyke component)	Description as above. Unit localised to the far SW mapping area. Mafic dyke component is <15%.		

^Lithologies are ordered on the basis of relative age established from cross-cutting relationships and tectonic and metamorphic fabrics.
Lithologies defining the peak metabasite (HRMC) and Irindina Gneiss metapelite mineral assemblages are also denoted with an asterisk.
Mineral abbreviations: bi, biotite; chl, chlorite; cpx, clinopyroxene; gt, garnet; hbl, hornblende; Ksp, K-feldspar; mus, muscovite; opx, orthopyroxene; plag, plagioclase feldspar; qtz, quartz; sill, sillimanite.

3. ANALYTICAL METHODS

3.1. Geochronology

3.1.1. SHRIMP ZIRCON U–PB GEOCHRONOLOGY

Detrital zircon samples from the Stanovos Gneiss, Irindina Gneiss and Brady Gneiss (Maidment *et al.* 2013), and Pacoota Sandstone, Arumbera Sandstone and Heavitree Quartzite from the Amadeus Basin, and Tomahawk Formation from the Georgina Basin (Maidment *et al.* 2007) have been used for Hf-isotopic analysis is this study to evaluate the proposed correlations suggested by Maidment *et al.* (2013). U–Pb analysis for these samples was carried out previously at the Australian National University, Canberra, with full procedures detailed in Maidment *et al.* (2007) and Maidment *et al.* (2013). However, one sample could not be matched to the original cathodoluminescence imagery (CL), and therefore U–Pb analysis has been repeated for this sample.

Zircon grains were imaged using a Phillips XL40 Scanning Elelctron Microscope (SEM) fitted with a Gatan CL detector at Adelaide Microscopy, University of Adelaide. Zircon U–Pb data were collected using a Sensitive High Resolution Ion Microprobe Mass Spectrometer (SHRIMP II) located in the John de Laeter Centre of Mass Spectrometry at Curtin University of Technology, Perth, Western Australia.

SHRIMP analytical procedures follow those documented by De Laeter and Kennedy (1998). Zircons were ablated using a primary bean current of typically 2.2 nA, a spot size of approximately 25 μm and a mass resolution of about 5000. A secondary beam with a ^{206}Pb sensitivity of 22–24 cps/ppm/nA was achieved. Each analysis involved a two-minute raster followed by five measurement cycles (with dwell times) of Zr_2O (2 s), ^{204}Pb (8 s), background (8 s), ^{206}Pb (15 s), ^{207}Pb (25 s), ^{208}Pb (8 s), ^{238}U (4 s), ^{248}ThO (3 s) and ^{254}UO (2

s). Common Pb correction was made on the basis of measured ^{204}Pb counts (Compston *et al.* 1984). SL13 was used as the primary reference standard (Claoué-Long *et al.* 1995) and Temora 2 was used as the secondary standard and U concentration reference (Black *et al.* 2004). The uncertainty for unknown analyses was <1% however the external spot to spot uncertainty for the Temora 2 standard was 2.2%. SQUID v.2.50 and Isoplot v.4.15 were used for data reduction (Ludwig 2009, 2012).

3.1.2. LA-ICP-MS MONAZITE U–PB GEOCHRONOLOGY

In situ U–Pb monazite Laser Ablation Multicollector Inductively Coupled Mass Spectrometry (LA-MC-ICP-MS) geochronology was undertaken on samples from the Lower Brady Gneiss immediately north of the field area, at Adelaide Microscopy, University of Adelaide. Analyses were conducted on a New Wave 213 nm laser under a helium ablation atmosphere, attached to an Agilent 7500cx ICP-MS following the methods of Payne *et al.* (2008). A spot size of 15 µm, a frequency of 5 Hz and an average fluence of 11–13 J/cm^2 at the ablation site were used. The total acquisition time of 90 s was inclusive of 40 s background measurement followed by 50 s of sample analysis involving measurement of isotopes ^{204}Pb (10 ms), ^{206}Pb (15 ms), ^{207}Pb (20 ms) and ^{238}U (15ms). Data were corrected for elemental fractionation and mass bias using 'Glitter' software (Griffin *et al.* 2004), using the primary monazite standard MAdel (TIMS normalization data: ^{207}Pb/^{206}Pb age = 491.7 Ma; ^{206}Pb/^{238}U age = 514.8 Ma; ^{207}Pb/^{235}U age = 510.4 Ma; Payne *et al.* (2008)). Accuracy was monitored by repeat analysis of in-house standard 94-222/Bruna NW (c. 450 Ma, Payne *et al.* (2008)). Instrument drift was also corrected for by standard bracketing every 10–12 unknown analyses and the application of a linear correction. Weighted average ages for 94-222/Bruna-NW were 472.0 ± 17 Ma (n = 16, MSWD = 1.3) for ^{207}Pb/^{206}Pb, 452.8 ± 4.7 Ma (n = 15, MSWD = 1.5) for ^{206}Pb/^{238}U, and 455.4 ± 5.2 Ma (n = 15, MSWD = 2.3) for ^{207}Pb/^{235}U. Due

to unresolvable interference of ^{204}Hg on ^{204}Pb common lead was not corrected for in age calculations however, analyses were rejected on the basis of appreciable raw ^{204}Pb counts.

3.1.3. COMPARATIVE AGE MODELLING

Maidment *et al.* (2013) proposes that the HRG correlates with units in the Amadeus and Georgina basins on the basis of visual comparisons between age spectra. To test this hypothesis, comparisons between detrial zircon age data for samples from the HRG, and Amadeus and Georgina basins (Fig. 1) are objectively quantified by employing multidimensional scaling (MDS), a standard statistical technique, following the methods of Vermeesch (2013). Age data are sourced from Maidment *et al.* (2013), Maidment *et al.* (2007), Hollis *et al.* (2010), Buick *et al.* (2001), Buick *et al.* (2005) and Zhao *et al.* (1992) and only include <10% discordant analyses. Methods are documented in Appendix I.

3.2. Lu–Hf isotope analysis

Lu–Hf isotopic analyses on detrital zircons from the HRG, Amadeus and Georgina basins by LA-MC-ICP-MS were undertaken at the joint CSIRO-University of Adelaide facility, South Australia. Analyses were conducted on all seven detrital zircon samples analysed for U–Pb SHRIMP ages in previous studies (Maidment *et al.* 2007; Maidment *et al.* 2013), and this study. Grains were selected on the basis of good internal structure, >90% concordance and low ^{204}Pb content. Analysis spots were placed as close as possible to the concordant SHRIMP spot localities. Analytical methods for zircon Hf isotopic determination are detailed in Payne *et al.* (2013).

Analyses were conducted using a New Wave UP-193 Excimer laser (193 nm) attached to a Thermo-Scientific Neptune Multi Collector ICP-MS equipped with Faraday detectors and $10^{11}\Omega$ amplifiers. The analyses were carried out under a helium atmosphere

mixed upstream of the ablation cell with argon and nitrogen, using a beam diameter of 50 μm, a 5 Hz repetition rate, and an intensity of approximately 6 J/cm^2. Typical ablation times were 60–225 s involving a maximum of 15 measurement cycles, each consisting of ten 0.524 s integrations on ^{171}Yb, ^{173}Yb, ^{175}Lu, ^{176}Hf (+ Lu + Yb), ^{177}Hf, ^{178}Hf, ^{179}Hf and ^{180}Hf; one 0.524 s integration of REE ^{160}Gd, ^{163}Dy, ^{164}Dy, ^{165}Ho, ^{166}Er, ^{167}Er, ^{168}Er, ^{170}Yb and ^{171}Yb, and one 0.524 s integration of Hf oxides with masses ranging from 187 to 196 amu. This is inclusive of a 1.5 s idle time between subsequent mass changes and an off-peak baseline measurement. Oxide formation rates and REE-oxide interference in high REE zircon were monitored throughout the session. Hf oxide formation rates for all analytical sessions in this study were within the range 0.03–0.06%.

Data were normalised by an exponential mass bias correction using a stable ^{179}Hf/^{177}Hf ratio of 0.7325. Isobaric interferences on ^{176}Hf by Yb and Lu were corrected using the methods of Woodhead *et al.* (2004) with direct measurement of ^{171}Yb/^{173}Yb fractionation using the Yb isotopic values of Segal *et al.* (2003). Assuming the same mass bias behaviour as Yb, a correction for Lu isobaric interference on ^{176}Hf used a ^{176}Lu/^{175}Lu ratio of 0.02655 (Vervoort *et al.* 2004). Data were processed using software *HfTRAX* v.3.2 (Payne *et al.* 2013).

Instrument performance and stability was monitored by analysis of Plesovice and Mudtank zircon standards and a JMC475 Hf glass standard (Payne *et al.* 2013). The average ^{176}Hf/^{177}Hf value for Plesovice for the analytical session was 0.282472 ± 0.000016 (2σ, n = 10) which is within uncertainty of the published value of 0.282482 ± 0.000013 (2σ, Slama *et al.* (2008)). The mean ^{176}Hf/^{177}Hf value for Mudtank analyses was 0.282510 ± 0.000015 (2σ, n = 7) which is likewise within uncertainty of 0.282507 ± 0.000044 (2σ, Woodhead and Hergt (2005)). Depleted-mantle crustal model ages ($T_{\mathrm{DM\ crustal}}$), and epsilon hafnium values ($\varepsilon_{\mathrm{Hf}}$) were calculated following the methods of Griffin *et al.* (2002). An average crustal

composition of $^{176}Lu/^{177}Hf = 0.015$, chondritic uniform reservoir (CHUR) values of Bouvier *et al.* (2008) and a ^{176}Lu decay constant of 1.865×10^{-11} yr^{-1} (Scherer *et al.* 2001) were used.

3.3. Bulk-rock and mineral chemistry

Whole-rock geochemical analyses for phase equilibria modelling were undertaken by Wavelength Dispersive X-ray Fluorescence (WD-XRF) spectrometry at the Earth and Environmental Department, Franklin and Marshall College, Lancaster PA (Appendix J).

Mineral compositions and elemental x-ray maps were obtained using a CAMECA SXFive electron microprobe at Adelaide Microscopy, University of Adelaide. A beam current of 20 nA, accelerating voltage of 15 kV and a defocussed beam size of 5 µm was used for all point analyses, and a PAP correction was applied to all data. Routine analyses were made for SiO_2, TiO_2, Cr_2O_3, Al_2O_3, FeO, MnO, MgO, CaO, Na_2O, K_2O, ZnO and P_2O_5 on Wavelength Dispersive Spectrometers (WDS). Calibration was done on natural and synthetic mineral standards supplied by Astimex, Taylor and P&H. Compositional mapping of garnet grains used a 15 kV accelerating voltage, a beam current of 150 nA, a dwell time of 50 ms and a step size of 20µm. Analyses of Fe, Mg, Mn, Ca and Al were collected on WDS and analyses of Si, Ti, K, Na, P, Zn, Zr and Ce on Electron Dispersive Spectrometers.

3.4. Mineral equilibria modelling

3.4.1. THERMOBAROMETRY

Pressure–temperature (P–T) calculations were made following the average P–T approaches of Powell and Holland (1994). Calculations were done using the software THERMOCALC v.3.21 (Powell and Holland 1988; Powell *et al.* 1998) with an updated and expanded version of the internally consistent thermodynamic dataset (Sept 1999 update) of Holland and Powell (1998). Mineral endmember activities were recalculated from electron

microprobe analyses (Appendix D) using software AX 2 (2008 update). Methods and model parameters are documented in Appendix H. Water activites (a_{H2O}) used for mafic granulite and metapelite samples were 0.4 and 0.8, respectively. The presence of leucosomes suggests fluid-absent partial melting prevailed, typically associated with low a_{H2O}, however higher values were selected due to occurrence of relatively hydrous hornblende- and mica-rich mineral assemblages, respectively (Phillips 1980; Lamb and Valley 1988; Mawby *et al.* 1999; Scrimgeour and Raith 2001). The chosen a_{H2O} value for metapelite also gave the most realistic temperature estimate (>650ºC) as suggested by the presence of leucosomes.

3.4.2. PRESSURE–TEMPERATURE PSEUDOSECTIONS

P–T pseudosections were calculated for metapelite samples UBG-4, IG-222, and IG-10 using the phase equilibrium modelling program THERMOCALC v.3.33 (update Nov. 2009, Powell and Holland (1988)) with the internally consistent thermodynamic dataset of Holland and Powell (1998). Pseudosections were calculated for the geologically realistic system of MnNCKFMASHTO ($MnO–Na_2O–CaO–K_2O–FeO–MgO–Al_2O_3–SiO_2–H2O–TiO_2–Fe_2O_3$). The following activity relationships were used: silicate melt (White *et al.* 2007); cordierite and staurolite (Mahar *et al.* 1997; Holland and Powell 1998b); garnet, biotite, ilmenite and hematite (White *et al.* 2005); orthopyroxene, spinel and magnetite (White *et al.* 2002); chloritoid (Mahar *et al.* 1997; White *et al.* 2000); muscovite and paragonite (Coggon and Holland 2002); plagioclase and K-feldspar (Holland and Powell 2003). Whole-rock XRF analyses recalculated to molar oxide percent were used for the bulk composition of each sample (Appendix C). The H_2O content used for each buk-rock compositions was set so that mineral assemblages were just H_2O-saturated at the solidus for above-solidus calcluations and over-saturated for below solidus. The proportion of Fe_2O_3 (as Fe_2O_{3T} from whole-rock geochemistry) converted to FeO was estimated by extent of sample weathering and the

abundance of Fe^{3+}-bearing minerals (i.e. ilmenite) which overall implied a low oxidation state. The amount of remaining Fe_2O_3 is recast as 'O' in MnNCKFMASHTO calculations. Modal proportions and compositional isopleths were calculated to further constrain the P–T path.

4. RESULTS

4.1. Provenance of the HRG

4.1.1. SHRIMP ZIRCON U-PB GEOCHRONOLOGY

U-Pb SHRIMP analysis was done on 62 grains from the Arumbera Sandstone (Fig. 5, Table 2). The detrital zircon signature is dominated by ages between ~1200 and 1050 Ma, consistent with previous analysis undertaken by Maidment *et al.* (2007) on the same sample. The youngest detrital zircon is 605 ± 14 Ma which is significantly younger than the other analysed grains, but is broadly similar to the inferred depositional age of ~540 Ma (Maidment *et al.* 2007).

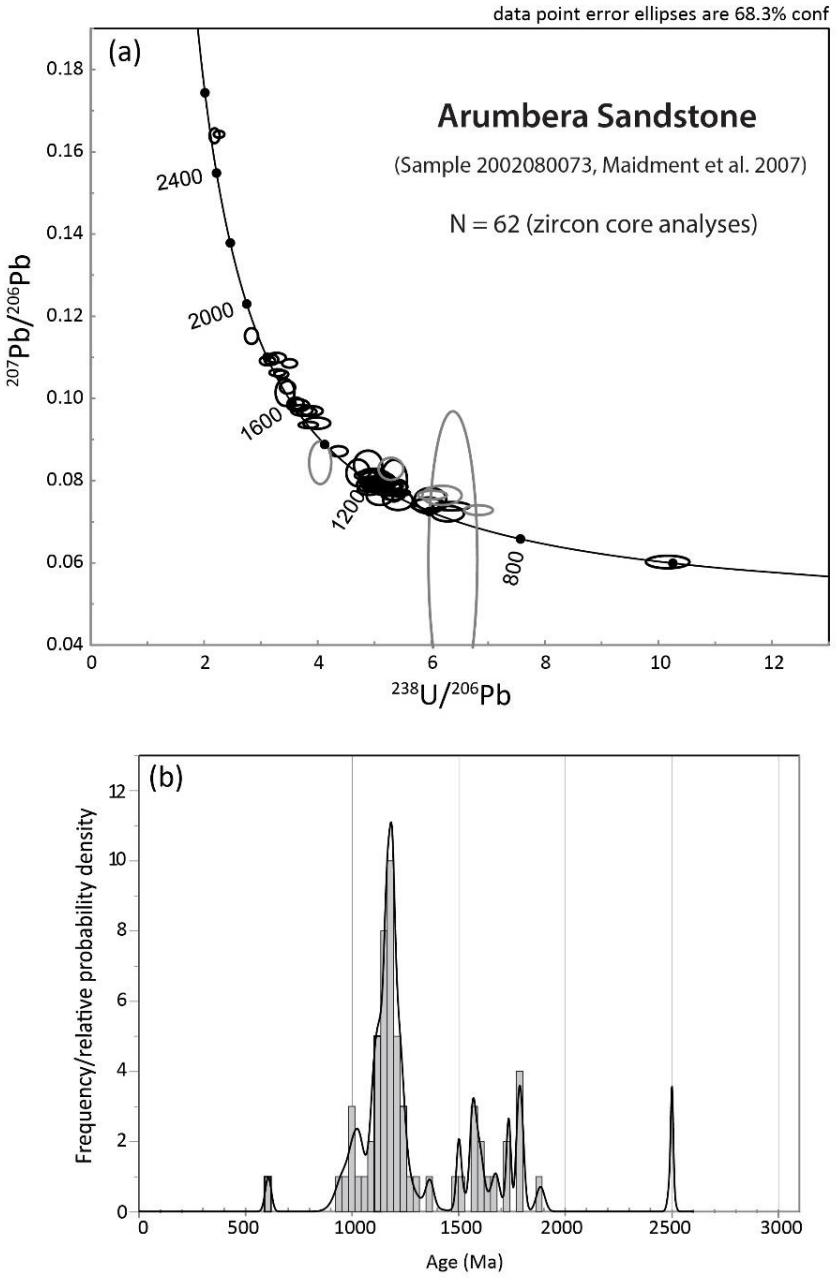

Figure 5. SHRIMP zircon U–Pb geochronology for the Arumbera Sandstone. (a) Tera-Wasserburg concordia plot and (b) probability density plot for Arumbera Sandstone (Sample 2002080073 from Maidment *et al*. 2007). Analyses which are > 10% discordant are coloured grey for clarity. These ages are not represented in the probability density plot.

Table 2. SHRIMP zircon U–Pb geochronology results

Spot	U (ppm)	Th (ppm)	Th/U	$^{204}Pb/^{206}Pb$	1σ	$^{207}Pb/^{206}Pb$	1σ	$^{206}Pb/^{238}U$	1σ	$^{206}Pb_c$ %	$^{206}Pb^*$ (ppm)	$^{238}U/^{206}Pb^*$	1σ	$^{207}Pb^*/^{206}Pb^*$	1σ	$^{207}Pb^*/^{235}U$	1σ	$^{206}Pb^*/^{238}U$	1σ	ρ	% Disc.	Apparent ages (Ma)				Inferred age (Ma)	1σ
																						$^{206}Pb/^{238}U$	1σ	$^{207}Pb/^{206}Pb$	1σ		
AS-1	131	143	1.13	-0.00005	-0.00003	0.07814	0.00086	0.457	0.005	-0.08926	22	5.09	0.13	0.0788	0.0010	2.14	0.06	0.197	0.005	0.90	+1	1157	28	1168	25	1168	25
AS-2	91	69	0.79	-0.00008	-0.00006	0.07889	0.00113	0.442	0.004	-0.15053	16	4.99	0.17	0.0801	0.0014	2.21	0.09	0.200	0.007	0.89	+2	1177	37	1199	34	1199	34
AS-3	143	126	0.91	0.00000	0.00000	0.09396	0.00091	0.581	0.006	0.00000	31	3.98	0.16	0.0940	0.0009	3.25	0.13	0.251	0.010	0.97	+5	1444	51	1507	18	1507	18
AS-4	634	232	0.38	0.00002	0.00001	0.07892	0.00043	0.452	0.005	0.04492	103	5.26	0.16	0.0786	0.0005	2.06	0.06	0.190	0.006	0.98	+4	1123	31	1161	12	1161	12
AS-5	220	493	2.32	0.00003	0.00003	0.06069	0.00088	0.242	0.001	0.06172	19	10.16	0.25	0.0602	0.0010	0.82	0.02	0.098	0.002	0.83	+1	605	14	611	36	605	14
AS-6	147	102	0.71	0.00006	0.00003	0.09910	0.00086	0.652	0.012	0.10259	34	3.65	0.13	0.0983	0.0010	3.71	0.14	0.274	0.010	0.96	+2	1559	49	1592	18	1592	18
AS-7	41	40	1.00	0.00000	0.00000	0.07551	0.00177	0.428	0.005	0.00000	6	5.99	0.18	0.0755	0.0018	1.74	0.07	0.167	0.005	0.79	+9	996	28	1082	47	996	28
AS-8	210	142	0.70	0.00003	0.00002	0.08011	0.00071	0.447	0.007	0.05933	35	5.11	0.15	0.0796	0.0008	2.15	0.07	0.196	0.006	0.95	+3	1153	30	1188	19	1188	19
AS-9	394	73	0.19	-0.00001	-0.00001	0.07691	0.00053	0.417	0.004	-0.01721	63	5.38	0.16	0.0770	0.0005	1.97	0.06	0.186	0.006	0.97	+2	1099	30	1122	14	1122	14
AS-10	167	105	0.65	-0.00004	-0.00003	0.08091	0.00082	0.457	0.008	-0.07527	29	4.98	0.16	0.0815	0.0009	2.26	0.08	0.201	0.006	0.94	+5	1180	34	1233	22	1233	22
AS-11	107	121	1.16	0.00017	0.00008	0.07867	0.00100	0.428	0.003	0.30307	18	5.09	0.15	0.0763	0.0015	2.07	0.07	0.196	0.006	0.84	-5	1156	32	1103	39	1156	32
AS-12	124	76	0.64	-0.00005	-0.00004	0.08009	0.00090	0.452	0.003	-0.09426	21	5.09	0.13	0.0808	0.0010	2.19	0.06	0.197	0.005	0.89	+5	1157	27	1217	25	1217	25
AS-13	263	281	1.10	-0.00003	-0.00002	0.07855	0.00063	0.452	0.008	-0.04773	44	5.10	0.13	0.0789	0.0007	2.13	0.06	0.196	0.005	0.94	+1	1155	26	1170	17	1170	17
AS-14	118	151	1.32	0.00000	0.00000	0.07852	0.00095	0.435	0.003	0.00000	19	5.25	0.14	0.0785	0.0010	2.06	0.06	0.191	0.005	0.90	+3	1124	27	1160	24	1160	24
AS-15	249	225	0.93	0.00002	0.00002	0.09707	0.00064	0.610	0.003	0.03860	56	3.80	0.12	0.0968	0.0007	3.51	0.11	0.263	0.008	0.97	+4	1505	41	1563	13	1563	13
AS-16	167	183	1.13	0.00013	0.00005	0.08019	0.00083	0.411	0.007	0.24157	27	5.28	0.20	0.0783	0.0011	2.05	0.08	0.189	0.007	0.93	+3	1118	38	1154	29	1154	29
AS-17	116	174	1.55	0.00000	0.00000	0.07966	0.00097	0.450	0.007	0.00000	19	5.13	0.19	0.0797	0.0010	2.14	0.08	0.195	0.007	0.95	+4	1149	38	1189	24	1189	24
AS-18	174	155	0.92	0.00003	0.00002	0.11023	0.00076	0.707	0.004	0.04763	46	3.27	0.11	0.1099	0.0008	4.63	0.16	0.306	0.010	0.98	+5	1719	51	1797	13	1797	13
AS-19	322	165	0.53	-0.00004	-0.00002	0.08061	0.00058	0.450	0.002	-0.07912	57	4.85	0.13	0.0812	0.0007	2.31	0.06	0.206	0.006	0.96	+2	1209	30	1227	16	1227	16
AS-20	40	10	0.26	0.00364	0.00069	0.11349	0.01992	0.390	0.016	6.57905	5	6.38	0.28	0.0607	0.0239	1.31	0.52	0.157	0.007	0.11	-53	939	39	627	849	939	39
AS-21	316	139	0.45	0.00001	0.00001	0.07966	0.00061	0.466	0.005	0.02159	54	5.03	0.14	0.0795	0.0006	2.18	0.07	0.199	0.006	0.96	+1	1170	31	1184	16	1184	16
AS-22	435	315	0.75	0.00003	0.00002	0.07893	0.00049	0.468	0.004	0.05816	74	5.03	0.16	0.0785	0.0005	2.15	0.07	0.199	0.006	0.98	-1	1168	35	1159	14	1159	14
AS-23	392	83	0.22	-0.00003	-0.00001	0.10581	0.00052	0.653	0.004	-0.05835	102	3.29	0.09	0.1063	0.0006	4.46	0.12	0.304	0.008	0.98	+2	1713	41	1736	10	1736	10
AS-24	220	172	0.81	-0.00005	-0.00003	0.07698	0.00071	0.421	0.004	-0.09272	36	5.17	0.13	0.0777	0.0008	2.07	0.06	0.193	0.005	0.92	-0	1140	26	1139	21	1139	21
AS-25	95	111	1.20	0.00004	0.00004	0.07963	0.00109	0.426	0.003	0.07034	17	4.89	0.13	0.0791	0.0012	2.23	0.07	0.204	0.006	0.87	-2	1199	30	1174	31	1199	30
AS-26	353	218	0.64	0.00000	0.00000	0.07618	0.00055	0.409	0.002	0.00000	57	5.33	0.13	0.0762	0.0005	1.97	0.05	0.188	0.005	0.96	-1	1109	25	1100	14	1100	14
AS-27	203	124	0.63	0.00005	0.00003	0.07849	0.00071	0.449	0.003	0.09136	35	4.91	0.13	0.0778	0.0008	2.19	0.06	0.204	0.006	0.93	-5	1196	30	1141	21	1141	21
AS-28	175	138	0.81	0.00006	0.00003	0.09794	0.00076	0.631	0.003	0.10861	40	3.72	0.13	0.0971	0.0009	3.60	0.13	0.269	0.009	0.97	+2	1536	46	1569	17	1569	17
AS-29	277	68	0.25	0.00000	0.00000	0.07376	0.00067	0.399	0.007	0.00000	37	6.35	0.22	0.0738	0.0007	1.60	0.06	0.157	0.005	0.97	+10	943	30	1035	18	1035	18
AS-30	116	62	0.55	0.00007	0.00005	0.07297	0.00101	0.379	0.003	0.12766	16	6.29	0.19	0.0720	0.0012	1.58	0.05	0.159	0.005	0.87	+4	951	26	985	35	951	26

Table 2. (cont.) SHRIMP zircon U–Pb geochronology results

Spot	U (ppm)	Th (ppm)	Th/U	$^{204}Pb/^{206}Pb$	1σ	$^{207}Pb/^{206}Pb$	1σ	$^{206}Pb/^{238}U$	1σ	$^{206}Pb_c$ %	$^{206}Pb^*$ (ppm)	$^{238}U/^{206}Pb^*$	1σ	$^{207}Pb^*/^{206}Pb^*$	1σ	$^{207}Pb^*/^{235}U$	1σ	$^{206}Pb^*/^{238}U$	1σ	ρ	% Disc.	Apparent ages (Ma) $^{206}Pb/^{238}U$	1σ	$^{207}Pb/^{206}Pb$	1σ	Inferred age (Ma)	1σ
AS-31	368	178	0.50	0.00000	0.00000	0.16431	0.00055	1.010	0.003	0.00773	139	2.26	0.06	0.1643	0.0006	10.01	0.27	0.442	0.012	0.99	+7	2359	54	2500	6	2500	6
AS-32	311	151	0.50	0.00003	0.00002	0.07686	0.00063	0.370	0.002	0.04853	44	6.02	0.17	0.0765	0.0007	1.75	0.05	0.166	0.005	0.95	+11	991	26	1108	18	1108	18
AS-33	155	144	0.96	0.00001	0.00001	0.10961	0.00080	0.694	0.004	0.02624	42	3.18	0.08	0.1094	0.0008	4.74	0.12	0.314	0.008	0.96	+2	1761	39	1790	14	1790	14
AS-34	455	339	0.77	0.00001	0.00001	0.08721	0.00082	0.534	0.004	0.01200	89	4.37	0.11	0.0871	0.0008	2.75	0.07	0.229	0.006	0.93	+3	1330	29	1363	18	1363	18
AS-35	202	261	1.34	0.00001	0.00001	0.09713	0.00075	0.549	0.007	0.02665	44	3.90	0.13	0.0969	0.0008	3.43	0.12	0.257	0.008	0.97	+7	1473	43	1566	15	1566	15
AS-36	195	177	0.94	-0.00002	-0.00002	0.07943	0.00076	0.429	0.006	-0.03411	33	5.08	0.13	0.0797	0.0008	2.16	0.06	0.197	0.005	0.93	+3	1157	26	1190	20	1190	20
AS-37	121	126	1.08	0.00006	0.00004	0.07944	0.00097	0.438	0.003	0.11281	19	5.37	0.14	0.0786	0.0012	2.02	0.06	0.186	0.005	0.87	+6	1101	26	1161	29	1101	26
AS-38	53	63	1.22	0.00019	0.00011	0.08458	0.00146	0.507	0.005	0.34672	10	4.71	0.14	0.0819	0.0021	2.40	0.09	0.212	0.006	0.74	+0	1241	33	1242	51	1241	33
AS-39	41	43	1.10	-0.00014	-0.00010	0.09949	0.00167	0.585	0.008	-0.25722	10	3.42	0.11	0.1015	0.0022	4.09	0.16	0.292	0.009	0.83	-0	1652	47	1651	40	1651	40
AS-40	78	49	0.64	-0.00006	-0.00006	0.07549	0.00129	0.390	0.004	-0.11609	11	6.19	0.23	0.0764	0.0016	1.70	0.07	0.162	0.006	0.88	+14	966	33	1106	41	1106	41
AS-41	135	114	0.88	-0.00006	-0.00004	0.07930	0.00094	0.430	0.003	-0.10447	22	5.16	0.13	0.0801	0.0011	2.14	0.06	0.194	0.005	0.88	+5	1142	27	1200	27	1200	27
AS-42	178	155	0.90	0.00002	0.00002	0.07872	0.00082	0.421	0.006	0.04003	30	5.08	0.18	0.0784	0.0009	2.13	0.08	0.197	0.007	0.95	-0	1159	37	1157	22	1157	22
AS-43	222	89	0.42	-0.00002	-0.00002	0.10883	0.00071	0.675	0.007	-0.04144	61	3.11	0.09	0.1091	0.0007	4.83	0.14	0.321	0.009	0.97	-1	1796	44	1785	12	1785	12
AS-44	76	70	0.95	-0.00015	-0.00009	0.08069	0.00126	0.413	0.004	-0.27852	12	5.29	0.14	0.0829	0.0018	2.16	0.07	0.189	0.005	0.79	+13	1116	28	1266	42	1266	42
AS-45	27	53	2.06	0.00000	0.00000	0.08382	0.00229	0.401	0.006	0.00000	5	4.88	0.16	0.0838	0.0023	2.37	0.10	0.205	0.007	0.78	+7	1201	37	1288	53	1201	37
AS-46	61	57	0.95	0.00029	0.00015	0.08412	0.00261	0.392	0.004	0.52751	10	5.34	0.15	0.0800	0.0033	2.06	0.10	0.187	0.005	0.56	+8	1106	29	1197	83	1106	29
AS-47	823	172	0.22	0.00002	0.00001	0.07991	0.00039	0.419	0.002	0.03529	136	5.18	0.14	0.0796	0.0004	2.12	0.06	0.193	0.005	0.98	+5	1139	28	1188	10	1188	10
AS-48	110	108	1.01	0.00015	0.00006	0.11720	0.00101	0.732	0.006	0.27085	33	2.83	0.08	0.1152	0.0013	5.61	0.16	0.353	0.010	0.93	-4	1950	45	1883	20	1883	20
AS-49	428	262	0.63	0.00002	0.00001	0.07968	0.00055	0.435	0.006	0.03507	74	4.95	0.14	0.0794	0.0006	2.21	0.06	0.202	0.006	0.97	-0	1186	30	1182	14	1182	14
AS-50	303	135	0.46	0.00002	0.00002	0.07308	0.00073	0.303	0.002	0.03527	38	6.83	0.17	0.0728	0.0008	1.47	0.04	0.146	0.004	0.92	+14	881	20	1008	22	1008	22
AS-51	142	68	0.50	0.00002	0.00002	0.09905	0.00089	0.610	0.004	0.03630	34	3.61	0.09	0.0988	0.0009	3.77	0.10	0.277	0.007	0.94	+2	1577	36	1601	18	1601	18
AS-52	153	131	0.89	-0.00003	-0.00003	0.07359	0.00092	0.368	0.002	-0.05507	22	5.96	0.20	0.0740	0.0010	1.71	0.06	0.168	0.006	0.93	+4	1001	32	1042	28	1042	28
AS-53	295	283	0.99	0.00003	0.00002	0.10890	0.00064	0.616	0.007	0.05139	72	3.50	0.09	0.1085	0.0007	4.27	0.11	0.285	0.007	0.97	+10	1619	36	1775	11	1775	11
AS-54	86	30	0.36	0.00002	0.00002	0.16414	0.00116	1.008	0.007	0.03458	34	2.18	0.06	0.1639	0.0012	10.35	0.29	0.458	0.012	0.97	+3	2432	54	2496	12	2496	12
AS-55	38	38	1.03	0.00040	0.00020	0.09003	0.00188	0.484	0.006	0.72863	8	4.04	0.13	0.0843	0.0034	2.88	0.15	0.247	0.008	0.62	-11	1425	41	1301	79	1301	79
AS-56	317	150	0.49	0.00004	0.00002	0.10640	0.00057	0.632	0.002	0.07037	81	3.36	0.08	0.1059	0.0006	4.35	0.11	0.298	0.007	0.97	+3	1681	36	1729	11	1729	11
AS-57	262	164	0.65	-0.00007	-0.00003	0.07298	0.00117	0.362	0.004	-0.12348	38	5.95	0.17	0.0740	0.0013	1.71	0.06	0.168	0.005	0.86	+4	1002	27	1040	35	1002	27
AS-58	387	185	0.49	-0.00001	-0.00001	0.07924	0.00105	0.417	0.004	-0.01904	66	5.00	0.13	0.0794	0.0011	2.19	0.06	0.200	0.005	0.89	+1	1175	28	1182	26	1182	26
AS-59	92	72	0.81	-0.00010	-0.00007	0.07377	0.00118	0.362	0.003	-0.17840	15	5.41	0.17	0.0752	0.0015	1.91	0.07	0.185	0.006	0.84	-2	1093	32	1073	41	1093	32
AS-60	158	139	0.91	-0.00007	-0.00004	0.10166	0.00086	0.607	0.004	-0.13224	39	3.47	0.09	0.1027	0.0010	4.08	0.11	0.288	0.007	0.94	+3	1634	37	1673	18	1673	18
AS-61	480	181	0.39	0.00001	0.00001	0.09372	0.00049	0.553	0.008	0.02340	107	3.83	0.11	0.0935	0.0005	3.36	0.10	0.261	0.008	0.98	+0	1494	39	1499	10	1499	10
AS-62	140	156	1.15	-0.00009	-0.00005	0.07973	0.00095	0.430	0.003	-0.15861	24	4.92	0.13	0.0810	0.0012	2.27	0.07	0.203	0.005	0.87	+3	1193	28	1221	29	1193	28

Erros are 1σ; Pb_c and Pb* indicate the common and radiogenic Pb proportions respectively. 1σ error in standard calibration was 0.76% (not included in the errors shown above but required to compare data from different samples). Common Pb correction was made using measured ^{204}Pb.

4.1.2. COMPARATIVE AGE MODELLING

Dissimilarities between detrital zircon age spectra for units deemed potential correlatives (Fig. 1) from the upper, mid and lower parts of the HRG, and Amadeus and Georgina basins, are quantitatively compared on MDS plots (Fig. 6). Pairwise dissimilarities between samples produce a MDS configuration of points in 'dissimilarity-space' in which similar samples cluster (Stevens *et al.* 2013; Vermeesch 2013). The samples fall into three main groupings that define the upper, mid and lower sequences when compared collectively (Fig. 6a). Samples comprising each cluster are also compared on separate MDS plots (Fig. 6b–d) to reflect the small dissimilarities between these samples. Comparing samples from individual sequences is limited in that there are no constraints on the intrasequence variation that may exist in detrital zircon ages. Conceivably, samples from sequences that are truly depositional correlatives may have different detrital zircon spectra. To account for this, age data are also compared from the entire HRG with the entire Amadeus succession and entire Georgina succession (Fig. 7). The MDS configuration of the overall 'average' provenance of each succession reveals that little dissimilarity exists between these three datasets, particularily between the Amadeus Basin and HRG.

Figure 6. Multidimensional Scaling (MDS) maps of detrital zircon age data for proposed stratigraphic correlative samples from the upper, mid and lower parts of the Harts Range Group (HRG), and Amadeus and Georgina basin successions. (a) Collective MDS plot for all samples deemed stratigraphic correlatives. Pairwise dissimilarities between samples produce a MDS configuration in which samples with a similar age spectra cluster and dissimilar samples occur father apart. The Kolmogorov-Smirnov (K-S) sample effect size is used as a measure of the dissimilarity (refer to Appendix I). Axes of MDS plots are dimensionless as 'K-S' units of distance ($0 < K\text{-}S < 1$) between samples, and orientation is arbitrary. Solid lines connect least dissimilar samples and dashed lines connect the second closest neighbour in 'dissimilarity-space'. Note the close clustering of samples into groups relating to the upper, mid and lower parts of the successions when collectively compared. (b–d) Samples forming the clusters (in (a)) are further compared in individual MDS plots. These plots highlight the small K-S distances between samples (i.e. dissimilarities). A stress value, S, and Shephard Plots (refer to Appendix I), reflect how well original input (K-S) dissimilarities (denoted 'distances') are reproduced by those calculated by the MDS configuration ('dissimilarities') for each sample pair (Satkoski *et al*. 2013, Vermeesch 2013), and therefore assesses the goodness-of-fit of the MDS representation. Minimal scatter in Shephard Plots, reflected by stress approaching zero (on a scale out of 0.2), indicates high reliability of the MDS plots in reflecting actual sample dissimilarities. A QQ-plot is also shown (with (a)), showing quantiles of detrital age spectra of compared samples plotted against one another with two samples following an identical distribution if their data points plot on a 1:1 line. Abbreviations: HRG: UBG – Upper Brady Gneiss, CBS – Crossing Bore Schist, USG – Upper Stanovos Gneiss, LSG – Lower Stanovos Gneiss, NCM – Naringa Calcareous Member; Amadeus Basin: P – Pacoota Sandstone; AS – Arumbera Sandstone, LM – Limbla Member; HTQ – Heavitree Quartzite; Georgina Basin: T – Tomahawk Formation; B – Mt. Baldwin Formation.

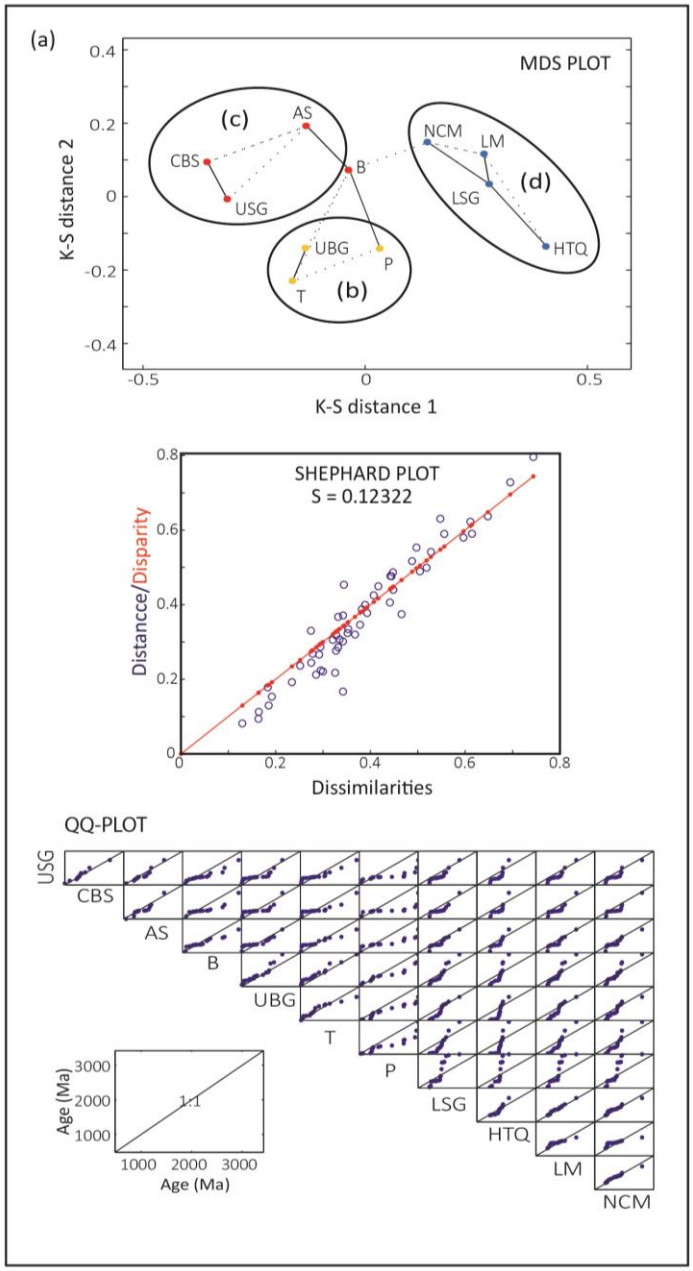
(a)
MDS PLOT
K-S distance 2
K-S distance 1
(c)
(b)
(d)
AS
CBS
USG
B
NCM
LM
LSG
HTQ
UBG
P
T
SHEPHARD PLOT
S = 0.12322
Distancce/Disparity
Dissimilarities
QQ-PLOT
USG
CBS
AS
B
UBG
T
P
LSG
HTQ
LM
NCM
Age (Ma)
1:1

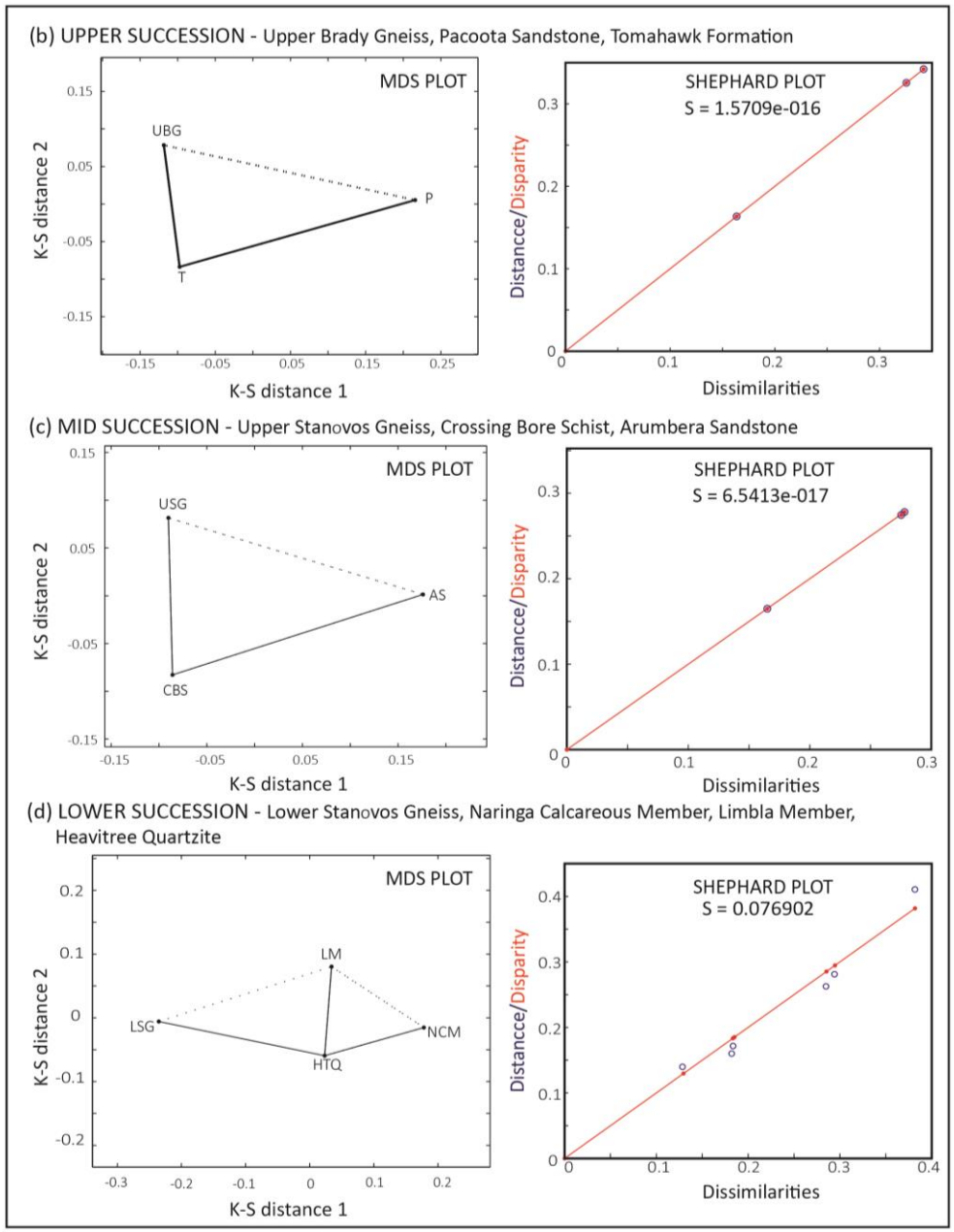
(b) UPPER SUCCESSION - Upper Brady Gneiss, Pacoota Sandstone, Tomahawk Formation
MDS PLOT
UBG
P
T
K-S distance 2
K-S distance 1
SHEPHARD PLOT
S = 1.5709e-016
Distancce/Disparity
Dissimilarities
(c) MID SUCCESSION - Upper Stanovos Gneiss, Crossing Bore Schist, Arumbera Sandstone
MDS PLOT
USG
AS
CBS
K-S distance 2
K-S distance 1
SHEPHARD PLOT
S = 6.5413e-017
Distancce/Disparity
Dissimilarities
(d) LOWER SUCCESSION - Lower Stanovos Gneiss, Naringa Calcareous Member, Limbla Member, Heavitree Quartzite
MDS PLOT
LM
LSG
NCM
HTQ
K-S distance 2
K-S distance 1
SHEPHARD PLOT
S = 0.076902
Distancce/Disparity
Dissimilarities

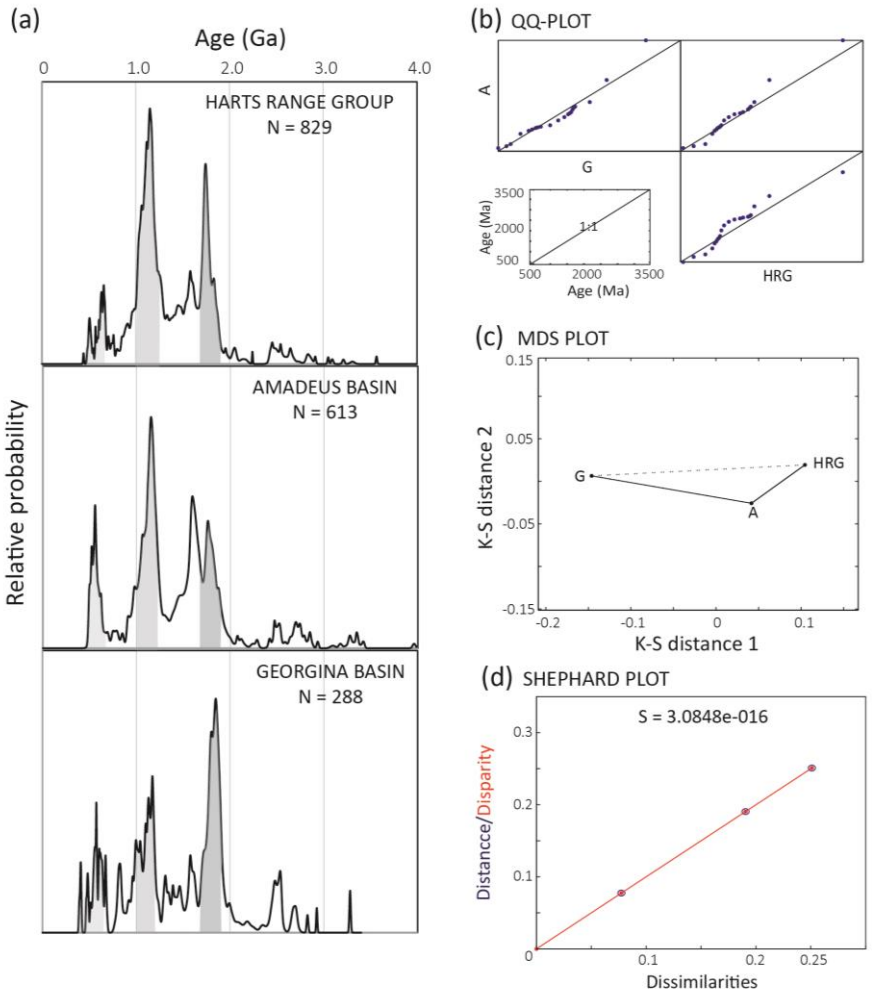

Figure 7. Comparative age modelling between arrays of detrital zircon age data from the entire Harts Range Group (HRG), Amadeus Basin and Georgina Basin successions. (a) Probability Density Plots (PDP) of detrital zircon age data. Dominant zircon population 'events' in the age spectra at c. 1.9–1.7 Ga, 1.2–1.0 Ga and 0.5–0.7 Ga (Maidment *et al.* 2013) are shaded grey. (b) QQ-plot showing quantiles of detrital age spectra of the three datasets plotted against one another with two samples following an identical distribution if their quantiles plot on a 1:1 line. (c) Multidimensional Scaling (MDS) plot for the three datasets in which samples with a similar age spectra cluster (refer to Fig. 6, see also Appendix I). The Kolmogorov-Smirnov (K-S) sample effect size is used as a measure of the dissimilarity between samples (refer to Appendix I). Axes are dimensionless in 'K-S' units ($0 < K\text{-}S < 1$) of distance between samples. Note the overall clustering of all three datasets but particularly between the Amadeus Basin and HRG, relative to the scale of Fig. 6a. (d) Minimal scatter of points in the corresponding Shephard Plot and a stress value, S, approaching zero reflect high reliability of the MDS configuration distances in representing actual sample dissimilarities (refer to Fig. 6, also Appendix I). Abbreviations: HRG – Harts Range Group; A – Amadeus Basin; G – Georgina Basin.

4.1.3. LU–HF ISOTOPIC ANALYSIS

Lu–Hf isotopic analyses have been done on seven samples from the HRG, and Amadeus and Georgina basins. These samples have been selected because of visual similarities in the detrital age signature (Fig. 1, Maidment *et al.* 2013) and they reflect three

separate stratigraphic intervals - upper, mid, and lower, which enables a robust comparison of the entire succession. Zircon Hf-isotope data are provided in Appendix B. Data are presented comparatively in plots of ε_{Hf} versus U–Pb SHRIMP age data (Fig. 8) and by relative probability plots for the ε_{Hf} values of each sample (Fig. 9) grouped according to three inferred dominant zircon population 'events' (see Fig. 7, Maidment *et al.* 2013).

There is an overall broad similarity in zircon Hf isotopic compositions from all three parts of the succession. Analyses from the Upper Brady Gneiss, Pacoota Sandstone and Tomahawk Formation comprise the upper succession with ages between 535–2523 Ma, 540–3345 Ma and 520–3283 Ma. ε_{Hf} values range bewteen -9.83 – +5.52, -34.82 – +13.55, and -22.59 – +13.36, respectively. Samples from the Pacoota Sandstone and Tomahawk Formation contain a younger distribution of ages within the 700–500 Ma subset corresponding to zircon grains which are considerably more isotopically evolved than the other samples in this study. Samples from the Arumbera Sandstone and Crossing Bore Schist from the mid-succession have ages between 605–2500 Ma and 634–2736 Ma, and are dominated by analyses from the c. 1200–1000 Ma population. ε_{Hf} values range between -13.45 – +8.51 and -9.47 – +8.70, respectively, with a dominant ε_{Hf} peak at approximately +2, reflecting a slightly juvenile mantle input relative to CHUR. Analyses from the Heavitree Quartzite and Lower Stanovos Gneiss have an age distribution of 1138–2076 Ma and 1043–2648 Ma with ε_{Hf} values of -6.40 – +8.45 and -14.73 – +9.68, respectively.

Figure 8. Lu–Hf isotope results: ε_{Hf} values plotted against U–Pb ages. A comparison of Lu–Hf detrital zircon isotopic data between proposed stratigraphic correlatives at three separate depth intervals (Maidment *et al.* 2013) for select rocks of the Harts Range Group (HRG), and units in the NE Amadeus and SW Georgina basins. U–Pb age data are from Maidment *et al.* (2007) and Maidment *et al.* (2013). Deviations of Hf ($^{176}Hf/^{177}Hf$) isotopic composition from the chondrite uniform reservoir (CHUR) standard are expressed in epsilon units. Grains which have positive ε_{Hf} values, relative to CHUR, are derived from depleated mantle sources and are termed as more 'juvenile'. Grains which have negative ε_{Hf}, relative to CHUR, are derived from either relatively enriched mantle and/or a an enriched crustal source, and are denoted as being more isotopically 'evolved'. ε_{Hf} versus U–Pb ages for individual zircon grains from: (a) Pacoota Sandstone (Amadeus), Tomahawk Formation (Georgina) and Upper Brady Gneiss (HRG); (b) Arumbera Sandstone (Amadeus) and Crossing Bore Schist (HRG); (c) Lower Stanovos Gneiss (HRG) and Heavitree Quartzite (Amadeus). Sample sizes (N) are indicated.

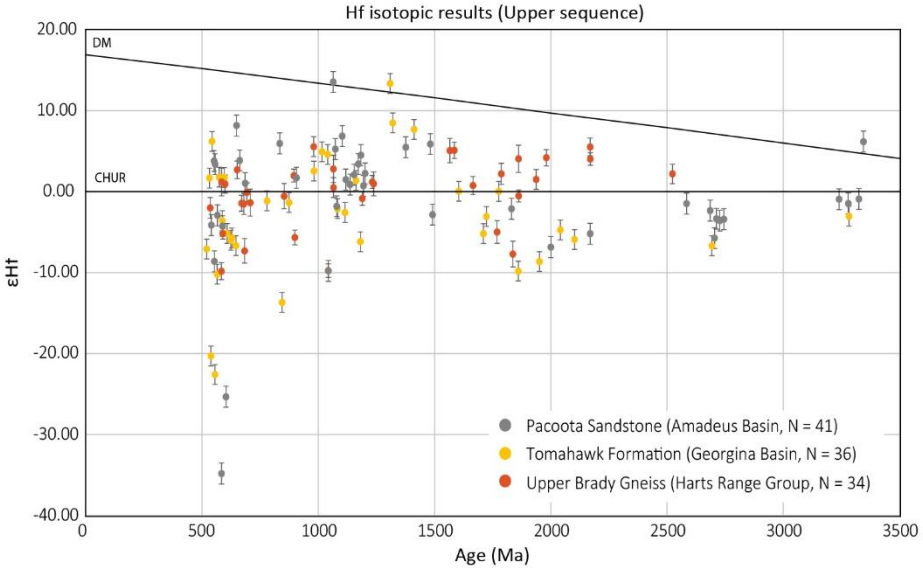
Hf isotopic results (Upper sequence)
DM
CHUR
εHf
Age (Ma)
Pacoota Sandstone (Amadeus Basin, N = 41)
Tomahawk Formation (Georgina Basin, N = 36)
Upper Brady Gneiss (Harts Range Group, N = 34)

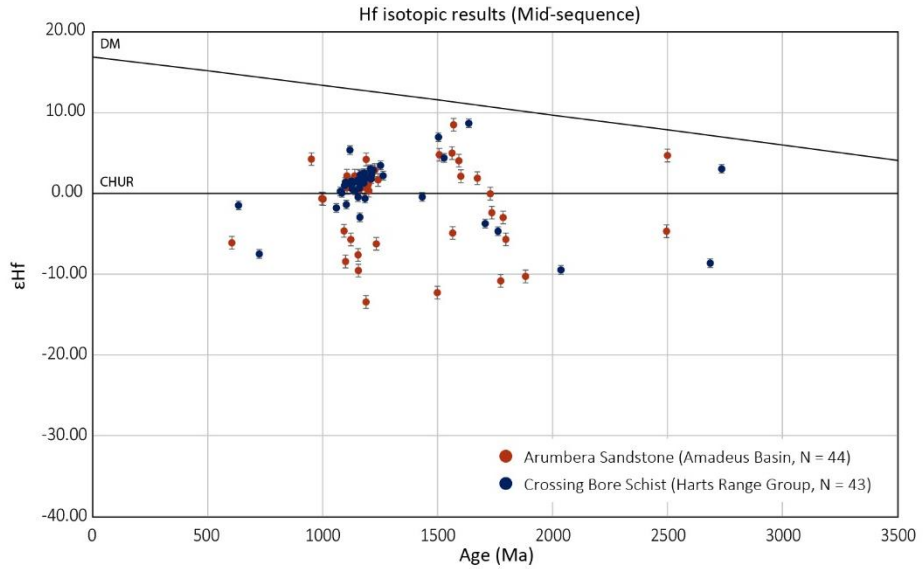
Hf isotopic results (Mid-sequence)
DM
CHUR
εHf
Age (Ma)
Arumbera Sandstone (Amadeus Basin, N = 44)
Crossing Bore Schist (Harts Range Group, N = 43)

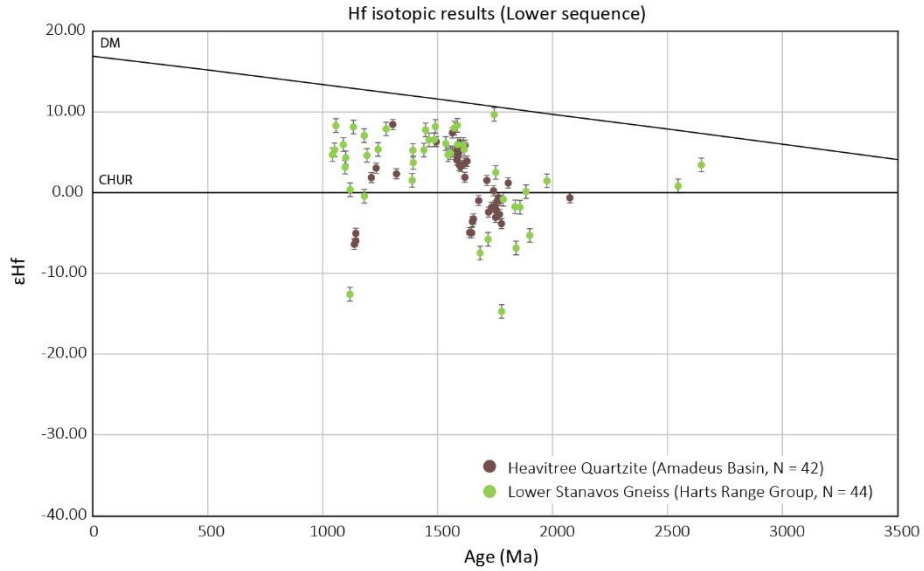
Hf isotopic results (Lower sequence)
DM
CHUR
εHf
Age (Ma)
Heavitree Quartzite (Amadeus Basin, N = 42)
Lower Stanavos Gneiss (Harts Range Group, N = 44)

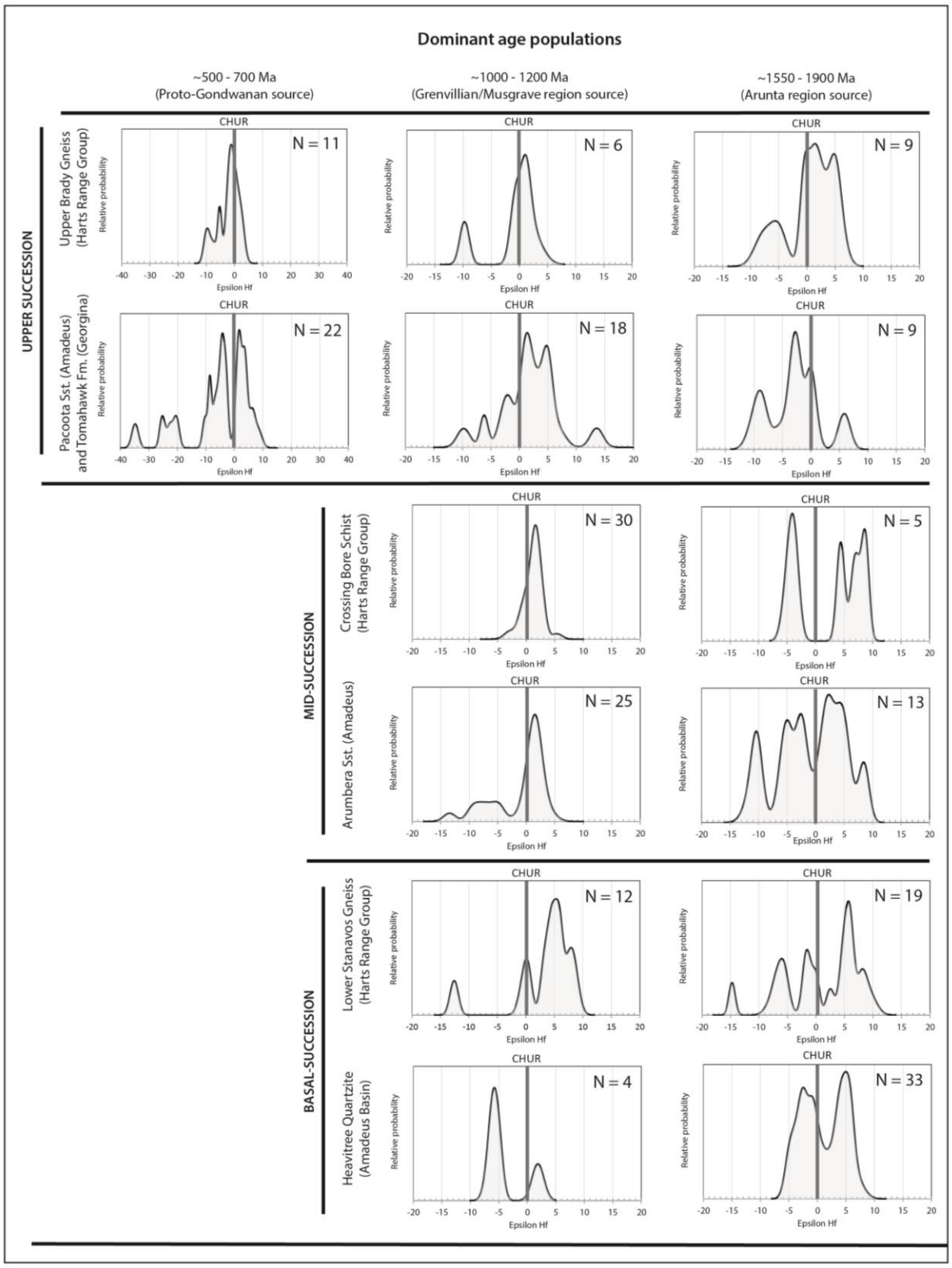

Figure 9. Lu–Hf isotope results: relative probability density plots for ε_{Hf} values. Individual relative probability density plots of epsilon hafnium (ε_{Hf}) values, relative to the chondrite uniform reservoir (CHUR) standard, of each sample grouped according to inferred dominant zircon age population 'events' (see also Fig. 8, Maidment *et al.* 2013) for proposed stratigraphic correlatives between the Harts Range Group, with those from the Amadeus and Georgina basins, at three separate depth intervals. If HRG protoliths were derived from the same magma source as their correlative basin sediments then the Hf zircon isotopic compositions should correspond for correlating sequences between the two regions. A particularly strong correlation is observed for the c. 1200–1000 Ma age bracket for samples from the mid succession. Sample sizes (N) are indicated.

4.2. Metamorphic geology

4.2.1. METAMORPHIC PETROLOGY

Samples were taken from the Upper and Lower Brady Gneiss, Irindina Gneiss and HRMC (Appendix A). Peak and retrograde mineral assemblages have been interpreted on the basis of grain size and microstructural context.

HRMC (Riddock Amphibolite Member)

Samples IG-16–28

These samples contain garnet, clinopyroxene, hornblende, ilmenite, plagioclase and quartz, and minor titanite, which define a predominantly coarse (2–6 mm) granoblastic texture. Samples IG-23 and IG-26 are sections through a large garnet crystal (~60 mm) but exhibit identical mineral relationships as remaining samples containing smaller garnet porphyroblasts (~2–7 mm, locally >10 mm). Garnet is often located within coarse migmatitic segregations (also Fig. 4a). Coarse-grained poikioblastic garnet contains inclusions of clinopyroxene, hornblende, quartz, and minor plagioclase and ilmenite. Clinopyroxene is coarse-grained (~2–4 mm), often exhibits fine orthopyroxene exsolution lamellae and contains inclusions of quartz and occasionally hornblende.

Three generations of hornblende are present. Foliated regions external to retrograde segregations are defined by a coarse gneissic layering of hornblende, and tonalitic plagioclase ± quartz domains, which also comprise the matrix. Minor clinopyroxene, garnet and ilmenite in contact with this hornblende do not exhibit retrograde reaction textures. Hornblende and plagioclase defining this fabric are denoted generation 1 and are considered as preserved prograde grains. In the earliest retrograde generation (generation 2), garnet is locally partially to completely isolated from clinopyroxene by a moderately coarse-grained coronae of hornblende adjacent to clinopyroxene, and sometimes hornblende–clinopyroxene symplectic

intergrowths, and also often plagioclase ± quartz coronae adjacent to garnet. Occurrence of very coarse-grained (4–6 mm) hornblende (generation 3) in contact with and spatially isolating much smaller relict garnet suggests that retrograde hornblende also pseudomorphed former coarser garnet porphyroblasts.

The peak metamorphic assemblage is interpreted to be garnet–clinopyroxene–hornblende–plagioclase–ilmenite–melt. Mineral relationships reflect development of garnet and clinopyroxene from breakdown of a prograde hornblende–plagioclase assemblage which is preserved in the externally foliated domains, and the subsequent reaction of garnet with clinopyroxene to form retrograde hornblende and plagioclase reaction textures. Post-peak mineral development is locally extensive, comprising variably retrogressed segregations within the matrix.

Figure 10. Photomicrographs of key petrological relationships. Harts Range Meta-Igneous Complex - (a) IG-16B: coarse-grained retrograde hornblende interpreted to have pseudomorphed a former garnet porphyroblast which now exists as relict subhedral garnet grains. (b) IG16A, (c) IG-28A and (d) IG-28B: garnet and clinopyroxene are systematically separated by a near-complete reaction rim of hornblende adjacent clinopyroxene sometimes with an additional corona of plagioclase ± quartz adjacent to garnet. Subhedral ilmenite grains are included within the retrograde hornblende and most are mantled by a partial coronal-symplectic intergrowth of titanate. (e) IG-26A: preservation of near-peak textural conditions as shown by clinopyroxene in direct contact with garnet with only minor effects of retrogression by growth of hornblende ± plagioclase reaction rims, generally around clinopyroxene. (f) IG-28A: externally foliated domains surround the regrogressed segregations, preserving prograde hornblende–plagioclase–quartz assemblages. **Irindina Gneiss metapelite -** (g) IG-10A: an aggregate of garnet porphyroblasts with minor ilmenite inclusions, are wrapped by a biotite-defined foliation which alternated with domains of plagioclase ± quartz, forming a coarse gneissic texture. (h) IG-222: a large garnet porphyroblast truncates and is wrapped by the coarse-grained biotite–sillimanite fabric. **Lower Brady Gneiss -** (i) BG-07A: densely aggregated fibrolitic sillimanite needles as inclusions within ganet porphyroblasts are aligned with the external foliation defined by biotite. **Upper Brady Gneiss -** (j) UBG-4B: garnet porphyroblast wrapped in the biotite fabric. (k) UBG-4A: showing the top portion of a large blocky aggregate of fibrous sillimanite. The spatial arrangement of the aggregate appears to mimic a former andalusite grain which has now been completely pseudomorphed. The individual sillimanite grains are aligned with the long axis of the former andalusite (approximately 20 mm x 10 mm), and are also aligned with the external fabric. **Strangways Metamorphic Complex basement -** (l) IG-30: reworked garnet porphyroblasts wrapped by a biotite–sillimanite foliation. Sample taken from mylonitised metapelite in the SW field area. Mineral abbreviations are shown with images. Abbreviations from Holland & Powell (1998).

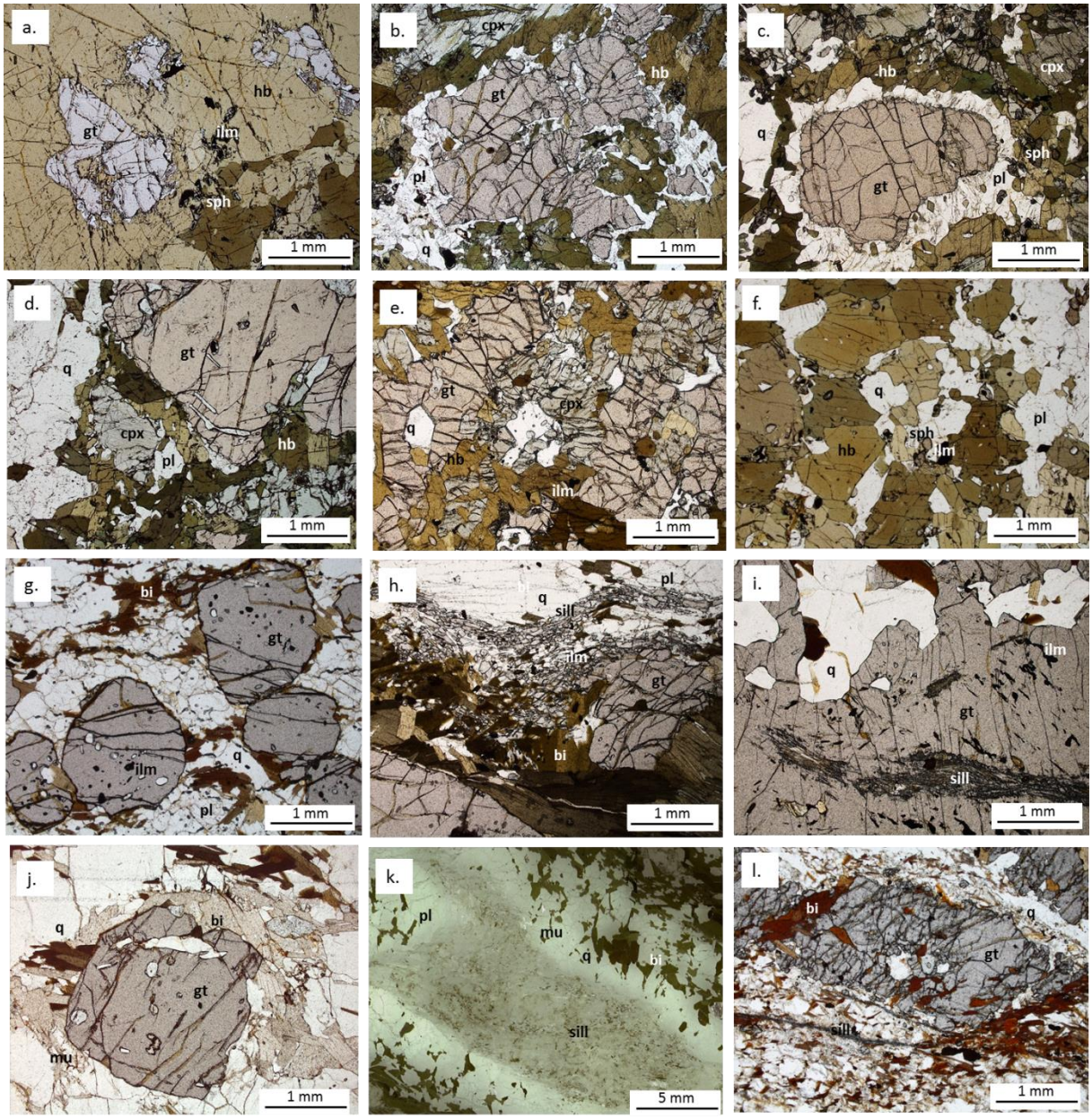

Irindina Gneiss (metapelite)

Samples IG-02, IG-10, IG-222

Sample IG-10 was taken from within the mapping area (Fig. 3) within the lower Irindina Gneiss at the contact with the HRMC. Samples IG-02 and IG-222 were taken from outside the mapping area at the contact between the Brady Gneiss and basement (Fig. 2), respectively, and are inferred to reflect stratigraphically higher and lower parts of the sequence relative to IG-10.

These samples contain garnet, biotite, plagioclase, quartz, rutile, minor ilmenite and chlorite and sample IG-222 also contains abundant sillimanite in the matrix. Coarse-grained euhedral garnet porphyroblasts (~1–4 cm, locally <10 cm) typically occur in aggregates and contain inclusions of biotite aligned with the external fabric, quartz, ilmenite, often rutile and fine-grained sillimanite. Coarse-grained biotite (0.5–3 mm) ± sillimanite (in IG-222) defines a pervasive fabric which is cross-cut by and partially wraps garnet. Biotite occurs in direct contact with ilmenite and rutile. The matrix is comprised of coarse anhedral quartz and subhedral tabular plagioclase (<5 mm) in approximately equal proportions.

The inferred peak mineral assemblage in sample IG-222 is garnet–sillimanite–biotite–plagioclase–quartz–rutile–ilmenite–melt. In samples IG-02 and IG-10 sillimanite is excluded from the peak mineral assemblage due to its absence in the matrix. Post-peak mineral development is limited and is confined to the occurrence of randomly oriented biotite and muscovite, and localised biotite alteration to chlorite.

Brady Gneiss

Samples BG-03, BG-07, BG-08, BG-09 & UBG-4

Samples BG-03–09 were taken from the central part of the Lower Brady Gneiss immediately to the north of the mapping area. Sample UBG-4 was also taken from outside the mapping area from within the highest preserved stratigraphy of the Upper Brady Gneiss (Fig. 2).

These samples contain garnet, sillimanite, biotite, muscovite, plagioclase, quartz, and ilmenite which all typically occur in contact. Porphyroblastic equant garnet (<35 mm) contain small subhedral grains of randomly interspersed ilmenite and subhedral quartz, sillimanite and coarse biotite and muscovite. The included fibrolitic sillimanite and coarse biotite are aligned parallel to the external fabric, defined by alternating coarse biotite–muscovite ±

fibrous sillimanite migmatitic domains, and quartz-rich quartz ± plagioclase layers (2–6 mm). Biotite occasionally contains thin muscovite grains aligned with the foliation and is often in contact with minor ilmenite. Sillimanite is disseminated as elongate aggregates within the matrix and also as inclusions within muscovite and occasionally plagioclase, and is significantly more abundant within samples from the Upper Brady Gneiss. Sample UBG-4A contains large (2–5 cm) rectangular psudomorphs of sillimanite interpreted to be after andalusite, in which individual sillimanite grains are themselves aligned with the long grain axis of the andalusite crystal (also Fig. 4). The matrix is comprised of quartz and minor plagioclase.

The inferred peak mineral assemblage is garnet–sillimanite–biotite–muscovite–plagioclase–quartz–ilmenite–melt with prograde development of sillimanite after andalusite. Post-peak mineral development is limited to the isolated occurrence of randomly-oriented biotite and muscovite growth at garnet grain edges in all samples.

4.2.2. GEOCHEMISTRY AND MINERAL CHEMISTRY

Whole-rock geochemical data are provided in Appendix C. Full analyses for electron-microprobe mineral compositions used for thermobarometry are given in Appendix D. Garnet analyses from the Brady Gneiss display slight core to rim decreases in manganese, reflecting the partial preservation of garnet growth zoning during prograde metamorphism whereas analyses from HRMC mafic granulite reflect increasing manganese and decreasing magnesium at the garnet rim consistent with reverse zoning during retrograde metamorphism (e.g. Spear and Peacock, 1989). Observed trends in garnet mineral chemistry are summarised in Table 3 and with Figure 11.

Table 3. Summary of garnet mineral chemistry from the Brady Gneiss and Harts Range Meta-Igneous Complex

	Brady Gneiss metapelite			Harts Range Meta-Igneous Complex mafic granulite			
Sample	UBG–4	BG-08	BG–07B	IG-26	IG–23	IG–16A	IG–28B
Garnet core							
X_{alm}	0.65–0.69	0.61–0.63	0.68–0.71	0.46–0.51	0.48–0.53	0.49–0.57	0.49–0.52
X_{py}	0.15–0.17	0.17–0.18	0.12–0.16	0.20–0.23	0.17–0.20	0.13–0.21	0.16–0.20
X_{sps}	0.10–0.15	0.12–0.13	0.08–0.10	0.02–0.03	0.02–0.03	0.02–0.06	0.03–0.04
X_{grs}	0.03–0.05	0.01–0.03	0.06–0.07	0.19–0.26	0.21–0.27	0.18–0.26	0.19–0.26
*Garnet near-rim**							
X_{alm}	0.65–0.69	0.64–0.65	0.70–0.74	-	-	-	-
X_{py}	0.16–0.17	0.16–0.17	0.13–0.15	-	-	-	-
X_{sps}	0.09–0.14	0.10–0.11	0.06–0.08	-	-	-	-
X_{grs}	0.00–0.01	0.00–0.06	0.00–0.07	-	-	-	-
Garnet rim							
X_{alm}	0.71–0.72	0.66–0.67	0.73–0.75	0.56–0.59	0.54–0.58	0.51–0.57	0.51–0.56
X_{py}	0.13–0.14	0.13–0.14	0.09–0.13	0.14–0.20	0.12–0.15	0.11–0.13	0.09–0.13
X_{sps}	0.09–0.10	0.10–0.12	0.06–0.08	0.02–0.06	0.04–0.06	0.06–0.08	0.06–0.09
X_{grs}	0.05–0.06	0.00–0.05	0.07–0.08	0.14–0.20	0.16–0.26	0.17–0.27	0.19–0.28

X_{alm} ($Fe^{2+}/(Fe^{2+} + Mg + Ca + Mn)$); X_{py} ($Mg/Mg + Fe^{2+} + Ca + Mn$)); X_{grs} ($Ca/Mg + Fe^{2+} + Ca + Mn$)); X_{sps} ($Mn/(Mg + Fe^{2+} + Ca + Mn$))

Garnet mineral compositions (of elements Fe, Mg, Ca and Mn) are expressed as mole fractions, X, (abbreviations as above, mole fraction x 100 = mole %) recalculated from electron microprobe analyses (see Appendix D). A composition range is shown which consists of 5–10 microprobe point analyses from several garnet grains within each sample.

*Near-rim analyses are located approximately 1/3 garnet grain diameter from the grain edge. Near-rim analyses were not conducted for mafic granulite samples. Garnet rim analyses are located within 10 µm of the garnet grain edge.

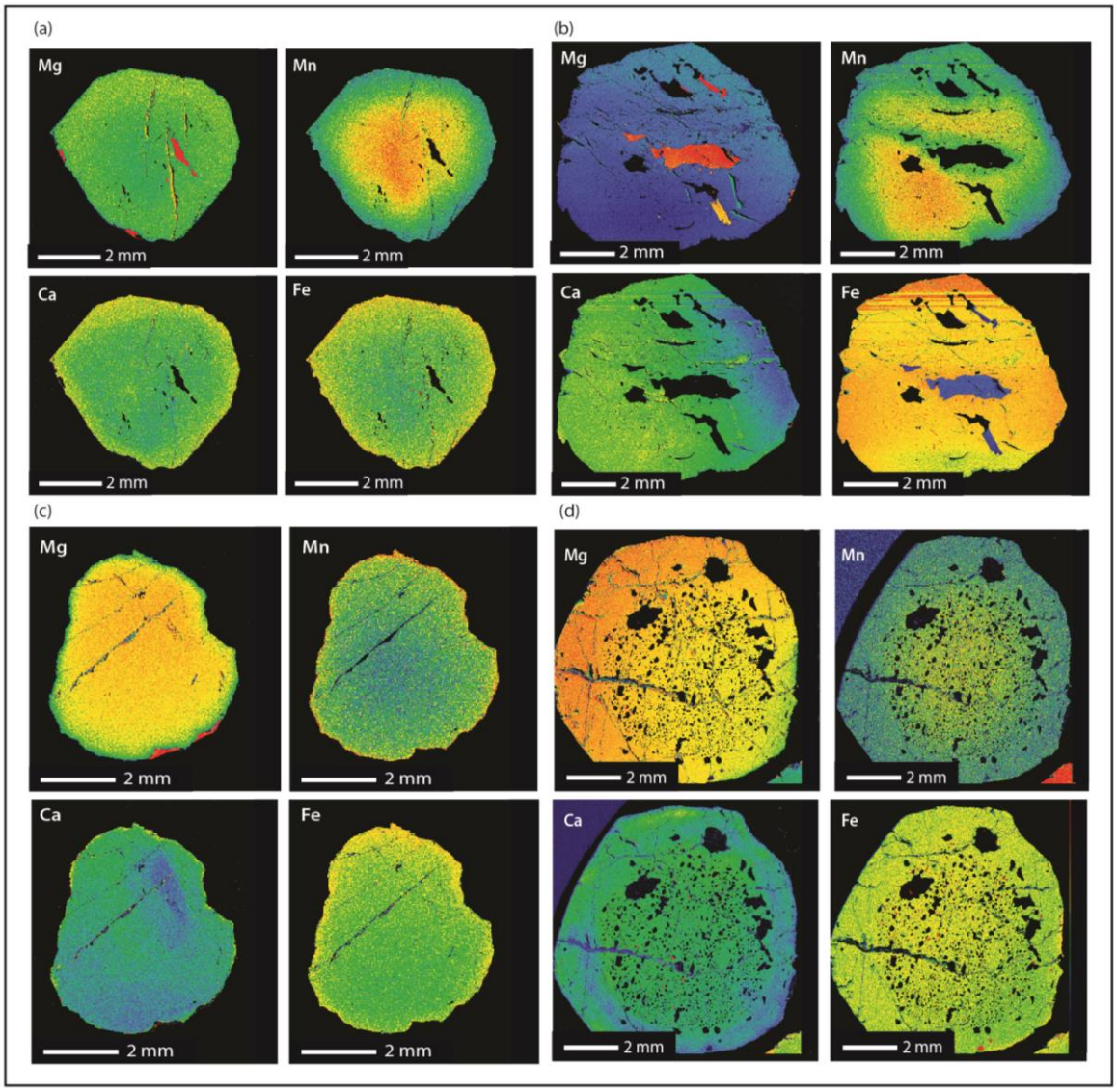

Figure 11. Electron microprobe elemental x-ray maps of Mg, Mn, Ca and Fe for garnet from the Brady Gneiss and Irindina Gneiss metapelite. Qualitative elemental x-ray maps are shown for garnet grains from sample (a) UBG-4 (Upper Brady Gneiss), (b) BG-07 (Lower Brady Gneiss), (c) IG-02 (upper Irindina Gneiss) and (d) IG-10 (lower Irindina Gneiss). Colour gradient from blue to red reflects an increasing concentration of that particular element. Sample UBG-4 shows a manganese decrease from core to rim whereas iron, magnesium and calcium show very slight increases. Garnet in samples BG-07 and IG-10 are larger and from lower in the sequence than sample UBG-4, and have a largely homogenous composition for iron, magnesium and calcium, however they likewise show a slight decrease in manganese towards the rim. Similar trends are confirmed in electron-microprobe analyses of garnet from the Brady Gneiss (see Table 3) which display slight core to rim zonation with overall small increases in X_{alm}, and consistently decreasing X_{py} and X_{sps}. Observed core to rim decreases in manganese are consistent with garnet growth zoning during prograde metamorphism (e.g. Spear and Peacock 1989). Sample IG-02 is approximately the same size as sample UBG-4 but from lower in the sequence at a structural level between BG-07 and IG-10. In constrast to these other samples, elemental mapping shows a sharp increase in manganese and decrease in magnesium at the garnet rim. This is consistent with reverse zoning during retrograde metamorphism (e.g. Spear 1993) associated with partial garnet resorption by Mg-rich matrix minerals. Microprobe analyses of garnet from the Harts Range Meta-Igneous Complex mafic granulites (see Table 3) reflect similar trends with well-defined core to rim reverse zonation by increasing X_{alm}, X_{grs} and X_{sps}, and decreasing X_{py}.

4.2.3. PRESSURE–TEMPERATURE CONDITIONS

4.2.3.1. Thermobarometry

The results of average P–T calculations are summarised in Table 4. P–T calculations were undertaken to evaluate the difference in peak metamorphic conditions between the upper and lower parts of the HRG. Calculations were made using the compositions from the interiors of garnets, combined with compositions from cores of matrix minerals away from garnet to minimise the effects of retrograde re-equilibration. Garnet analyses from the Brady Gneiss indicate partial preservation of prograde growth zoning (i.e. Fig. 11) and therefore near-rim compositions were selected as reflecting more realistic peak mineral compositions. Mean calculations for the average P–T results of peak metamorphic conditions are 887 ± 52ºC (2σ) and 10.5 ± 0.9 kbar (2σ) for the HRMC mafic granulites, and 677 ± 34ºC (2σ) and 7.3 ± 1.3 kbar (2σ) for the Brady Gneiss. These calculations are in agreement with P–T estimates undertaken in previous work from the Harts Range (Miller *et al.* 1997; Mawby *et al.* 1999).

4.2.3.2. Pressure–temperature pseudosections

P–T pseudosections were calculated for metapelites from the Upper Brady Gneiss (UBG-4) and Irindina Gneiss (IG-10 & IG-222), in order to further assess the difference in metamorphic pressure between the upper and lower HRG stratigraphic section. In sample UBG-4, the garnet stability field is broady V-shaped, and the range of stable temperatures widens as pressure increases above ~3 kbar and 640ºC. The andalusite stability field occurs below ~4 kbar and 650ºC and increases with decreasing pressure and temperature. The garnet–sillimanite–plagioclase–biotite–muscovite–liquid–quartz–ilmenite assemblage defines the peak P–T assemblage with the peak field stable within the P-T range of ~660–730ºC and 5–8 kbar (Fig. 12).

Table 4. THERMOCALC average P–T results for peak metamorphic assemblages of the Brady Gneiss and Harts Range Meta-Igneous Complex

Sample	T (°C)	1σ	P (kbar)	1σ	a_{H2O}	Correl.	Fit	NR	Endmembers removed
Mafic granulites - Harts Range Meta-Igneous Complex									
IG-16A	878	71	11.0	1.2	0.4	0.562	1.31	9	Geik
IG-16B	879	78	10.1	1.3	0.4	0.576	1.33	8	Geik
IG-23A	819	70	10.1	1.1	0.4	0.485	1.41	9	Parg
IG-23B	930	80	11.0	1.3	0.4	0.536	1.33	9	Geik
IG-26A	893	69	9.8	1.2	0.4	0.546	1.17	8	Geik
IG-26B	937	66	11.3	1.1	0.4	0.528	1.18	10	Geik
IG-28A	837	64	10.3	1.5	0.4	0.236	1.10	6	Parg
IG-28B	920	86	10.5	1.6	0.4	0.557	1.23	7	Geik
Average (2σ)	887	52	10.5	0.9					
Brady Gneiss metapelites									
Upper Brady Gneiss									
UBG-4B	710	34	7.4	1.2	0.8	0.848	0.80	7	-
Lower Brady Gneiss									
BG-07B	668	27	7.4	1.1	0.8	0.897	0.98	9	-
BG-08	654	27	7.0	1.1	0.8	0.882	1.00	7	-
Average (2σ)	677	34	7.3	1.3					

a_{H2O}, fluid activity composition used; σ, standard deviation; Correl., correlation between P and T uncertainties; Fit, a goodness of fit parameter describing the average of n equilibria (Powell & Holland, 1988); NR, number of independent equilibria reactions calculated by THERMOCALC; endmembers removed, mineral endmembers which were removed from calculations to improve the fit of the P-T estimate to pass at 95% confidence; Geik, abbreviation for geikielite (endmember of ilmenite); Parg, abbreviation for pargasite (endmember of hornblende).

In samples IG-10 and IG-222 the garnet stability field extends over the entire pseudosection, the rutile stability field extends above ~7 kbar and the sillimanite stability field occurs below ~750ºC and decreases with decreasing pressure. For samples IG-10 and IG-222, the andalusite stability field is small, extending only below ~4kbar and 580ºC. The peak field for IG-10 is narrow and defined by garnet–plagioclase–biotite–liquid–quartz–ilmenite–rutile between ~760–790ºC and 6.5–9 kbar (Fig. 13). The peak assemblage in sample IG-222 is defined by garnet–plagioclase–biotite–sillimanite–liquid–quartz–ilmenite–rutile which occurs at ~700–770ºC and 7.5–9.5 kbar (Fig. 14).

The P–T path is inferred from changes in mineral abundances, X_{alm} and X_{sps} compositional isopleths in garnet, and X_{Ca} compositional isopleths for plagioclase. Compositions of representative electron microprobe analyses of garnet for sample UBG-4 also provide

additional constraints on the P–T evolution for this sample (refer to Fig. 11). Andalusite-sillimanite textural relationships (e.g. Fig. 4 & 10) for all samples are also used to infer a prograde P–T path in which andalusite abundance decreases with the appearance of sillimanite. Modal garnet proportions reflect increasing garnet abundance with increasing pressure along the prograde P–T paths, consistent with preserved prograde zonation involving Mn depletion at garnet rims (Fig. 11, Spear 1993).

Retrograde mineral development is limited in sample UBG-4 and accordingly the retrograde P–T path has not been constrained. Minor post-peak mineral development, the absence of kyanite, and likewise the absence of cordierite in samples IG-10 and IG-222, constrains the probable retrograde path to above the cordierite-in, but below kyanite-in stability fields, reflecting decompressive cooling towards ~600°C and 5 kbar.

4.2.4. LA-ICP-MS MONAZITE U–PB GEOCHRONOLOGY

In situ U–Pb monazite geochronology was done on samples BG-07 and BG-09 from the Lower Brady Gneiss. Monazite is abundant within matrix biotite and also as inclusions within garnet. Twenty analyses were obtained from 10 grains located within garnet, and 18 analyses from 10 grains located in the foliated matrix (Table 5). Data are presented on a Terra-Wasserburg Concordia diagram and probability density plot of $^{206}Pb/^{238}U$ age (Fig. 15). U–Pb analyses reveal a broad age spectrum (c. 340–480 Ma) with similar ages obtained from both included and matrix monazite. Due to observable levels of common lead, only the most concordant analyses have been used to calculate a weighted average $^{206}Pb/^{238}U$ age of 442.4 ± 9.1 Ma.

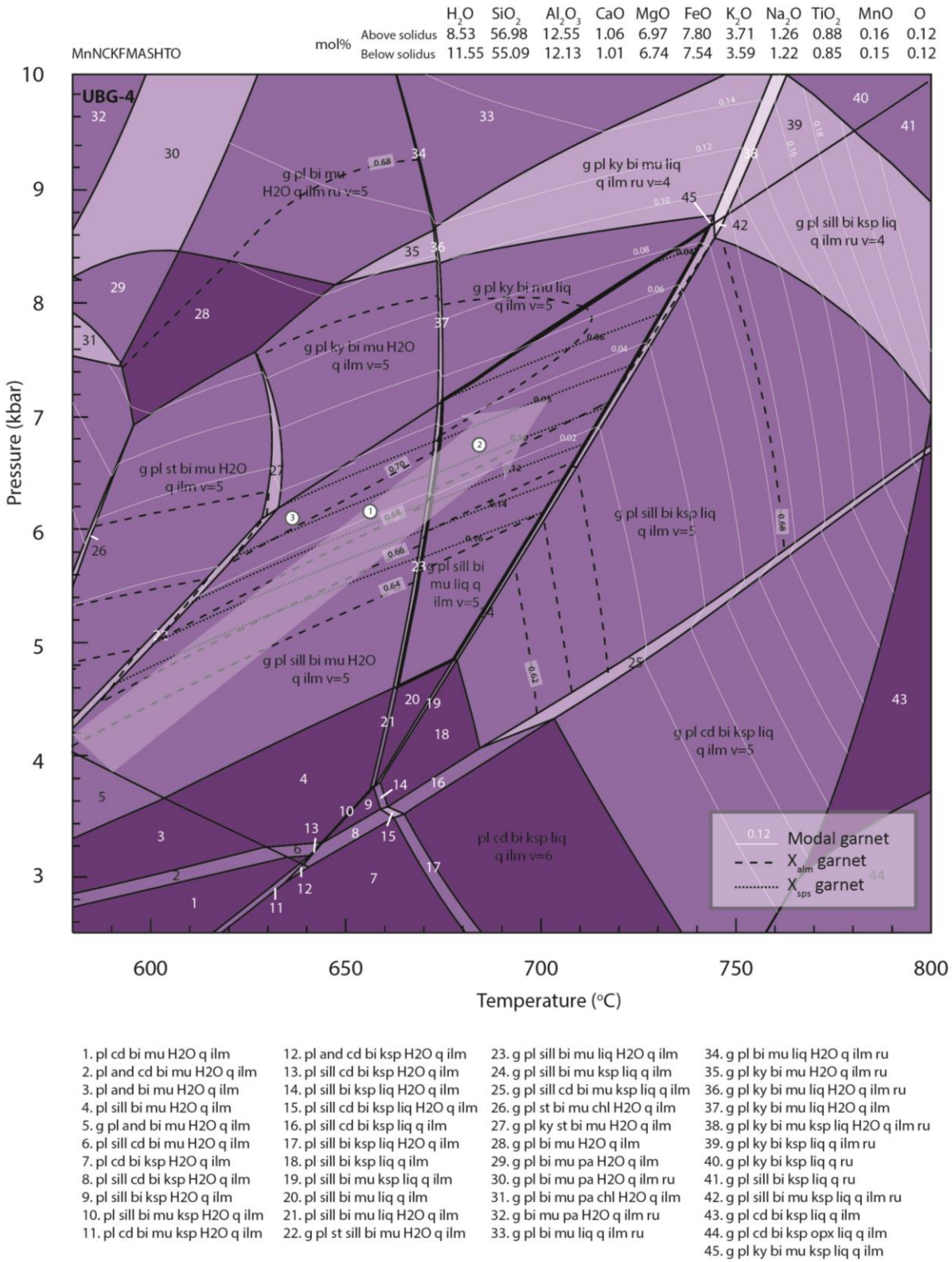

1. pl cd bi mu H2O q ilm
2. pl and cd bi mu H2O q ilm
3. pl and bi mu H2O q ilm
4. pl sill bi mu H2O q ilm
5. g pl and bi mu H2O q ilm
6. pl sill cd bi mu H2O q ilm
7. pl cd bi ksp H2O q ilm
8. pl sill cd bi ksp H2O q ilm
9. pl sill bi ksp H2O q ilm
10. pl sill bi mu ksp H2O q ilm
11. pl cd bi mu ksp H2O q ilm
12. pl and cd bi ksp H2O q ilm
13. pl sill cd bi ksp H2O q ilm
14. pl sill bi ksp liq H2O q ilm
15. pl sill cd bi ksp liq H2O q ilm
16. pl sill cd bi ksp liq q ilm
17. pl sill bi ksp liq H2O q ilm
18. pl sill bi ksp liq q ilm
19. pl sill bi mu ksp liq q ilm
20. pl sill bi mu liq q ilm
21. pl sill bi mu liq H2O q ilm
22. g pl st sill bi mu H2O q ilm
23. g pl sill bi mu liq H2O q ilm
24. g pl sill bi mu ksp liq q ilm
25. g pl sill cd bi mu ksp liq q ilm
26. g pl st bi mu chl H2O q ilm
27. g pl ky st bi mu H2O q ilm
28. g pl bi mu H2O q ilm
29. g pl bi mu pa H2O q ilm
30. g pl bi mu pa H2O q ilm ru
31. g pl bi mu pa chl H2O q ilm
32. g bi mu pa H2O q ilm ru
33. g pl bi mu liq q ilm ru
34. g pl bi mu liq H2O q ilm ru
35. g pl ky bi mu H2O q ilm ru
36. g pl ky bi mu liq H2O q ilm ru
37. g pl ky bi mu liq H2O q ilm
38. g pl ky bi mu ksp liq H2O q ilm ru
39. g pl ky bi ksp liq q ilm ru
40. g pl ky bi ksp liq q ru
41. g pl sill bi ksp liq q ru
42. g pl sill bi mu ksp liq q ilm ru
43. g pl cd bi ksp liq q ilm
44. g pl cd bi ksp opx liq q ilm
45. g pl ky bi mu ksp liq q ilm

Figure 12. Calculated P–T pseudosection for sample UBG-4 from the Upper Brady Gneiss.
Bulk compositions are given in the top right of the diagram and expressed as mole percent. The field garnet–plagioclase–sillimanite–biotite–muscovite–liquid–quartz–ilmenite, outlined in bold, indicates the peak P–T conditions of the sample; the arrow represents the interpreted prograde P–T path. Garnet modal proportions (modal proportions x 100 = modal %), garnet X_{alm} (Fe^{2+}/ (Fe^{2+} + Mg + Ca + Mn)) and X_{sps} (Mn/ (Mg + Fe^{2+} + Ca + Mn)) compositional isopleths are shown. The solid white circles correspond to representative core (1), near-rim (2) and rim (3) electron microprobe analysis of a garnet from sample UBG-4B (see also Appendix D). The near-rim analysis is interpreted to reflect a more realistic peak metamorphism garnet composition (refer to section 4.2.3.1.), and so further constrains the prograde P–T path. Mineral abbreviations from Holland & Powell (1998).

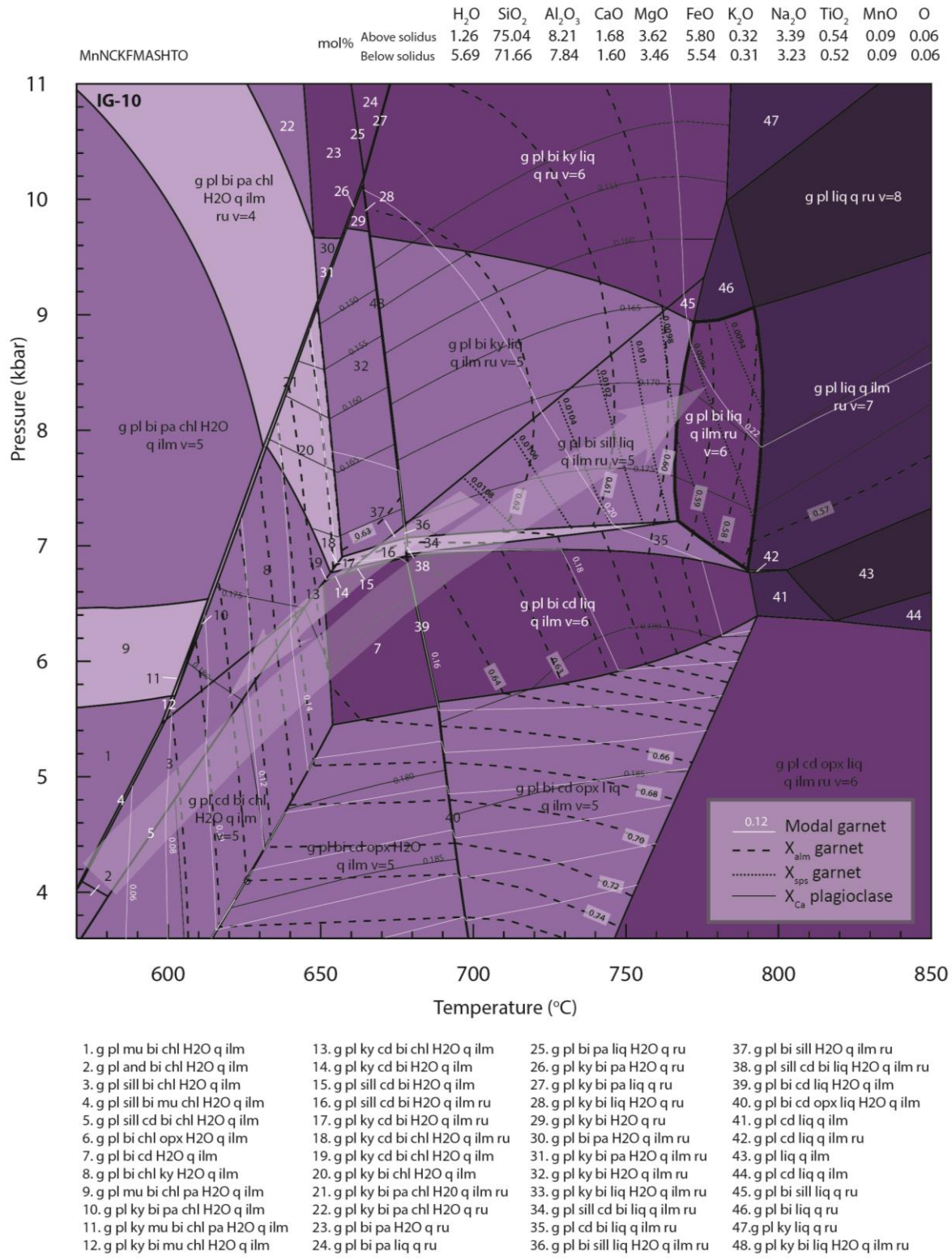

1. g pl mu bi chl H2O q ilm
2. g pl and bi chl H2O q ilm
3. g pl sill bi chl H2O q ilm
4. g pl sill bi mu chl H2O q ilm
5. g pl sill cd bi chl H2O q ilm
6. g pl bi chl opx H2O q ilm
7. g pl bi cd H2O q ilm
8. g pl bi chl ky H2O q ilm
9. g pl mu bi chl pa H2O q ilm
10. g pl ky bi pa chl H2O q ilm
11. g pl ky mu bi chl pa H2O q ilm
12. g pl ky bi mu chl H2O q ilm
13. g pl ky cd bi chl H2O q ilm
14. g pl ky cd bi H2O q ilm
15. g pl sill cd bi H2O q ilm
16. g pl sill cd bi H2O q ilm ru
17. g pl ky cd bi H2O q ilm ru
18. g pl ky cd bi chl H2O q ilm ru
19. g pl ky cd bi chl H2O q ilm
20. g pl ky bi chl H2O q ilm
21. g pl ky bi pa chl H20 q ilm ru
22. g pl ky bi pa chl H2O q ru
23. g pl bi pa H2O q ru
24. g pl bi pa liq q ru
25. g pl bi pa liq H2O q ru
26. g pl ky bi pa H2O q ru
27. g pl ky bi pa liq q ru
28. g pl ky bi liq H2O q ru
29. g pl ky bi H2O q ru
30. g pl bi pa H2O q ilm ru
31. g pl ky bi pa H2O q ilm ru
32. g pl ky bi H2O q ilm ru
33. g pl ky bi liq H2O q ilm ru
34. g pl sill cd bi liq q ilm ru
35. g pl cd bi liq q ilm ru
36. g pl bi sill liq H2O q ilm ru
37. g pl bi sill H2O q ilm ru
38. g pl sill cd bi liq H2O q ilm ru
39. g pl bi cd liq H2O q ilm
40. g pl bi cd opx liq H2O q ilm
41. g pl cd liq q ilm
42. g pl cd liq q ilm ru
43. g pl liq q ilm
44. g pl cd liq q ilm
45. g pl bi sill liq q ru
46. g pl bi liq q ru
47.g pl ky liq q ru
48. g pl ky bi liq H2O q ilm ru

Figure 13. Calculated P–T pseudosection for sample IG-10 from mid-lower metapelitic Irindina Gneiss. Bulk compositions are given in the top right of the diagram and expressed as mole percent. The field garnet–plagioclase–biotite–liquid–quartz–ilmenite–rutile, outlined in bold, indicates the peak P–T conditions of this sample. The large and small arrows represent the interpreted prograde and retrograde P–T paths, respectively. Garnet modal proportions and X_{alm} (Fe^{2+}/ (Fe^{2+} + Mg + Ca + Mn)) and X_{sps} (Mn/ (Mg + Fe^{2+} + Ca + Mn)) compositional isopleths, and plagioclase X_{Ca} (Ca/ (Ca + Na)) isopleths are shown. Mineral abbreviations from Holland & Powell (1998).

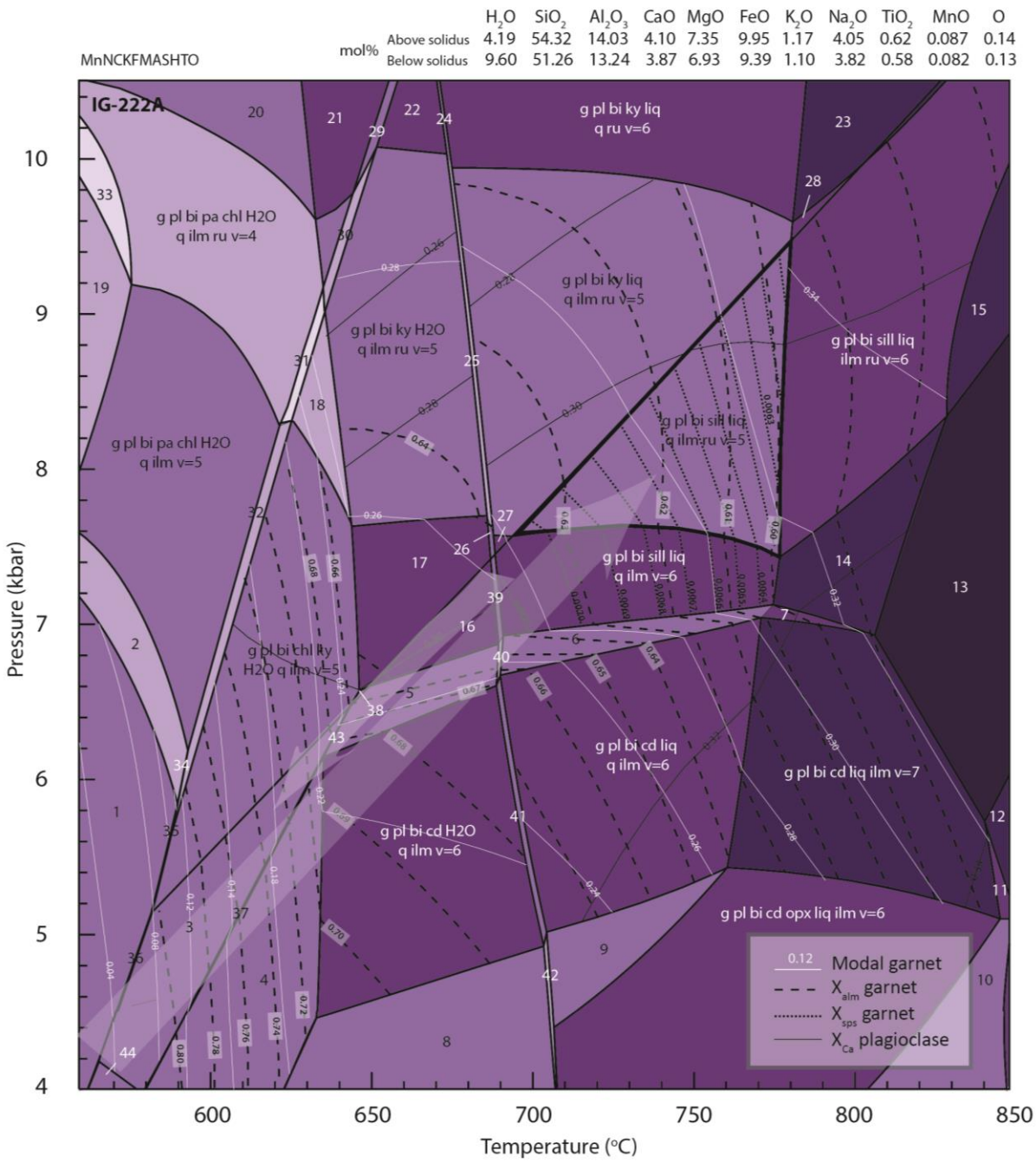

1. g pl mu bi chl H2O q ilm
2. g pl mu bi chl pa H2O q ilm
3. g pl sill bi chl H2O q ilm
4. g pl cd bi chl H2O q ilm
5. g pl sill cd bi H2O q ilm
6. g pl sill cd bi liq q ilm
7. g pl sill cd bi liq ilm
8. g pl bi cd opx H2O q ilm
9. g pl bi cd opx liq q ilm
10. g pl bi cd opx sp liq ilm
11. g pl bi cd sp liq ilm
12. g pl bi sp liq ilm
13. g pl bi liq ilm
14. g pl sill bi liq ilm
15. g pl bi liq ilm ru
16. g pl sill bi H2O q ilm
17. g pl ky bi H2O q ilm
18. g pl ky bi chl H2O q ilm ru
19. g pl bi pa chl zo H2O q ilm
20. g pl bi pa chl H2O q ru
21. g pl bi pa H2O q ru
22. g pl ky bi H2O q ru
23. g pl ky bi liq ru
24. g pl ky bi liq H2O q ru
25. g pl ky bi liq H2O q ilm ru
26. g pl ky bi liq H2O q ilm
27. g pl ky bi liq q ilm
28. g pl ky liq ilm ru
29. g pl ky bi pa H2O q ru
30. g pl ky bi pa H2O q ilm ru
31. g pl ky bi pa chl H2O q ilm ru
32. g pl ky bi pa chl H2O q ilm
33. g pl bi pa chl zo H2O q ilm ru
34. g pl ky bi mu pa chl H2O q ilm
35. g pl ky bi mu chl H2O q ilm
36. g pl sill bi mu chl H2O q ilm
37. g pl sill cd bi chl H2O q ilm
38. g pl ky cd bi H2O q ilm
39. g pl sill bi liq H2O q ilm
40. g pl sill cd bi liq H2O q ilm
41. g pl cd bi liq H2O q ilm
42. g pl cd bi opx liq H2O q ilm
43. g pl sill cd bi chl H2O q ilm
44. g pl and bi chl H2O q ilm

Figure 14. Calculated P–T pseudosection for sample IG-222 from the lower metapelitic Irindina Gneiss. Bulk compositions are given in the top right of the diagram and expressed as mole percent. The field garnet–plagioclase–sillimanite–biotite–liquid–quartz–ilmenite–rutile, outlined in bold, indicates the peak P–T conditions of this sample. The large and small arrows represent the interpreted prograde and retrograde P–T paths, respectively. Garnet modal proportions and X_{alm} (Fe^{2+}/ (Fe^{2+} + Mg + Ca + Mn)) and X_{sps} (Mn/ (Mg + Fe^{2+} + Ca + Mn)) compositional isopleths, and plagioclase X_{Ca} (Ca/ (Ca + Na)) isopleths are shown. Mineral abbreviations from Holland & Powell (1998).

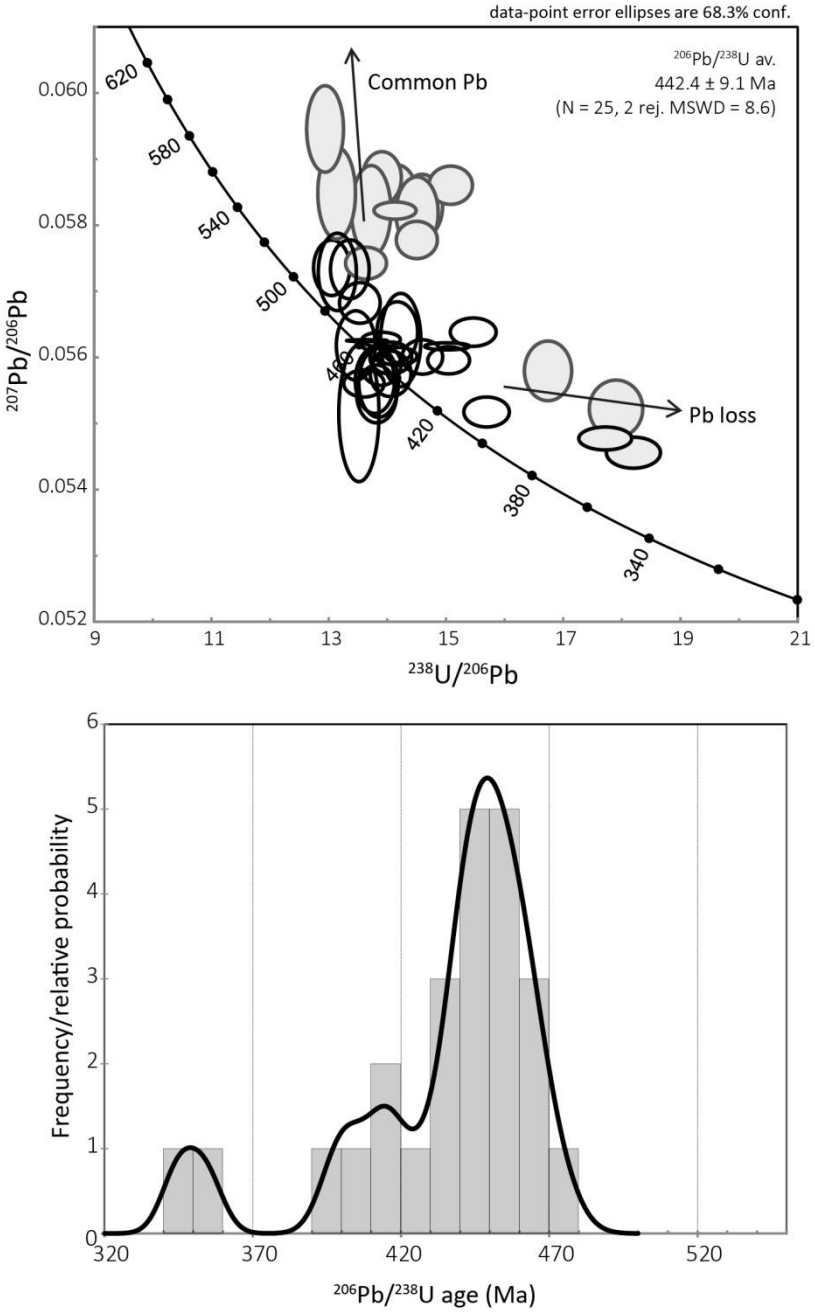

Figure 15. *In situ* LA-ICP-MS monazite U–Pb geochronology. (a) Terra-Wasserburg Concordia plot for all matrix and included (within garnet) monazite analyses from samples BG-07 and BG-09 from the Lower Brady Gneiss. The most concordant analyses (n = 25, conc. 100 ± 2%), are shown with black outlines, and lesser concordant analyses (> 2% disc.) outlined grey. Common Pb and Pb-loss trends are shown. Due to observable levels of common Pb and Pb-loss in some grains, only the most concordant population (n = 25, 2 statistical outliers removed) have been used to calculate the $^{206}Pb/^{238}U$ weighted average age of 442.4 ± 9.1 Ma. Analyses which were not used for the weighted mean age calculation are shaded grey; analyses which were incorporated in the calculation have their ellipses unfilled for clarity. (b) Cumulative frequency histogram and probability density plot for all concordant analyses (n = 25, conc. 100 ± 2%).

Table 5. *In situ* LA-ICP-MS monazite U–Pb geochronology results

Analysis	$^{207}Pb/^{206}Pb$	1σ	$^{206}Pb/^{238}U$	1σ	$^{207}Pb/^{235}U$	1σ	% Conc.	$^{207}Pb/^{206}Pb$ age (Ma)	1σ	$^{206}Pb/^{238}U$ age (Ma)	1σ	$^{207}Pb/^{235}U$ age (Ma)	1σ	$^{204}Pb/^{206}Pb$ (%)	Rho (ρ)
Included monazite															
Sample BG-07															
17_1	0.05630	0.00060	0.07197	0.00112	0.55838	0.00872	101	463.5	23.53	448.0	6.75	450.5	5.68	0.00	0.99651
17_2	0.05598	0.00062	0.06646	0.00104	0.51276	0.00812	101	451.4	23.86	414.8	6.28	420.3	5.45	0.03	0.98817
17_3	0.05605	0.00060	0.07056	0.00110	0.54499	0.00854	101	453.9	23.15	439.5	6.64	441.7	5.61	0.01	0.99487
17_4	0.05604	0.00062	0.06850	0.00107	0.52898	0.00842	101	453.6	24.13	427.1	6.47	431.1	5.59	0.01	0.98134
18_1	0.05643	0.00069	0.07057	0.00114	0.54862	0.00934	101	468.5	27.10	439.6	6.84	444.1	6.12	0.08	0.94888
18_2	0.05829	0.00080	0.07286	0.00118	0.58488	0.01050	103	540.0	30.30	453.3	7.10	467.6	6.73	0.10	0.90213
4_1	0.05857	0.00068	0.07070	0.00111	0.57061	0.00929	104	551.1	25.18	440.4	6.70	458.4	6.01	0.04	0.96433
4_2	0.05875	0.00068	0.07190	0.00113	0.58209	0.00951	104	558.0	25.21	447.6	6.82	465.8	6.10	0.01	0.96196
4_3	0.05832	0.00072	0.06853	0.00109	0.55078	0.00926	104	541.3	27.53	427.3	6.55	445.5	6.06	0.04	0.94605
4_4	0.05632	0.00079	0.07028	0.00112	0.54521	0.00979	101	464.4	31.09	437.8	6.75	441.9	6.43	0.00	0.88750
8_1	0.05817	0.00074	0.06893	0.00113	0.55301	0.00969	104	535.8	28.06	429.7	6.79	447.0	6.33	0.02	0.93558
1_1	0.05515	0.00096	0.07399	0.00124	0.56265	0.01171	99	418.3	38.01	460.2	7.44	453.3	7.61	0.03	0.80525
12_1	0.00131	0.01504	0.05351	0.01200	0.00961	0.11022	3	0.1	0.00	336.1	73.42	9.7	110.85	62.30	0.01955
Sample BG-09															
9_1	0.05781	0.00065	0.06895	0.00110	0.54928	0.00894	103	522.3	24.66	429.8	6.60	444.5	5.86	0.01	0.98020
9_2	0.05565	0.00072	0.07220	0.00116	0.55365	0.00953	100	438.0	27.89	449.4	6.95	447.4	6.23	0.01	0.93339
8a_1	0.05861	0.00066	0.06631	0.00108	0.53582	0.00890	105	552.7	24.55	413.9	6.51	435.7	5.88	0.03	0.98056
8b_1	0.05620	0.00071	0.07428	0.00121	0.57540	0.01002	100	459.4	28.07	461.9	7.26	461.5	6.46	0.00	0.93544
10_1	0.05589	0.00064	0.07199	0.00117	0.55473	0.00924	100	447.7	24.76	448.1	7.02	448.1	6.03	0.00	0.97572
17a_1	0.05735	0.00070	0.07485	0.00122	0.59169	0.01011	101	504.4	26.52	465.3	7.30	471.9	6.45	0.03	0.95392
17b_1	0.05546	0.00068	0.07237	0.00118	0.55328	0.00947	99	430.7	26.84	450.4	7.07	447.1	6.19	0.01	0.95262
17b_2	0.05730	0.00074	0.07606	0.00124	0.60085	0.01060	101	502.7	28.33	472.5	7.43	477.8	6.72	0.00	0.92411
Matrix monazite															
Sample BG-07															
6_1	0.05581	0.00068	0.05973	0.00095	0.45952	0.00771	103	444.5	26.27	374.0	5.80	383.9	5.37	0.03	0.94794
16_1	0.05566	0.00070	0.07253	0.00116	0.55651	0.00948	100	438.5	27.29	451.4	6.95	449.3	6.18	0.02	0.93887
16_2	0.05851	0.00082	0.07613	0.00123	0.61393	0.01103	103	548.8	30.34	473.0	7.34	486.0	6.94	0.01	0.89928
14_1	0.05950	0.00080	0.07729	0.00124	0.63362	0.01116	104	585.5	29.06	479.9	7.40	498.3	6.94	0.04	0.91088
14_2	0.05738	0.00068	0.07662	0.00120	0.60593	0.00993	101	505.6	25.86	475.9	7.20	481.0	6.28	0.04	0.95568
Sample BG-09															
1a_1	0.05641	0.00062	0.06466	0.00108	0.50267	0.00849	102	467.7	24.46	403.9	6.55	413.5	5.73	0.02	0.98892
1a_2	0.05620	0.00061	0.06658	0.00112	0.51563	0.00868	102	459.5	24.05	415.5	6.76	422.2	5.81	0.04	0.99929
1b_1	0.05459	0.00061	0.05495	0.00092	0.41337	0.00702	102	395.4	24.70	344.8	5.63	351.3	5.04	0.02	0.98588
3a_1	0.05825	0.00064	0.07076	0.00119	0.56804	0.00959	104	538.5	24.31	440.8	7.15	456.7	6.21	0.02	0.99614
3b_1	0.05628	0.00061	0.07325	0.00123	0.56816	0.00954	100	462.9	23.88	455.7	7.36	456.8	6.18	0.01	0.99995
3b_2	0.05563	0.00061	0.07352	0.00123	0.56368	0.00953	99	437.3	23.84	457.3	7.40	453.9	6.19	0.00	0.98955
4_1	0.05480	0.00061	0.05644	0.00095	0.42625	0.00723	102	403.9	24.32	354.0	5.79	360.5	5.15	0.03	0.99235
4_2	0.05525	0.00068	0.05586	0.00094	0.42533	0.00749	103	422.0	26.99	350.4	5.73	359.9	5.34	0.00	0.95559
16a_1	0.05601	0.00062	0.07112	0.00119	0.54905	0.00932	100	452.5	24.16	442.9	7.18	444.4	6.11	0.01	0.98571
16a_2	0.05745	0.00065	0.07333	0.00124	0.58062	0.00995	102	508.3	24.77	456.2	7.44	464.9	6.39	0.02	0.98675
16b_1	0.05685	0.00066	0.07390	0.00125	0.57901	0.01001	101	484.9	25.60	459.6	7.48	463.8	6.43	0.01	0.97840
12_1	0.05519	0.00061	0.06372	0.00104	0.48475	0.00802	101	419.8	24.44	398.2	6.30	401.3	5.48	0.01	0.98651
12_2	0.05578	0.00064	0.07114	0.00116	0.54686	0.00919	100	443.3	25.00	443.0	6.99	442.9	6.03	0.02	0.97030

5. DISCUSSION

The objective of this study is to understand the tectonic context in which burial and metamorphism of the Harts Range protoliths occurred. This requires an understanding of the sequence correlations between the HRG and the surrounding basins, as well as an evaluation of the structural-lithological and metamorphic character of the HRG sequences.

5.1. Provenance

Similarities between the detrital zircon age spectra and temporal changes in age distribution from the base to uppermost HRG and late Neoproterozoic–Cambrian Amadeus and Georgina basin sequences suggests that the metasedimentary rocks of the HRG are either derived from similar-aged but unrelated rocks, or are the highly metamorphosed correlatives of these basin successions (Buick *et al.* 2001; Buick *et al.* 2005; Maidment *et al.* 2013). Age distributions (Fig. 1) from all three successions show three dominant detrital zircon populations (Maidment *et al.* 2013): (1) ~1.90–1.70 Ga, with smaller populations extending to ~1.65–1.55 Ga and at ~2.5 Ga; (2) ~1.20–1.00 Ga; and (3) ~700–500 Ma. These populations are consistent with derivation from (1) the Palaeoproterozoic Arunta region (Collins and Shaw 1995; Scrimgeour *et al.* 2005; Claoué-Long *et al.* 2008); (2) Musgrave Inlier (Camacho *et al.* 2002; Wade *et al.* 2008); and (3) a Cambro-Ordovician Proto-Gondwanan margin origin (Williams *et al.* 2002). However, MDS analysis provides a more robust statistical comparision for visualisation of the dissimilarity between samples from the upper, mid and lower succession to better discriminate age frequency distributions (Chapman *et al.* 2012; Stevens *et al.* 2013; Vermeesch 2013). MDS analysis reflects a relatively strong similarity between samples for each of the upper, mid and lower parts of the successions (Fig. 6). Comparisons made between the entire HRG, Amadeus Basin and Georgin Basin

successions (Fig. 7) likewise reflect very strong similarities in the age spectra between the 'averaged' provenances of each succession.

The Hf-isotopic analyses from this study provide additional constraints on comparisons between proposed correlative sequences. Results show a wide range in ε_{Hf} values suggesting that the sources of the magmas in which zircons grew included both pre-existing crust (i.e. 'evolved' sources) and more juvenile sources. Determining specific heterogeneity and crustal evolution of potential source regions is beyond the scope of this study. However, the isotopic signature of units from the HRG correlates broadly with those from the basin successions for the basal, mid and upper succession (Fig. 8). The correlation in age and isotopic signature is strongest for the Arumbera Sandstone and Crossing Bore Schist of the mid succession (also Fig. 9) effectively signifying they are indeed stratigraphic correlatives. Differences between Hf-isotope compositions for samples deemed stratigraphic correlatives may be partially attributed to currently unconstrained intraformational heterogeneity, and sampling localities not being precisely equivalent within their respective sections. Observed similarities on the basis of comparative Lu-Hf zircon isotopic compositions combined with comparative modelling of detrital zircon age spectra in the HRG and the surrounding basins, nevertheless provide strong support to the notion that the HRG is a correlative of sequences in the Amadeus and Georgina basins.

5.2. Structural architecture

Within the HRG, deformation associated with peak metamorphism (D1) resulted in the development of a coarse layer-parallel fabric (S1). Tonalitic segregations containing the peak metabasic assemblages reflect fluid-absent partial melting, and both overprint and parallel S1, indicating that granulite facies conditions (~850ºC, 10 kbar) prevailed throughout D1 in the lower parts of the sequence. NE-side-down shear-sense kinematics associated with

S2 fabrics, typically preserved in domains of diatexite, imply that the subsequent development of the S2 fabric was associated with NE–SW-oriented extension. Both the S1 and S2 fabrics are paralleled and cross-cut by variably deformed mafic dykes, indicating that mafic magmatism was coeval with extensional deformation. The occurrence of extensive mafic magmatism within the HRG itself reflects extension with mantle decompression melting driven by by thinning of the continental lithosphere (e.g. Thompson and Gibson 1994; Corti *et al.* 2003). Mafic magmatism is also interleaved with metasedimentary rocks of the Irindina Gneiss, indicating that burial, basin development and metamorphism were coincident with ongoing extension.

The timing of D1 has not been directly constrained. However, Maidment *et al.* (2013) obtained a $^{206}Pb/^{238}U$ age of 483 ± 6 Ma for metamorphic zircon in peak metabasite assemblages near Mt. Ruby in the southern Harts Range. Maidment (2005) and Payne (2008) also obtained ages of 450.2 ± 3.4 Ma and 449.7 ± 3.4 Ma, respectively, from monazite in peak metapelite assemblages from the Irindina Gneiss from the location of sample IG-222 (Fig. 2). In this study, monazite included within prograde-zoned garnet and the enclosing S2 matrix fabric from the Brady Gneiss suggests a similar age of monazite growth at 442.4 ± 9.1 Ma (Fig. 15). The monazite ages are slightly younger than the zircon ages which may reflect the timing of retrograde melt crystalisation (e.g. Kelsey *et al.* 2008) post peak conditions of high-grade metamorphism during the Ordovician Larapinta Event (c. 480-460 Ma, Hand *et al.* 1999).

Local preservation of top-to-the-SW kinematics reflects basin inversion driven by convergent south-southwest directed shortening (regional D3). Pegmatites deformed by D3 fabrics dated by Buick *et al.* (2008) to ≤380 Ma indicate that D3 is associated with the ASO. This was ultimately responsible for exhumation of the HRG and adjacent Arunta basement

from mid–lower crust by c. 310 Ma (Collins and Teyssier 1989; Sandiford and Hand 1998; Haines *et al.* 2001; Sandiford *et al.* 2001).

5.3. Pressure-temperature-time evolution

Thermobarometry from coarse migmatitic peak assemblages of the HRMC and Brady Gneiss indicate peak metamorphic conditions of 887 ± 52°C and 10.5 ± 0.9 kbar, and 677 ± 34°C and 7.3 ± 1.3 kbar respectively, in the structurally lowest and highest parts of the HRG, which is consistent with previous work (Oliver *et al.* 1988; Miller *et al.* 1997; Mawby *et al.* 1999). Phase equlibria modelling (Fig. 12–14) indicates that the peak assemblages from the lower Irindina Gneiss metapelite formed within the range ~700–770ºC and 7.5–9.5 kbar. In constrast, for the Upper Brady Gneiss, the peak assemblage formed between ~660–730ºC and 5–8 kbar with electron microprobe analyses of progrde-zoned garnet further constraining inferred peak conditions to ~670ºC and 6.5 kbar. A slight discrepancy between P–T estimates from phase equilibria and those calculated using the average P–T method may reflect differences in the activity-composition models between the two methods (e.g. Powell and Holland 2008). Nonetheless, metamorphic conditions reflect that stratigraphically younger sequences in the HRG were buried to shallower depths compared to older successions and further suggest that the entire HRG has remained stratigraphically right-way-up.

Mineral contours in psuedosections reflect increasing garnet abundance and stability throughout the entire prograde P–T evolution in agreement with the preservation of prograde compositional zoning (Spear 1993). Textural and field relationships in both the Brady Gneiss and Irindina Gneiss metapelites (Fig. 4 & 10) show andalusite pseudomorphed by sillimanite, and garnet porphyroclasts wrapped in a foliation defined by biotite–muscovite ± sillimanite suggesting that they formed part of an assemblage which involved the prograde development of andalusite, then sillimanite. The absence of kyanite pseudomorphs or inclusions of

cordierite in garnet suggests that the prograde path tracked close between the kyanite and cordierite stability fields (Fig. 13 & 14). This reflects increasing pressure and temperature conditions along a moderately-high geotherm (low P/T) as opposed to a low geotherm (high P/T) that is typically associated with crustal thickening (Spear and Peacock 1989; Spear 1993; Sandiford *et al.* 1998). This prograde regime is accordingly more suited to that associated with extension.

5.4. Implications for mechanisms of burial to mid–lower crustal depths

In the absence of a palaeogeographic context, high-grade metamorphic terranes recording P–T conditions comparable to those of the HRG, are often ascribed to deep burial (~20–30 km) by crustal thickening during compressional orogenesis (e.g. Brown 1993, Jaimieson et al 2002). However, burial of HRG protoliths is constrained to have occurred along a near-linear high-geotherm that passed through andalusite stability, which is typically more indicative of an extensional regime (e.g. Spear & Peacock 1989). Metamorphic conditions also reflect that stratigraphically younger sequences were buried to shallower depths and lower metamorphic grades than older sequences. Peak metamorphism linked with coarse stratigraphy-parallel fabrics, immediately post-peak extensional kinematics, and voluminous, syn-depositional and syn-deformational mafic magmatism also support an extensional tectonic regime. Furthermore, statistical analysis shows the overall provenance of HRG zircons is virtually identical to the surrounding basins, and individual units are highly correlated between the two regions. Palaeogeographic reconstructions indicate burial and localised high-grade regional lower-crustal deformation of HRG protoliths was concurrent with the Larapintine Seaway, and the persistently shallow, epicontinental marine environment associated with ongoing Centralian Superbasin sedimentation (Shaw *et al.* 1991; Sandiford and Hand 1998; Haines *et al.* 2001; Lindsay 2002).

It is difficult to reconcile these observations with traditional mechanisms of deep burial from underthrusting or compressional over-thickening, which typically result in more extensive metamorphic terranes, often with stratigraphic inversion, and initially low geothermal gradients (Robinson and Bevins 1989; Harley 1992; Brown 1993; Brown 2001; Jamieson et al. 2002). Accordingly, the HRG evolution seems more consistent with burial by sediment loading with high-grade burial metamorphism localised within a super-deep rift basin, within a broader intraplate basin system. If burial did occur within an extensional intraplate setting, then burial, basin development and metamorphism were likely coeval with ongoing extension. High-grade metamorphism was probabily facilitated by elevated lower-crustal heat flow and magmatism associated with rifting.

The notion that burial into the lower crust can occur within sedimentary basins is supported by the preservation of a number of well-recognised basins worldwide that have >20 km of sedimentary fill (e.g. Allen *et al.* 1995; Starostenko *et al.* 1999; Baldwin *et al.* 2003). Proximity and trend approximately normal to the Cambro-Ordovician Australian continental margin, the discrete and broadly V-shaped distribution of the HRG, narrowing to the west and opening to the east (Maidment *et al.* 2013), and preservation of a half-graben style geometry of the HRG as reflected by seismic data in sectional view (Korsch *et al.* 2011) is also consistent with characteristics common to most ultra-deep sedimentary basins.

If this model is correct there are significant implications for the way in which high-grade metamorphic terranes are interpreted when palaeogeographic constraints are lacking. Burial and subsequent metamorphism of the HRG to mid-lower crustal depths indicates that regional-scale medium to high pressure metamorphism can occur in deep intraplate rift basins during extension, and accordingly that high-grade metamorphism of supracrustal rocks is not necessarily reflective of compressional crustal thickening.

6. CONCLUSIONS

Similarities in the detrital zircon age spectra and Hf-isotopic signature between the high-grade metasedimentary rocks of the HRG and the unmetamorphosed late Neoproterozoic-Cambrian Amadeus and Georgina basin sequences imply that the HRG is a highly metamorphosed equivalent to the Centralian Superbasin successions. Integrated phase equilibria modelling and thermobarometry reflect peak metamorphic conditions of ~880ºC and 10.5 kbar, and ~670ºC and 7.0 kbar in the structurally lowest and highest parts of the HRG, respectively. This implies burial of the lower parts of the succession to mid-lower crustal depths (~25–30 km). In contrast, stratigraphically younger sequences were buried to shallower depths and experienced lower metamorphic grades compared to older successions. Burial occurred along a high geothermal gradient evidenced by the development of prograde andalusite-bearing mineral assemblages. Peak metamorphism was also associated with a coarse layer-parallel fabric, subsequent NE-side-down extensional deformation, and abundant mafic magmatism, the combination of which points to an extensional tectonic regime. Late Ordovician U–Pb ages of monazite growth are interpreted to record the timing of high-grade retrograde metamorphism of the upper HRG following peak metamorphic conditions during the Larapinta Event (c. 480–460 Ma). The HRG seems consistent with profound sediment loading and high-grade metamorphism occurring within a localised super-deep intraplate rift basin. Deep burial of the HRG therefore indicates that regional medium-pressure, high-grade metamorphic terranes may be generated in ultra-deep sedimentary basins and are not necessarily reflective of compressional thickening. The tectonic interpretation of deeply-buried supracrustal successions as compressional in the absence of a palaeogeographic context should therefore be done so with caution.

ACKNOWLEDGMENTS

Supervisors Martin Hand and Justin Payne are thanked for their invaluable and onging support, guidance and encouragement. David Maidment and Ian Williams are thanked for providing zircon samples from the Harts Range, and Amadeus and Georgina basins for additional analysis in this study. Richard Taylor and Chris Clark, Curtin University, are thanked for assistance with SHRIMP analyses. Ben Wade and Angus Netting, Adelaide Microscopy, are thanked for their assistance with SEM imaging, and electron microprobe and LA-ICP-MS analyses.

REFERENCES

ALLEN D. J., BRAILE L. W., HINZE W. J. & MARIANO J. 1995. The Midcontinent rift system, U.S.A.: a major Proterozoic continental rift. *In:* Olsen K. H. ed. *Continental rifts: evolution, structure, tectonics, geotectonics,* pp. 373–407, Elsevier, Netherlands.

BALDWIN S., WHITE N. & MULLER R. 2003. Resolving multiple rift phases by strain-rate inversion in the Petrel Sub-basin, northwest Australia. In Hillis R. & Muller R. D. eds. *Evolution and dynamics of the Australian Plate* pp. 245–263. *Geological Society of Australia Special Publication* 22 and *Geological Society of America Special Paper* **372**.

BARNES L. 2013. Structural evolution of the northern Harts Range, central Australia. Honours Thesis, Curtin University of Technology, Perth.

BLACK L. P., KAMO S. L., ALLEN C. M., DAVIS D. W., ALEINIKOFF J. N., VALLEY J. W., MUNDIL R., CAMPBELL I. H., KORSCH R. J., WILLIAMS I. S. & FOUDOULIS C. 2004. Improved $^{206}Pb/^{238}U$ microprobe geochronology by the monitoring of a trace-element-related matrix effect; SHRIMP, ID–TIMS, ELA–ICP–MS and oxygen isotope documentation for a series of zircon standards. *Chemical Geology* **205**, 115–140.

BOUVIER A., VERVOORT J. D. & PATCHETT P. J. 2008. The Lu–Hf and Sm–Nd isotopic composition of CHUR: constraints from unequilibrated chondrites and implications for the bulk composition of terrestrial planets. *Earth and Planetary Science Letters* **273**, 48–57.

BROWN M. 1993. P-T-t evolution of orogenic belts and the causes of regional metamorphism. *Journal of the Geological Society, London* **150**, 227–241.

BROWN M. 2001. From microscope to mountain belt: 150 years of petrology and its contribution to understanding geodynamics, particularly the tectonics of orogens. *Journal of Geodynamics* **32**, 115–164.

BUICK I. S., HAND M., WILLIAMS I. S., MAWBY J., MILLER J. A. & NICOLL R. S. 2005. Detrital zircon provenance constraints on the evolution of the Harts Range Metamorphic Complex (central Australia): links to the Centralian Superbasin. *Journal of the Geological Society, London* **162**, 777–787.

BUICK I. S., MILLER J. A., WILLIAMS I. S. & CARTWRIGHT I. 2001. Ordovician high-grade metamorphism of a newly recognised late Neoproterozoic terrane in the northern Harts Range, central Australia. *Journal of Metamorphic Geology* **19**, 373–394.

BUICK I. S., STORKEY A. & WILLIAMS I. S. 2008. Timing relationships between pegmatite emplacement, metamorphism and deformation during the intra-plate Alice Springs Orogeny, central Australia. *Journal of Metamorphic Geology* **26**, 915–936.

BUSBY C. & INGERSOLL R. 1995. *Teconics of sedimentary basins.* Blackwell Science Inc., U.S.A.

CAMACHO A., HENSEN B. J. & ARMSTRONG R. 2002. Isotopic test of a thermally driven intraplate orogenic model, Australia. *Geology* **30**, 887–890.

CHAPMAN A. D., SALEEBY J. B., WOOD D. J., PIASECKI A., KIDDER S., DUCEA M. N. & FARLEY K. A. 2012. Late Cretaceous gravitational collapse of the southern Sierra Nevada batholith, California. *Geosphere* **8**, 314–341.

CLAOUÉ-LONG J., COMPSTON W., ROBERTS J. & FANNING C. 1995. Two Carboniferous ages: a comparison of SHRIMP zircon dating with conventional zircon ages and $^{40}Ar/^{39}Ar$ analysis. In Bergrenn W., Kent D., Aubry M. & Hardenbol J. eds. *Geochronology, time scales and global stratigraphic correlation* pp. 1–21. *SEPM Special Publication* **54**.

CLAOUÉ-LONG J., MAIDMENT D., HUSSEY K. & HUSTON D. 2008. The duration of the Strangways Event in central Australia: evidence for prolonged deep crust processes. *Precambrian Research* **166**, 246–262.

CLARKE G. L., KLEPEIS K. A. & DACZKO N. R. 2000. Cretaceous high-P granulites at Milford Sound, New Zealand: metamorphic history and emplacement in a convergent margin setting. *Journal of Metamorphic Geology* **18**, 359–374.

COGGON R. & HOLLAND T. 2002. Mixing properties of phengitic micas and revised garnet-phengite thermobarometers. *Journal of Metamorphic Geology* **20**, 683-696.

COLLINS W. J. & SHAW R. D. 1995. Geochronological constraints on orogenic events in the Arunta Inlier: a review. *Precambrian Research* **71**, 315–346.

COLLINS W. J. & TEYSSIER C. 1989. Crustal scale ductile fault systems in the Arunta Inlier, central Australia. *Tectonophysics* **158**, 49–66.

COMPSTON W., WILLIAMS I. S. & MEYER C. 1984. U-Pb geochronology of zircons from lunar breccia 73217 using a sensitive high mass-resolution ion microprobe. *Journal of Geophysical Research: Solid Earth* **89**, 525–534.

COOPER J. A., MORTIMER G. E. & JAMES P. R. 1988. Rate of Arunta Inlier evolution at the eastern margin of the Entia Dome, central Australia. *Precambrian Research* **40–41**, 217–231.

CORTI G., BONINI M., CONTICELLI S., INNOCENTI F., MANETTI P. & SOKOUTIS D. 2003. Analogue modelling of continental extension: a review focused on the relations between the patterns of deformation and the presence of magma. *Earth-Science Reviews* **63**, 169–247.

DE LAETER J. R. & KENNEDY A. K. 1998. A double focusing mass spectrometer for geochronology. *International Journal of Mass Spectrometry* **178**, 43–50.

FLOTTMANN T. & HAND M. 1999. Folded basement-cored tectonic wedges along the northern edge of the Amadeus Basin, central Australia: evaluation of orogenic shortening. *Journal of Structural Geology* **21**, 399–412.

FRIEDMANN S. & BURBANK D. 1995. Rift basins and supradetachment basins: intracontinental extensional end-members. *Basin Research* **7**, 109–127.

GRIFFIN W. L., BELOUSOVA E. A., SHEE S. R., PEARSON N. J. & O'REILLY S. Y. 2004. Archean crustal evolution in the northern Yilgarn Craton: U–Pb and Hf-isotope evidence from detrital zircons. *Precambrian Research* **131**, 231–282.

GRIFFIN W. L., WANG X., JACKSON S. E., PEARSON N. J., O'REILLY S. Y., XU X. & ZHOU X. 2002. Zircon chemistry and magma mixing, SE China: In-situ analysis of Hf isotopes, Tonglu and Pingtan igneous complexes. *Lithos* **61**, 237–269.

HAINES P. & WINGATE M. Year. Contrasting depositional histories, detrital zircon provenance and hydrocarbon systems: did the Larapintine Seaway link the Canning and Amadeus basins during the Ordovician? In Munson T. J. & Ambrose G. J. eds. *Proceedings of the Central Australian Basins Symplosium (CABS),* Alice Springs, Northern Territory, 16-18 August 2005, pp. 36–51. *Northern Territory Geological Survey Special Publication* **2**.

HAINES P. W., HAND M. & SANDIFORD M. 2001. Palaeozoic synorogenic sedimentation in central and northern Australia: a review of distribution and timing with implications for the evolution of intracontinental orogens. *Australian Journal of Earth Sciences* **48**, 911–928.

HAND M., MAWBY J., KINNY P. & FODEN J. D. 1999. U–Pb ages from the Harts Range, central Australia: evidence for early Ordovician extension and constraints on Carboniferous metamorphism. *Journal of the Geological Society, London* **156**, 715–730.

HOLLAND T. & POWELL R. 1998. An internally consistent thermodynamic data set for phases of petrological interest. *Journal of metamorphic Geology* **16**, 309–343.

HOLLAND T. & POWELL R. 2003. Activity-composition relations for phases in petrological calculations: an asymmetric multicomponent formulation. *Contributions to Mineralogy and Petrography* **145**, 492–501.

HOLLIS J. A., BEYER E. E., WHELAN J., KEMP A., SCHERSTEN A. & GREIG A. 2010. Summary of results. NTGS laser U–Pb and Hf geochronology project: Pine Creek Orogen, Murphy Inlier, McArthur Basin and Arunta region, July 2007–June 2008. *Northern Territory Geological Survey, Record* 2010-001.

JAMIESON R. A., BEAUMONT C., NGUYEN M. H. & LEE B. 2002. Interaction of metamorphism, deformation and exhumation in large convergent orogens. *Journal of Metamorphic Geology* **20**, 9–24.

JOLIVET M., ARZHANNIKOV S., CHAUVET A., ARZHANNIKOVA A., VASSALLO R., KULAGINA N. & AKULOVA V. 2012. Accommodating large-scale intracontinental extension and compression in a single stress-field: a key example from the Baikal Rift System. *Gondwana Research* **24**, 918–935.

KELSEY D. E., CLARK C. & HAND M. 2008. Thermobarometric modelling of zircon and monazite growth in melt-bearing systems: examples using model metapelitic and metapsammitic granulites. *Journal of Metamorphic Geology* **26**, 199–212.

KORSCH R. J., BLEWETT R. S., CLOSE D. F., SCRIMGEOUR I. R., HUSTON D. L., KOSITCIN N., WHELAN J. A., CARR L. K. & DUAN J. M. 2011. Geological interpretation and geodynamic implications of the deep seismic reflection and magnetotelluric line 09GA-GA1: Georgina Basin–Arunta region. pp. 67–76. *Northern Territory Geological Survey Record* **3**.

KORSCH R. J. & LINDSAY J. F. 1989. Relationships between deformation and basin evolution in the intracratonic Amadeus Basin, central Australia. *Tectonophysics* **158**, 5–22.

LAMB W. M. & VALLEY J. W. 1988. Granulite facies amphibole and biotite equilibria, and calculated peak-metamorphic water activities. *Contributions to Mineralogy and Petrology* **100**, 349–360.

LINDSAY J. F. 2002. Supersequences, superbasins, supercontinents – evidence from the Neoproterozoic–early Palaeozoic basins of central Australia. *Basin Research* **14**, 207–223.

LUDWIG K. R. 2009. SQUID 2: a user's manual. *Berkeley Geochronology Centre Special Publication* **5**.

LUDWIG K. R. 2012. User's manual for ISOPLOT 3.75, a geochronological toolkit for Microsoft Excel. *Berkeley Geochronology Centre Special Publication* **5**.

MAHAR E. M., BAKER J. M., POWELL R., HOLLAND T. & HOWELL N. 1997. The effect of Mn on mineral stability in metapelites. *Journal of Metamorphic Geology* **15**, 223–238.

MAIDMENT D. W. 2005. Palaeozoic high-grade metamorphism within the Centralian Superbasin, Harts Range region, central Australia. PhD Thesis, Australian National University, Canberra.

MAIDMENT D. W., HAND M. & WILLIAMS I. S. 2005. Tectonic cycles in the Strangways Metamorphic Complex, Arunta Inlier, central Australia: geochronological evidence for exhumation and basin formaiton between two high-grade metamorphic events. *Australian Journal of Earth Sciences* **52**, 205–215.

MAIDMENT D. W., HAND M. & WILLIAMS I. S. 2013. High grade metamorphism of sedimentary rocks during Palaeozoic rift basin formation in central Australia. *Gondwana Research* **24**, 865–885.

MAIDMENT D. W., WILLIAMS I. S. & HAND M. 2007. Testing long-term patterns of basin sedimentation by detrital zircon geochronology, Centralian Superbasin, Australia. *Basin Research* **19**, 335–360.

MAWBY J., HAND M. & FODEN J. 1999. Sm–Nd evidence for high-grade Ordovician metamorphism in the Arunta block, central Australia. *Journal of Metamorphic Geology* **17**, 653–668.

MILLER J. A., CARTWRIGHT I. & BUICK I. S. 1997. Granulite facies metamorphism in the Mallee Bore area, northern Harts Range: implications for the thermal evolution of the eastern Arunta Inlier, central Australia. *Journal of Metamorphic Geology* **15**, 613–629.

MORRISSEY L., PAYNE J. L., KELSEY D. E. & HAND M. 2011. Grenvillian-aged reworking in the North Australian Craton, central Australia: constraints from geochronology and modelled phase equilibria. *Precambrian Research* **191**, 141–165.

OLIVER R. L., LAWRENCE R. W., GOSCOMBE B. D., DING P., SIVELL W. J. & BOWYER D. G. 1988. Metamorphism and crustal considerations in the Harts Range and neighbouring regions, Arunta Inlier, central Australia. *Precambrian Research* **40**, 277–295.

PAYNE J. L. 2008. Palaeo- to Mesoproterozoic evolution of the Gawler Craton, Australia: gechronological, geochemical and isotopic constraints. PhD Thesis, University of Adelaide, Adelaide.

PAYNE J. L., HAND M., BAROVICH K. M. & WADE B. P. 2008. Temporal constraints on the timing of high-grade metamorphism in the northern Gawler Craton: implications for assembly of the Australian Proterozoic. *Australian Journal of Earth Sciences* **55**, 623–640.

PAYNE J. L., PEARSON N., GRANT K. J. & HALVERSON G. P. 2013. Reassessment of relative oxide formaiton rates and molecular interferences on in-situ Lutetium-Hafnium analysis with Laser Ablation MC-ICP-MS. *Journal of Analytical Atomic Spectrometry* **28**, 1068–1079.

PHILLIPS G. N. 1980. Water activity changes across an amphibolite-granulite facies transition, Broken Hill, Australia. *Contributions to Mineralogy and Petrology* **75**, 377–386.

POWELL R. & HOLLAND T. 1988. An internally consistent thermodynamic dataset with uncertainties and correlations: 3. Application methods, worked examples and a computer program. *Journal of Metamorphic Geology* **6**, 173–204.

POWELL R. & HOLLAND T. 1994. Optimal geothermometry and geobarometry. *American Mineralogist* **79**, 120–133.

POWELL R. & HOLLAND T. 2008. On thermobarometry. *Journal of Metamorphic Geology* **26**, 155–179.

POWELL R., HOLLAND T. & WORLEY B. 1998. Calculating phase diagrams involving solid solutions via non-linear equations, with examples using THERMOCALC. *Journal of Metamorphic Geology* **16**, 577–588.

PUZYREV N. N., MANDELBAUM M. M., KRYLOV S. V., MISHENKIN B. P., PETRIK G. V. & KRUPSKAYA G. V. 1978. Deep structure of the baikal and other continental rift zones from seismic data. *Tectonophysics* **45**, 15–22.

RAIMONDO T., CLARK C., HAND M. & FAURE K. 2011. Assessing the geochemical and tectonic impacts of fluid-rock interation in mid-crustal shear zones: a case study from the intracontinental Alice Springs Orogen, central Australia. *Journal of metamorphic geology* **29**, 821–850.

ROBINSON D. & BEVINS R. E. 1989. Diastathermal (extensional) metamorphism at very low grades and possible high grade analogues. *Earth and Planetary Science Letters* **92**, 81–88.

RUPPEL C. 1995. Extensional processes in continental lithosphere. *Journal of Geophysical Research: Solid Earth* **100**, 24187–24215.

SANDIFORD M. & HAND M. 1998. Controls on the locus of intraplate deformation in central Australia. *Earth and Planetary Science Letters* **162**, 97–110.

SANDIFORD M., HAND M. & MCLAREN S. 1998. High geothermal gradient metamorphism during thermal subsidence. *Earth and Planetary Science Letters* **163**, 149–165.

SANDIFORD M., HAND M. & MCLAREN S. 2001. Tectonic feedback, intraplate orogeny and the geochemical structure of the crust: a central Australian perspective. In Miller J. A., Holdsworth R. E., Buick I. S. & Hand M. eds. *Continental reactivation and reworking* pp. 195-218. *Geological Society of London Special Publication* **184**.

SANDIFORD M. & POWELL R. 1986. Deep crustal metamorphism during continental extension: modern and ancient examples. *Earth and Planetary Science Letters* **79**, 151–158.

SCHERER E., MÜNKER C. & MEZGER K. 2001. Calibration of the Lutetium-Hafnium Clock. *Science* **293**, 683-687.

SCRIMGEOUR I. & RAITH J. G. 2001. High-grade reworking of Proterozoic granulites during Ordovician intraplate transpression, eastern Arunta Inlier, Central Australia. **184**, 261–287.

SCRIMGEOUR I. R., KINNY P. D., CLOSE D. F. & EDGOOSE C. J. 2005. High-T granulites and polymetamorphism in the southern Arunta region, central Australia: evidence for a 1.64 Ga accretional event. *Precambrian Research* **142**, 1–27.

SEGAL I., HALICZ L. & PLATZNER I. T. 2003. Accurate isotope ratio measurements of ytterbium by multiple collection inductively coupled plasma mass spectrometry applying erbium and hafnium in an improved double external normalization procedure. *Journal of Analytical Atomic Spectrometry* **18**, 1217–1223.

SHAW R. D., ETHERIDGE M. A. & LAMBECK K. 1991. Development of the late Proterozoic to mid-Paleozoic, intracratonic Amadeus Basin in central Australia: a key to understanding tectonic forces in plate interiors. *Tectonics* **10**, 688–721.

SIVELL W. J. 1988. Geochemistry of metatholeiites from the Harts Range, central Australia: implications for mantle source heterogeneity in a Proterozoic mobile belt. *Precambrian Research* **40**, 261–275.

SIVELL W. J. & FODEN J. D. 1985. Banded amphibolites of the Harts Range meta-igneous complex, central Australia: an early Proterozoic basalt-tonalite suite. *Precambrian Research* **28**, 223–252.

SLAMA J., KOSLER J., CONDON D. J., CROWLEY J. L., GERDES A., HANCHAR J. M., HORSTWOOD M. S. A., MORRIS G. A., NASDALA L., NORBERG N., SCHALTEGGER U., SCHOENE N., TUBRETT M. N. & WHITEHOUSE M. J. 2008. Plesovice zircon - a new natural reference material for U–Pb and Hf isotopic microanalysis. *Chemical Geology* **249**, 1–35.

SPEAR F. S. 1993. *Metamorphic phase equilibria and pressure-temperature-time paths.* BookCrafters, Inc., Michigan, U.S.A.

SPEAR F. S. & PEACOCK S. M. 1989. *Metamorphic pressure-temperature-time paths.* American Geophysical Union, Washington, USA.

STAROSTENKO V. I., DANILENKO V. A., VENGROVITCH D. B., KUTAS R. I., STOVBA S. M., STEPHENSON R. A. & KHARITONOV O. M. 1999. A new geodynamical–thermal model of rift evolution, with application to the Dnieper–Donets Basin, Ukraine. *Tectonophysics* **313**, 29–40.

STEVENS T., CARTER A., WATSON T. P., VERMEESCH P., ANDÒ S., BIRD A. F., LU H., GARZANTI E., COTTAM M. A. & SEVASTJANOVA I. 2013. Genetic linkage between the Yellow River, the Mu Us desert and the Chinese Loess Plateau. *Quaternary Science Reviews* **78**, 355–368.

TAM P. Y., ZHAO G., SUN M., LI S., IIZUKA Y., MA G. S.-K. I., YIN C., HE Y. & WU M. 2012. Metamorphic P–T path and tectonic implications of medium-pressure pelitic granulites from the Jiaobei Massif in the Jiao-Liao-Ji Belt, North China Craton. *Precambrian Research* **220–221**, 177–191.

THOMPSON R. N. & GIBSON S. A. 1994. Magmatic expression of lithospheric thinning across continental rifts. *Tectonophysics* **233**, 41–68.

VANCE D., STRACHAN R. A. & JONES K. A. 1998. Extensional versus compressional settings for metamorphism: garnet chronometry and pressure-temperature-time histories in the Moine Supergroup, northwest Scotland. *Geology* **26**, 927–930.

VERMEESCH P. 2013. Multi-sample comparison of detrital age distributions. *Chemical Geology* **341**, 140–146.

VERVOORT J. D., PATCHETT P. J., SÖDERLUND U. & BAKER M. 2004. Isotopic composition of Yb and the determination of Lu concentrations and Lu/Hf ratios by isotope dilution using MC-ICPMS. *Geochemistry, Geophysics, Geosystems* **5**, Q11002, doi: 10.1029/2004GC000721.

WADE B. P., KELSEY D. E., HAND M. & BAROVICH K. M. 2008. The Musgrave Province: stitching north, west and south Australia. *Precambrian Research* **166**, 370–386.

WEBBY B. D. 1978. History of the Ordovician contiental platform shelf margin of Australia. *Journal of the Geological Society of Australia* **25**, 41–63.

WHITE N., POMROY N. E. & POWELL R. 2005. An in-situ metatexite-diatexite transition in upper amphibolite facies rocks from Broken Hill, Australia. *Journal of Metamorphic Geology* **23**, 579–602.

WHITE R. W., POWELL R. & CLARKE G. L. 2002. The interpretation of reaction textures in Fe-rich metapelitic granulites of the Musgrave Block, central Australia: constraints from mineral equilibria calculation in the system K_2O-FeO-MgO-Al_2O_3-SiO_2-H_2O-TiO_2-Fe_2O_3. *Journal of Metamorphic Geology* **20**, 41–55.

WHITE R. W., POWELL R. & HOLLAND T. 2007. Progress relating to calculation of partial melting equilibria for metapelites. *Journal of Metamorphic Geology* **25**, 511–527.

WHITE R. W., POWELL R., HOLLAND T. & WORLEY B. 2000. The effect of bolite facies conditiona: mineral equilibria calculations in the system K_2O-FeO-MgO-Al_2O_3-SiO_2-H_2O-TiO_2-Fe_2O_3. *Journal of Metamorphic Geology* **18**, 497–511.

WICKHAM S. M. & OXBURGH E. R. 1985. Continental rifts as a setting for regional metamorphism. *Nature* **318**, 330–333.

WILLIAMS, I.S., GOODGE, J., MYROW, P., BURKE, K., KRAUS, J. 2002. Large scale sediment dispersal associated with the late Neoproterozoic assembly of Gondwana. *Geological Society of Australia Abstracts* **67**, 238.

WOODHEAD J., HERGT J., SHELLEY M., EGGINS S. & KEMP R. 2004. Zircon Hf-isotope analysis with an excimer laser, depth profiling, ablation of complex geometries, and concomitant age estimation. *Chemical Geology* **209**, 121–135.

WOODHEAD J. D. & HERGT J. M. 2005. A preliminary appraisal of seven natural zircon reference materials for in-situ Hf-isotope determination. *Geostandards and Geoanalytical Research* **29**, 183–195.

ZHAO J. X., MCCULLOCH M. T. & BENNETT V. C. 1992. Sm-Nd and U-Pb zircon isotopic constraints on the provenance of sediments from the Amadeus Basin, central Australia: evidence for REE fractionation. *Geochimica et Cosmochimica Acta* **56**, 921–940.

APPENDIX A: SUMMARY OF SAMPLES

Sample	Location (53K) Easting	Northing	Region	Unit	Lithology	Geochron.	Lu-Hf	Trace element	Geochem.	Pseudosection	Thermobarometry	Gt maps
						Analyses						
Whole-rock samples												
HR-NT-UBG-3	501726	7458816	Harts Range	Upper Brady Gneiss	Metapelite			x				
HR-NT-UBG-4	501726	7458816	Harts Range	Upper Brady Gneiss	Metapelite			x	x	*x*	*x*	
HR-NT-BG-03	495886	7453346	Harts Range	Brady Gneiss	Metapelite			x				
HR-NT-BG-07	496321	7454594	Harts Range	Brady Gneiss	Metapelite	x		x		*x*	*x*	
HR-NT-BG-08	496321	7454594	Harts Range	Brady Gneiss	Metapelite			x		*x*		
HR-NT-BG-09	496321	7454594	Harts Range	Brady Gneiss	Metapelite	x		x				
HR-NT-IG-02	494952	7452565	Harts Range	Irindina Gneiss	Metapelite			x			*x*	
HR-NT-IG-10	495224	7449597	Harts Range	Irindina Gneiss	Metapelite			x	x		*x*	
HR-NT-IG-222	508639	7456191	Harts Range	Irindina Gneiss	Metapelite			x	x			
HR-NT-IG-16	495203	7449447	Harts Range	HRMC	Mafic granulite					*x*		
HR-NT-IG-23	495191	7449424	Harts Range	HRMC	Mafic granulite					*x*		
HR-NT-IG-26	495091	7449338	Harts Range	HRMC	Mafic granulite					*x*		
HR-NT-IG-28	495024	7449344	Harts Range	HRMC	Mafic granulite					*x*		
Detrital zircon samples												
2002080036*	585064	7497487	Georgina Basin	Tomahawk Formation			x	x				
2002080070*	447713	7387555	Amadeus Basin	Pacoota Sandstone			x	x				
2002080073*	447419	7389689	Amadeus Basin	Arumbera Sandstone		x	x	x				
2002080308*	498968	7403777	Amadeus Basin	Heavitree Quartzite			x	x				
2001080254^	540929	7439848	Harts Range	Upper Brady Gneiss			x	x				
2001080104^	564073	7443740	Harts Range	Crossing Bore schist			x	x				
2001080196^	539728	7422671	Harts Range	Lower Stanavos Gneiss			x	x				

**obtained from Maidment et al. 2007; ^obtained from Maidment et al. 2013*

APPENDIX B: LU–HF ISOTOPIC ANALYSIS DATA TABLES

LA-MC-ICP-MS Lu-Hf Isotopic Results

Analysis	$^{176}Hf/^{177}Hf$	2 S.E.	$^{176}Lu/^{177}Hf$	$^{176}Yb/^{177}Hf$	U/Pb age (Ma)	$Hf_{initial}$	$\varepsilon Hf_{(T)}$	1σ	$T_{DM(crustal)}$ (Ga)
Standards									
Laser - Hf glass									
Hf_01	0.28215	1.1E-05	0.00000	0.0000					
Hf_02	0.28216	1.2E-05	0.00000	0.0000					
Solution - JMC 475 Hf standard solution									
JMC475_1	0.28215	7.8E-06	0.00000	0.0000					
JMC475_2	0.28216	7.9E-06	0.00000	0.0000					
JMC475_3	0.28217	7.6E-06	0.00000	0.0000					
Zircon standards - session 1									
Mudtank									
JP_MT_284ox	0.28251	1.4E-05	0.00002	0.0013	732	0.282507	6.51	0.5	1.21
JP_MT_285ox	0.28251	1.6E-05	0.00002	0.0012	732	0.282512	6.69	0.6	1.20
JP_MT_286ox	0.28252	1.6E-05	0.00002	0.0009	732	0.282517	6.86	0.6	1.19
JP_MT_287ox	0.28251	1.5E-05	0.00002	0.0008	732	0.282507	6.52	0.5	1.21
JP_MT_288ox	0.28252	1.4E-05	0.00002	0.0010	732	0.282521	7.01	0.5	1.18
JP_MT_293ox	0.28250	1.4E-05	0.00002	0.0008	732	0.282502	6.34	0.5	1.22
JP_MT_295ox	0.28250	1.2E-05	0.00002	0.0010	732	0.282499	6.22	0.4	1.23
AVERAGE ± stdev	0.28251	1.5E-05	0.00002	0.0010					
Plesovice									
JP_Ples_342ox	0.28246	1.7E-05	0.00011	0.0077	337	0.282456	-4.15	0.6	1.58
JP_Ples_343ox	0.28247	1.8E-05	0.00011	0.0079	337	0.282467	-3.77	0.6	1.55
JP_Ples_344ox	0.28248	1.6E-05	0.00013	0.0095	337	0.282474	-3.50	0.6	1.54
JP_Ples_345ox	0.28248	1.6E-05	0.00012	0.0084	337	0.282474	-3.49	0.6	1.54
JP_Ples_346ox	0.28247	1.6E-05	0.00008	0.0056	337	0.282468	-3.71	0.6	1.55
JP_PLES_346ox	0.28247	1.6E-05	0.00011	0.0073	337	0.282468	-3.74	0.6	1.55
JP_Ples_348ox	0.28248	1.5E-05	0.00009	0.0060	337	0.282477	-3.41	0.5	1.53
JP_Ples_350ox	0.28248	1.4E-05	0.00008	0.0051	337	0.282482	-3.21	0.5	1.52
JP_Ples_353ox	0.28248	1.4E-05	0.00011	0.0071	337	0.282474	-3.50	0.5	1.54
JP_Ples_354ox	0.28247	1.5E-05	0.00011	0.0073	337	0.282471	-3.63	0.5	1.54
AVERAGE ± stdev	0.28247	1.6E-05	0.00011	0.0072					
Zircon standards - session 2									
JP_Ples_380	0.28248	1.7E-05	0.00012	0.0068	337	0.282481	-3.26	0.6	1.52
JP_Ples_381	0.28246	1.5E-05	0.00011	0.0061	337	0.282461	-3.96	0.5	1.56
JP_Ples_382	0.28246	1.5E-05	0.00011	0.0058	337	0.282462	-3.92	0.5	1.56
JP_Ples_383	0.28246	1.6E-05	0.00010	0.0056	337	0.282463	-3.91	0.5	1.56
JP_Ples_384	0.28247	1.7E-05	0.00011	0.0059	337	0.282469	-3.68	0.6	1.55
JP_Ples_385	0.28246	1.6E-05	0.00011	0.0059	337	0.282461	-3.97	0.6	1.57
JP_PLES_386	0.28247	1.5E-05	0.00008	0.0044	337	0.282467	-3.76	0.5	1.55
JP_PLES_387	0.28247	2.0E-05	0.00009	0.0051	337	0.282469	-3.70	0.7	1.55
JP_Ples_388	0.28246	1.6E-05	0.00009	0.0047	337	0.282460	-4.00	0.6	1.57
AVERAGE	0.28247	1.6E-05	0.00010	0.0056					
SESSION 1									
Upper Brady Gneiss									
NT_UBG_11_1	0.28205	4.2E-05	0.00090	0.0458	1238	0.282027	0.95	1.5	1.95
NT_UBG_13_1	0.28247	4.8E-05	0.00145	0.0724	584	0.282450	1.18	1.7	1.43
NT_UBG_20_1	0.28174	3.7E-05	0.00089	0.0443	1787	0.281708	2.19	1.3	2.31
NT_UBG_21_1	0.28169	2.9E-05	0.00132	0.0607	1981	0.281638	4.18	1.0	2.34
NT_UBG_22_1	0.28129	3.4E-05	0.00125	0.0622	2523	0.281228	2.19	1.2	2.89
NT_UBG_24_1	0.28234	2.8E-05	0.00166	0.0798	670	0.282322	-1.44	1.0	1.66
NT_UBG_25_1	0.28153	2.2E-05	0.00050	0.0241	2170	0.281510	4.02	0.8	2.50
NT_UBG_26_1	0.28155	4.0E-05	0.00103	0.0564	1769	0.281517	-5.00	1.4	2.73
NT_UBG_27_1	0.28214	3.5E-05	0.00091	0.0337	1065	0.282125	0.50	1.2	1.85
NT_UBG_28_1	0.28220	4.8E-05	0.00072	0.0363	1065	0.282190	2.81	1.7	1.71
NT_UBG_29_1	0.28233	4.7E-05	0.00241	0.0855	707	0.282300	-1.37	1.7	1.69
NT_UBG_30_1	0.28196	4.3E-05	0.00082	0.0407	1566	0.281932	5.07	1.5	1.96
NT_UBG_32_1	0.28235	3.4E-05	0.00073	0.0323	693	0.282345	-0.11	1.2	1.60
NT_UBG_33_1	0.28205	2.3E-05	0.00067	0.0313	1232	0.282037	1.18	0.8	1.94
NT_UBG_34_1	0.28162	3.5E-05	0.00091	0.0495	1937	0.281592	1.51	1.2	2.47
NT_UBG_35_1	0.28194	2.9E-05	0.00057	0.0233	1585	0.281921	5.10	1.0	1.97
NT_UBG_36_1	0.28162	2.1E-05	0.00116	0.0523	1862	0.281583	-0.54	0.7	2.53
NT_UBG_37_1	0.28229	2.3E-05	0.00076	0.0372	895	0.282275	1.98	0.8	1.62
NT_UBG_39_1	0.28245	3.2E-05	0.00109	0.0528	599	0.282434	0.93	1.1	1.46
NT_UBG_41_1	0.28207	2.6E-05	0.00070	0.0386	899	0.282057	-5.65	0.9	2.10
NT_UBG_42_1	0.28232	3.7E-05	0.00057	0.0266	680	0.282313	-1.51	1.3	1.68
NT_UBG_43_1	0.28202	2.4E-05	0.00054	0.0233	1189	0.282008	-0.85	0.8	2.03
NT_UBG_45_1	0.28187	2.4E-05	0.00095	0.0490	1043	0.281850	-9.75	0.8	2.46
NT_UBG_46_1	0.28237	3.5E-05	0.00263	0.1504	980	0.282322	5.55	1.2	1.47
NT_UBG_48_1	0.28179	3.2E-05	0.00135	0.0682	1665	0.281746	0.75	1.1	2.30
NT_UBG_51_1	0.28173	4.8E-05	0.00050	0.0241	1861	0.281712	4.05	1.7	2.25
NT_UBG_52_1	0.28144	4.6E-05	0.00122	0.0549	1837	0.281397	-7.72	1.6	2.94

LA-MC-ICP-MS Lu-Hf Isotopic Results

Analysis	$^{176}Hf/^{177}Hf$	2 S.E.	$^{176}Lu/^{177}Hf$	$^{176}Yb/^{177}Hf$	U/Pb age (Ma)	$Hf_{initial}$	$\varepsilon Hf_{(T)}$	1σ	$T_{DM(crustal)}$ (Ga)
NT_UBG_53_1	0.28227	4.5E-05	0.00224	0.1229	853	0.282230	-0.56	1.6	1.75
NT_UBG_54_1	0.28246	3.1E-05	0.00092	0.0454	651	0.282450	2.69	1.1	1.39
NT_UBG_55_1	0.28216	4.3E-05	0.00063	0.0264	683	0.282148	-7.31	1.5	2.04
NT_UBG_56_1	0.28227	1.9E-05	0.00036	0.0124	589	0.282267	-5.19	0.7	1.83
NT_UBG_57_1	0.28215	3.0E-05	0.00045	0.0176	583	0.282140	-9.83	1.0	2.12
NT_UBG_6_1	0.28158	3.1E-05	0.00060	0.0283	2169	0.281553	5.52	1.1	2.41
NT_UBG_7_1	0.28240	3.7E-05	0.00098	0.0505	535	0.282391	-2.01	1.3	1.59
Crossing Bore Schist									
NT_CBS_1_1	0.28212	1.9E-05	0.00067	0.0288	1207	0.282105	3.02	0.7	1.80
NT_CBS_10_1	0.28197	1.9E-05	0.00106	0.0479	1528	0.281938	4.40	0.7	1.97
NT_CBS_12_1	0.28114	1.8E-05	0.00054	0.0225	2736	0.281112	3.05	0.6	3.01
NT_CBS_13_1	0.28236	2.8E-05	0.00120	0.0601	634	0.282344	-1.47	1.0	1.64
NT_CBS_14_1	0.28203	1.8E-05	0.00053	0.0245	1184	0.282017	-0.63	0.6	2.01
NT_CBS_17_1	0.28213	2.9E-05	0.00076	0.0308	1111	0.282116	1.22	1.0	1.84
NT_CBS_18_1	0.28163	2.5E-05	0.00127	0.0594	1707	0.281593	-3.73	0.9	2.60
NT_CBS_19_1	0.28209	2.2E-05	0.00097	0.0468	1160	0.282069	0.66	0.8	1.91
NT_CBS_21_1	0.28212	2.7E-05	0.00129	0.0614	1151	0.282097	1.45	1.0	1.86
NT_CBS_22_1	0.28212	1.8E-05	0.00090	0.0426	1152	0.282101	1.61	0.6	1.85
NT_CBS_24_1	0.28206	2.0E-05	0.00071	0.0356	1154	0.282041	-0.45	0.7	1.98
NT_CBS_25_1	0.28211	1.8E-05	0.00047	0.0204	1219	0.282094	2.91	0.6	1.82
NT_CBS_29_1	0.28210	2.2E-05	0.00070	0.0308	1213	0.282087	2.51	0.8	1.84
NT_CBS_3_1	0.28208	2.1E-05	0.00059	0.0271	1141	0.282072	0.35	0.7	1.92
NT_CBS_31_1	0.28211	2.4E-05	0.00084	0.0404	1252	0.282089	3.48	0.8	1.81
NT_CBS_32_1	0.28207	3.3E-05	0.00116	0.0545	1263	0.282046	2.20	1.2	1.90
NT_CBS_34_1	0.28213	2.0E-05	0.00070	0.0326	1163	0.282114	2.31	0.7	1.81
NT_CBS_35_1	0.28210	4.8E-05	0.00171	0.0952	1060	0.282063	-1.80	1.7	1.99
NT_CBS_36_1	0.28201	1.9E-05	0.00070	0.0326	1636	0.281989	8.70	0.7	1.79
NT_CBS_37_1	0.28214	1.9E-05	0.00099	0.0463	1125	0.282116	1.53	0.7	1.83
NT_CBS_38_1	0.28085	1.7E-05	0.00060	0.0281	2686	0.280816	-8.64	0.6	3.65
NT_CBS_39_1	0.28208	2.0E-05	0.00069	0.0310	1211	0.282068	1.78	0.7	1.88
NT_CBS_41_1	0.28214	2.1E-05	0.00060	0.0267	1099	0.282129	1.40	0.7	1.82
NT_CBS_43_1	0.28209	2.1E-05	0.00058	0.0272	1212	0.282075	2.07	0.7	1.87
NT_CBS_44_1	0.28206	1.9E-05	0.00070	0.0323	1103	0.282048	-1.38	0.7	1.99
NT_CBS_46_1	0.28157	2.8E-05	0.00116	0.0517	1763	0.281530	-4.68	1.0	2.70
NT_CBS_47_1	0.28213	2.8E-05	0.00116	0.0448	1077	0.282110	0.25	1.0	1.87
NT_CBS_48_1	0.28205	2.3E-05	0.00102	0.0468	1504	0.282026	6.98	0.8	1.79
NT_CBS_49_1	0.28211	1.8E-05	0.00062	0.0281	1159	0.282094	1.55	0.6	1.86
NT_CBS_5_1	0.28211	2.4E-05	0.00135	0.0647	1209	0.282078	2.11	0.8	1.86
NT_CBS_51_1	0.28212	1.6E-05	0.00095	0.0446	1130	0.282105	1.25	0.5	1.85
NT_CBS_54_1	0.28209	1.9E-05	0.00057	0.0251	1179	0.282074	1.29	0.7	1.89
NT_CBS_55_1	0.28210	2.0E-05	0.00074	0.0330	1185	0.282085	1.82	0.7	1.86
NT_CBS_56_1	0.28190	2.3E-05	0.00143	0.0687	1433	0.281863	-0.43	0.8	2.19
NT_CBS_57_1	0.28212	2.3E-05	0.00086	0.0416	1084	0.282101	0.08	0.8	1.89
NT_CBS_58_1	0.28210	1.9E-05	0.00066	0.0300	1129	0.282085	0.52	0.7	1.90
NT_CBS_59_1	0.28211	1.6E-05	0.00049	0.0198	1169	0.282100	1.97	0.6	1.84
NT_CBS_61_1	0.28225	2.7E-05	0.00123	0.0554	1119	0.282228	5.37	0.9	1.59
NT_CBS_62_1	0.28214	2.8E-05	0.00085	0.0411	1095	0.282119	0.96	1.0	1.84
NT_CBS_63_1	0.28213	2.1E-05	0.00104	0.0473	1181	0.282108	2.53	0.8	1.81
NT_CBS_65_1	0.28213	2.1E-05	0.00104	0.0474	724	0.282117	-7.49	0.7	2.08
NT_CBS_66_1	0.28199	2.6E-05	0.00111	0.0510	1162	0.281966	-2.95	0.9	2.14
NT_CBS_8_1	0.28123	2.4E-05	0.00021	0.0098	2037	0.281217	-9.47	0.8	3.20
Pacoota Sandstone									
NT_P_10_1	0.28219	1.5E-05	0.00009	0.0048	553	0.282193	-8.61	0.5	2.02
NT_P_11_1	0.28218	2.7E-05	0.00071	0.0358	1183	0.282163	4.51	0.9	1.69
NT_P_12_1	0.28086	3.2E-05	0.00108	0.0535	3345	0.280795	6.18	1.1	3.31
NT_P_13_1	0.28230	1.9E-05	0.00042	0.0223	588	0.282294	-4.27	0.7	1.78
NT_P_14_1	0.28254	2.6E-05	0.00045	0.0208	556	0.282531	3.39	0.9	1.27
NT_P_18_1	0.28100	3.1E-05	0.00096	0.0482	2712	0.280948	-3.34	1.1	3.36
NT_P_22_1	0.28134	2.3E-05	0.00053	0.0259	2000	0.281315	-6.85	0.8	3.02
NT_P_23_1	0.28068	2.6E-05	0.00081	0.0384	3279	0.280625	-1.46	0.9	3.70
NT_P_24_1	0.28144	3.2E-05	0.00025	0.0139	584	0.281434	-34.82	1.1	3.64
NT_P_25_1	0.28072	3.7E-05	0.00172	0.0796	3325	0.280610	-0.91	1.3	3.71
NT_P_28_1	0.28204	3.0E-05	0.00096	0.0473	1482	0.282009	5.88	1.0	1.84
NT_P_31_1	0.28251	3.2E-05	0.00092	0.0409	1064	0.282494	13.55	1.1	1.04
NT_P_34_1	0.28114	3.6E-05	0.00104	0.0511	2584	0.281085	-1.48	1.3	3.15
NT_P_35_1	0.28212	3.4E-05	0.00038	0.0195	1154	0.282113	2.09	1.2	1.82
NT_P_38_1	0.28068	2.0E-05	0.00031	0.0141	3240	0.280666	-0.95	0.7	3.64
NT_P_39_1	0.28177	2.7E-05	0.00053	0.0248	1491	0.281758	-2.84	0.9	2.38
NT_P_40_1	0.28208	2.9E-05	0.00061	0.0318	1376	0.282066	5.48	1.0	1.78
NT_P_42_1	0.28128	2.7E-05	0.00073	0.0364	2169	0.281252	-5.20	1.0	3.05
NT_P_44_1	0.28244	2.9E-05	0.00062	0.0324	834	0.282426	5.95	1.0	1.33
NT_P_46_1	0.28210	2.9E-05	0.00064	0.0312	1137	0.282089	0.87	1.0	1.88
NT_P_48_1	0.28098	3.1E-05	0.00091	0.0418	2727	0.280932	-3.57	1.1	3.39
NT_P_49_1	0.28207	2.5E-05	0.00081	0.0385	1194	0.282049	0.73	0.9	1.93

LA-MC-ICP-MS Lu-Hf Isotopic Results

Analysis	$^{176}Hf/^{177}Hf$	2 S.E.	$^{176}Lu/^{177}Hf$	$^{176}Yb/^{177}Hf$	U/Pb age (Ma)	$Hf_{initial}$	$\varepsilon Hf_{(T)}$	1σ	$T_{DM(crustal)}$ (Ga)
NT_P_51_1	0.28228	2.8E-05	0.00115	0.0680	906	0.282261	1.71	1.0	1.65
NT_P_52_1	0.28212	3.1E-05	0.00147	0.0810	1201	0.282087	2.25	1.1	1.85
NT_P_53_1	0.28239	2.6E-05	0.00088	0.0470	685	0.282382	1.04	0.9	1.52
NT_P_55_1	0.28235	1.9E-05	0.00019	0.0121	566	0.282346	-2.92	0.7	1.68
NT_P_56_1	0.28227	2.5E-05	0.00062	0.0307	1073	0.282254	5.25	0.9	1.56
NT_P_57_1	0.28187	3.2E-05	0.00116	0.0582	1043	0.281849	-9.79	1.1	2.46
NT_P_58_1	0.28255	2.2E-05	0.00060	0.0323	552	0.282544	3.79	0.8	1.24
NT_P_59_1	0.28103	2.6E-05	0.00065	0.0308	2685	0.280994	-2.35	0.9	3.28
NT_P_6_1	0.28207	3.2E-05	0.00082	0.0367	1079	0.282051	-1.81	1.1	2.00
NT_P_60_1	0.28249	3.5E-05	0.00114	0.0606	662	0.282477	3.86	1.2	1.33
NT_P_61_1	0.28213	3.0E-05	0.00057	0.0299	1118	0.282119	1.49	1.0	1.83
NT_P_62_1	0.28233	3.8E-05	0.00043	0.0224	540	0.282328	-4.12	1.3	1.73
NT_P_63_1	0.28159	2.6E-05	0.00100	0.0466	1831	0.281558	-2.12	0.9	2.60
NT_P_64_1	0.28099	4.4E-05	0.00119	0.0633	2744	0.280925	-3.40	1.5	3.39
NT_P_66_1	0.28093	2.2E-05	0.00079	0.0411	2704	0.280886	-5.74	0.8	3.50
NT_P_68_1	0.28263	4.1E-05	0.00159	0.0838	648	0.282607	8.16	1.4	1.04
NT_P_71_1	0.28230	3.7E-05	0.00100	0.0505	1103	0.282280	6.86	1.3	1.48
NT_P_74_1	0.28216	2.5E-05	0.00081	0.0391	1172	0.282138	3.40	0.9	1.75
NT_P_77_1	0.28169	2.6E-05	0.00042	0.0224	603	0.281690	-25.32	0.9	3.08
Tomahawk Formation									
NT_T_10_1	0.28179	2.5E-05	0.00090	0.0384	1604	0.281766	0.04	0.9	2.30
NT_T_11_1	0.28137	3.4E-05	0.00055	0.0282	2041	0.281348	-4.73	1.2	2.92
NT_T_12_1	0.28227	2.9E-05	0.00078	0.0326	779	0.282261	-1.15	1.0	1.73
NT_T_13_1	0.28090	3.4E-05	0.00074	0.0375	2693	0.280866	-6.69	1.2	3.55
NT_T_14_1	0.28180	3.4E-05	0.00054	0.0277	555	0.281798	-22.59	1.2	2.88
NT_T_16_1	0.28158	4.5E-05	0.00077	0.0408	1710	0.281550	-5.19	1.6	2.69
NT_T_17_1	0.28163	2.7E-05	0.00098	0.0476	1723	0.281601	-3.07	0.9	2.58
NT_T_18_1	0.28223	4.6E-05	0.00064	0.0342	624	0.282222	-6.01	1.6	1.91
NT_T_19_1	0.28167	3.0E-05	0.00048	0.0230	1776	0.281654	0.03	1.0	2.43
NT_T_21_1	0.28226	3.0E-05	0.00051	0.0229	520	0.282257	-7.09	1.0	1.90
NT_T_22_1	0.28069	2.3E-05	0.00172	0.0818	3282	0.280579	-3.04	0.8	3.80
NT_T_23_1	0.28215	2.6E-05	0.00094	0.0551	565	0.282141	-10.20	0.9	2.13
NT_T_28_1	0.28229	2.2E-05	0.00061	0.0285	1016	0.282281	4.92	0.8	1.54
NT_T_29_1	0.28188	1.9E-05	0.00061	0.0272	1181	0.281862	-6.19	0.7	2.35
NT_T_33_1	0.28225	2.2E-05	0.00059	0.0290	981	0.282236	2.55	0.8	1.66
NT_T_34_1	0.28188	2.8E-05	0.00030	0.0143	538	0.281873	-20.29	1.0	2.73
NT_T_36_1	0.28210	2.4E-05	0.00068	0.0316	1162	0.282088	1.38	0.9	1.87
NT_T_39_1	0.28220	2.1E-05	0.00048	0.0226	1320	0.282187	8.49	0.7	1.56
NT_T_4_1	0.28232	3.1E-05	0.00025	0.0144	587	0.282314	-3.59	1.1	1.73
NT_T_40_1	0.28262	2.7E-05	0.00054	0.0255	543	0.282618	6.20	1.0	1.09
NT_T_42_1	0.28207	3.4E-05	0.00162	0.0845	1082	0.282041	-2.11	1.2	2.02
NT_T_43_1	0.28131	3.0E-05	0.00099	0.0429	2102	0.281275	-5.91	1.1	3.04
NT_T_44_1	0.28220	2.6E-05	0.00059	0.0293	646	0.282189	-6.67	0.9	1.97
NT_T_45_1	0.28249	3.5E-05	0.00114	0.0609	574	0.282474	1.79	1.2	1.39
NT_T_46_1	0.28131	2.9E-05	0.00045	0.0227	1951	0.281297	-8.63	1.0	3.09
NT_T_5_1	0.28247	3.4E-05	0.00063	0.0321	596	0.282459	1.75	1.2	1.41
NT_T_50_1	0.28212	2.9E-05	0.00048	0.0221	1412	0.282105	7.68	1.0	1.68
NT_T_51_1	0.28224	3.6E-05	0.00071	0.0343	628	0.282228	-5.71	1.3	1.90
NT_T_56_1	0.28228	3.5E-05	0.00122	0.0612	1040	0.282257	4.59	1.2	1.58
NT_T_57_1	0.28250	2.0E-05	0.00006	0.0032	532	0.282497	1.67	0.7	1.36
NT_T_61_1	0.28221	2.4E-05	0.00078	0.0379	874	0.282195	-1.35	0.8	1.81
NT_T_65_1	0.28227	3.1E-05	0.00100	0.0501	608	0.282256	-5.16	1.1	1.85
NT_T_67_1	0.28187	2.8E-05	0.00031	0.0147	844	0.281866	-13.69	1.0	2.55
NT_T_68_1	0.28136	3.7E-05	0.00104	0.0446	1860	0.281323	-9.82	1.3	3.09
NT_T_7_1	0.28234	2.3E-05	0.00052	0.0223	1309	0.282331	13.36	0.8	1.24
NT_T_9_1	0.28202	3.6E-05	0.00059	0.0332	1115	0.282006	-2.58	1.2	2.08
SESSION 2									
Lower Stanovos Gneiss									
LSG_01	0.28226	2.9E-05	0.00124	0.0477	1181	0.282236	7.07	1.0	1.53
LSG_02	0.28165	1.9E-05	0.00080	0.0303	1786	0.281624	-0.82	0.7	2.49
LSG_03	0.28201	1.9E-05	0.00087	0.0312	1535	0.281980	6.08	0.7	1.87
LSG_04	0.28217	3.4E-05	0.00105	0.0426	1241	0.282149	5.36	1.2	1.69
LSG_05	0.28223	4.3E-05	0.00148	0.0539	1276	0.282198	7.89	1.5	1.56
LSG_08	0.28176	2.0E-05	0.00066	0.0250	1753	0.281739	2.50	0.7	2.26
LSG_12	0.28204	2.2E-05	0.00085	0.0350	1573	0.282010	8.00	0.8	1.79
LSG_13	0.28207	2.3E-05	0.00072	0.0244	1393	0.282049	5.23	0.8	1.81
LSG_14	0.28197	2.0E-05	0.00108	0.0396	1545	0.281935	4.69	0.7	1.97
LSG_15	0.28145	2.3E-05	0.00081	0.0364	1842	0.281418	-6.86	0.8	2.90
LSG_16	0.28124	3.0E-05	0.00110	0.0408	2648	0.281181	3.43	1.1	2.91
LSG_17	0.28204	2.2E-05	0.00087	0.0328	1441	0.282019	5.28	0.8	1.85
LSG_21	0.28228	2.7E-05	0.00110	0.0437	1043	0.282258	4.70	0.9	1.57
LSG_23	0.28233	2.8E-05	0.00147	0.0617	1134	0.282296	8.13	1.0	1.43
LSG_25	0.28205	2.2E-05	0.00074	0.0307	1485	0.282026	6.56	0.8	1.80
LSG_27	0.28154	2.2E-05	0.00039	0.0153	1720	0.281527	-5.79	0.8	2.74

LA-MC-ICP-MS Lu-Hf Isotopic Results

Analysis	$^{176}Hf/^{177}Hf$	2 S.E.	$^{176}Lu/^{177}Hf$	$^{176}Yb/^{177}Hf$	U/Pb age (Ma)	$Hf_{initial}$	$\varepsilon Hf_{(T)}$	1σ	$T_{DM(crustal)}$ (Ga)
LSG_30	0.28205	2.5E-05	0.00115	0.0423	1181	0.282024	-0.43	0.9	2.00
LSG_31	0.28237	2.7E-05	0.00096	0.0395	1058	0.282350	8.31	0.9	1.36
LSG_32	0.28161	1.7E-05	0.00064	0.0249	1885	0.281586	0.13	0.6	2.51
LSG_33	0.28207	2.6E-05	0.00123	0.0490	1463	0.282040	6.54	0.9	1.79
LSG_34	0.28214	3.2E-05	0.00262	0.1002	1490	0.282069	8.20	1.1	1.71
LSG_36	0.28157	2.1E-05	0.00070	0.0272	1858	0.281549	-1.80	0.7	2.61
LSG_37	0.28158	1.7E-05	0.00043	0.0173	1837	0.281564	-1.76	0.6	2.59
LSG_39	0.28230	2.5E-05	0.00152	0.0632	1052	0.282269	5.29	0.9	1.54
LSG_41	0.28228	1.6E-05	0.00060	0.0237	1090	0.282263	5.96	0.6	1.53
LSG_42	0.28125	1.6E-05	0.00029	0.0107	1779	0.281237	-14.73	0.5	3.32
LSG_44	0.28218	2.3E-05	0.00106	0.0381	1192	0.282159	4.61	0.8	1.69
LSG_45	0.28220	2.0E-05	0.00113	0.0413	1098	0.282179	3.16	0.7	1.71
LSG_47	0.28224	2.8E-05	0.00165	0.0701	1100	0.282211	4.33	1.0	1.64
LSG_48	0.28203	2.1E-05	0.00093	0.0332	1394	0.282005	3.74	0.7	1.91
LSG_49	0.28199	3.4E-05	0.00149	0.0615	1747	0.281945	9.68	1.2	1.82
LSG_50	0.28196	2.0E-05	0.00071	0.0281	1390	0.281946	1.53	0.7	2.04
LSG_51	0.28205	3.0E-05	0.00133	0.0497	1586	0.282011	8.33	1.1	1.78
LSG_52	0.28194	2.1E-05	0.00095	0.0354	1615	0.281909	5.36	0.7	1.98
LSG_54	0.28210	2.0E-05	0.00085	0.0330	1120	0.282086	0.36	0.7	1.90
LSG_56	0.28194	1.8E-05	0.00056	0.0216	1612	0.281927	5.96	0.6	1.94
LSG_57	0.28213	2.7E-05	0.00165	0.0535	1448	0.282085	7.78	1.0	1.70
LSG_58	0.28119	1.8E-05	0.00032	0.0118	2547	0.281174	0.83	0.6	2.99
LSG_59	0.28196	2.2E-05	0.00069	0.0271	1556	0.281935	4.95	0.8	1.96
LSG_60	0.28148	2.4E-05	0.00165	0.0637	1901	0.281423	-5.30	0.8	2.85
LSG_63	0.28174	2.1E-05	0.00067	0.0260	1119	0.281722	-12.58	0.7	2.69
LSG_67	0.28198	2.4E-05	0.00107	0.0402	1587	0.281944	5.95	0.9	1.92
LSG_69	0.28152	3.4E-05	0.00047	0.0196	1685	0.281502	-7.48	1.2	2.81
LSG_70	0.28158	1.9E-05	0.00031	0.0129	1976	0.281565	1.46	0.7	2.50
Heavitree Quartzite									
HTQ_01_1	0.28178	2.6E-05	0.00124	0.0492	1714	0.281736	1.51	0.9	2.29
HTQ_02_1	0.28162	3.4E-05	0.00045	0.0213	1757	0.281603	-2.22	1.2	2.55
HTQ_03_1	0.28190	2.2E-05	0.00054	0.0214	1144	0.281892	-5.97	0.8	2.31
HTQ_04_1	0.28170	2.1E-05	0.00049	0.0191	1679	0.281689	-0.98	0.7	2.42
HTQ_08_1	0.28194	1.8E-05	0.00060	0.0232	1619	0.281920	5.87	0.6	1.95
HTQ_11_1	0.28194	2.2E-05	0.00088	0.0351	1144	0.281919	-5.03	0.8	2.25
HTQ_12_1	0.28156	2.8E-05	0.00054	0.0208	1778	0.281544	-3.84	1.0	2.67
HTQ_13_1	0.28190	5.0E-05	0.00126	0.0554	1601	0.281857	3.22	1.7	2.10
HTQ_14_1	0.28168	3.0E-05	0.00117	0.0498	1761	0.281637	-0.93	1.1	2.48
HTQ_15_1	0.28193	2.9E-05	0.00099	0.0365	1588	0.281903	4.53	1.0	2.01
HTQ_16_1	0.28169	4.4E-05	0.00077	0.0289	1807	0.281667	1.20	1.5	2.38
HTQ_19_1	0.28195	2.3E-05	0.00089	0.0351	1583	0.281922	5.10	0.8	1.97
HTQ_20_1	0.28169	3.3E-05	0.00173	0.0778	1735	0.281629	-1.82	1.2	2.51
HTQ_22_1	0.28189	2.8E-05	0.00091	0.0331	1595	0.281866	3.38	1.0	2.09
HTQ_23_1	0.28205	3.4E-05	0.00138	0.0577	1321	0.282013	2.34	1.2	1.93
HTQ_24_1	0.28193	2.5E-05	0.00067	0.0251	1592	0.281912	4.94	0.9	1.99
HTQ_25_1	0.28195	2.6E-05	0.00076	0.0297	1565	0.281932	5.03	0.9	1.96
HTQ_26_1	0.28222	2.6E-05	0.00099	0.0354	1305	0.282195	8.45	0.9	1.55
HTQ_30_1	0.28165	3.9E-05	0.00200	0.0757	1753	0.281582	-3.07	1.4	2.60
HTQ_31_1	0.28197	2.6E-05	0.00070	0.0293	1597	0.281944	6.21	0.9	1.91
HTQ_33_1	0.28192	2.2E-05	0.00084	0.0328	1584	0.281891	4.04	0.8	2.04
HTQ_35_1	0.28166	2.7E-05	0.00100	0.0404	1772	0.281629	-0.97	0.9	2.49
HTQ_36_1	0.28188	2.9E-05	0.00085	0.0294	1618	0.281858	3.64	1.0	2.09
HTQ_39_1	0.28146	1.8E-05	0.00058	0.0236	2076	0.281441	-0.63	0.6	2.71
HTQ_40_1	0.28195	2.2E-05	0.00070	0.0269	1587	0.281934	5.62	0.8	1.94
HTQ_41_1	0.28162	2.2E-05	0.00053	0.0197	1640	0.281602	-4.95	0.8	2.63
HTQ_43_1	0.28173	2.4E-05	0.00139	0.0495	1743	0.281681	0.23	0.8	2.39
HTQ_46_1	0.28167	2.3E-05	0.00073	0.0295	1765	0.281643	-0.64	0.8	2.46
HTQ_47_1	0.28204	3.4E-05	0.00148	0.0603	1565	0.281999	7.40	1.2	1.82
HTQ_49_1	0.28196	4.3E-05	0.00110	0.0460	1585	0.281923	5.19	1.5	1.97
HTQ_51_1	0.28160	2.1E-05	0.00060	0.0241	1769	0.281582	-2.69	0.7	2.59
HTQ_53_1	0.28166	2.8E-05	0.00073	0.0287	1656	0.281639	-3.26	1.0	2.54
HTQ_55_1	0.28184	4.5E-05	0.00117	0.0458	1619	0.281809	1.91	1.6	2.19
HTQ_58_1	0.28209	3.0E-05	0.00069	0.0274	1212	0.282069	1.86	1.0	1.88
HTQ_59_1	0.28161	2.5E-05	0.00059	0.0250	1648	0.281596	-4.98	0.9	2.63
HTQ_60_1	0.28190	2.7E-05	0.00061	0.0240	1138	0.281884	-6.40	0.9	2.33
HTQ_61_1	0.28165	4.9E-05	0.00088	0.0349	1751	0.281624	-1.63	1.7	2.51
HTQ_62_1	0.28210	1.7E-05	0.00056	0.0221	1233	0.282089	3.03	0.6	1.82
HTQ_63_1	0.28204	2.3E-05	0.00079	0.0314	1494	0.282013	6.31	0.8	1.83
HTQ_64_1	0.28163	1.9E-05	0.00037	0.0154	1721	0.281621	-2.41	0.6	2.54
HTQ_65_1	0.28189	2.6E-05	0.00111	0.0430	1628	0.281859	3.90	0.9	2.08
HTQ_66_1	0.28168	2.7E-05	0.00149	0.0549	1651	0.281633	-3.59	1.0	2.55

LA-MC-ICP-MS Lu-Hf Isotopic Results

Analysis	$^{176}Hf/^{177}Hf$	2 S.E.	$^{176}Lu/^{177}Hf$	$^{176}Yb/^{177}Hf$	U/Pb age (Ma)	$Hf_{initial}$	$\varepsilon Hf_{(T)}$	1σ	$T_{DM(crustal)}$ (Ga)
Arumbera Sandstone									
AS_02	0.28208	2.5E-05	0.00056	0.0203	1199	0.282069	1.53	0.9	1.89
AS_03	0.28199	3.3E-05	0.00093	0.0327	1507	0.281962	4.79	1.2	1.93
AS_05	0.28224	3.4E-05	0.00119	0.0501	605	0.282231	-6.12	1.2	1.90
AS_06	0.28191	4.1E-05	0.00092	0.0371	1592	0.281886	4.05	1.4	2.04
AS_07	0.28215	2.5E-05	0.00063	0.0257	996	0.282137	-0.63	0.9	1.86
AS_08	0.28210	2.3E-05	0.00065	0.0254	1188	0.282084	1.84	0.8	1.86
AS_09	0.28194	3.9E-05	0.00129	0.0485	1122	0.281913	-5.71	1.4	2.27
AS_10	0.28185	4.0E-05	0.00111	0.0416	1233	0.281827	-6.24	1.4	2.39
AS_11	0.28179	2.8E-05	0.00050	0.0214	1156	0.281783	-9.56	1.0	2.53
AS_13	0.28210	2.7E-05	0.00072	0.0291	1170	0.282080	1.29	0.9	1.88
AS_14	0.28214	4.9E-05	0.00112	0.0472	1160	0.282112	2.19	1.7	1.82
AS_15	0.28197	4.2E-05	0.00120	0.0487	1563	0.281932	5.00	1.5	1.96
AS_16	0.28185	3.8E-05	0.00070	0.0304	1154	0.281839	-7.62	1.3	2.41
AS_17	0.28167	3.0E-05	0.00076	0.0294	1189	0.281653	-13.45	1.0	2.79
AS_18	0.28151	3.2E-05	0.00095	0.0410	1797	0.281479	-5.69	1.1	2.79
AS_19	0.28210	2.7E-05	0.00059	0.0225	1227	0.282089	2.88	0.9	1.83
AS_21	0.28211	2.9E-05	0.00084	0.0288	1184	0.282088	1.88	1.0	1.86
AS_22	0.28209	4.8E-05	0.00107	0.0497	1159	0.282064	0.46	1.7	1.92
AS_23	0.28166	2.7E-05	0.00132	0.0519	1736	0.281612	-2.38	0.9	2.55
AS_24	0.28214	3.1E-05	0.00077	0.0325	1139	0.282125	2.19	1.1	1.80
AS_25	0.28207	3.6E-05	0.00076	0.0330	1199	0.282057	1.12	1.2	1.91
AS_26	0.28188	3.6E-05	0.00135	0.0501	1100	0.281851	-8.44	1.3	2.42
AS_28	0.28205	2.6E-05	0.00065	0.0234	1569	0.282027	8.51	0.9	1.75
AS_30	0.28231	3.9E-05	0.00062	0.0274	951	0.282304	4.26	1.4	1.53
AS_31	0.28135	3.7E-05	0.00069	0.0306	2500	0.281313	4.70	1.3	2.72
AS_35	0.28167	2.7E-05	0.00068	0.0270	1566	0.281651	-4.90	1.0	2.57
AS_36	0.28217	3.7E-05	0.00085	0.0374	1190	0.282150	4.21	1.3	1.72
AS_38	0.28207	3.8E-05	0.00111	0.0405	1241	0.282045	1.67	1.3	1.91
AS_40	0.28216	3.2E-05	0.00062	0.0268	1106	0.282147	2.19	1.1	1.78
AS_43	0.28161	3.3E-05	0.00131	0.0524	1785	0.281564	-2.98	1.2	2.62
AS_45	0.28204	2.5E-05	0.00049	0.0195	1201	0.282034	0.34	0.9	1.96
AS_46	0.28213	3.4E-05	0.00110	0.0379	1106	0.282104	0.70	1.2	1.87
AS_47	0.28210	3.6E-05	0.00088	0.0379	1188	0.282076	1.55	1.3	1.88
AS_48	0.28133	2.6E-05	0.00104	0.0392	1883	0.281295	-10.28	0.9	3.13
AS_49	0.28209	2.9E-05	0.00146	0.0533	1182	0.282057	0.75	1.0	1.92
AS_51	0.28185	3.0E-05	0.00078	0.0268	1601	0.281827	2.13	1.0	2.17
AS_53	0.28139	4.1E-05	0.00134	0.0488	1775	0.281349	-10.83	1.4	3.08
AS_54	0.28107	3.3E-05	0.00045	0.0185	2496	0.281052	-4.68	1.2	3.27
AS_56	0.28172	4.4E-05	0.00112	0.0424	1729	0.281683	-0.04	1.6	2.40
AS_57	0.28215	4.4E-05	0.00079	0.0333	1002	0.282132	-0.69	1.5	1.87
AS_58	0.28209	3.4E-05	0.00078	0.0263	1182	0.282070	1.20	1.2	1.90
AS_59	0.28197	2.7E-05	0.00052	0.0221	1093	0.281962	-4.64	0.9	2.19
AS_60	0.28182	3.4E-05	0.00155	0.0497	1673	0.281773	1.88	1.2	2.24
AS_61	0.28152	3.6E-05	0.00119	0.0553	1499	0.281486	-12.29	1.3	2.96

APPENDIX C: WHOLE-ROCK GEOCHEMISTRY

	BG-09	BG-03	BG-07	BG-08	IG -10	IG-222A	IG-02	UBG-2	UBG-4
Major elements (wt %)									
SiO_2	76.47	61.18	59.62	56.36	70.57	53.22	55.55	61.50	54.48
TiO_2	0.56	0.83	1.18	0.81	0.68	0.80	1.04	1.32	1.11
Al_2O_3	10.96	17.08	17.55	19.10	13.10	23.32	18.74	13.78	20.37
Fe_2O_3	0.65	1.72	1.20	1.18	2.85	1.71	1.80	1.49	1.76
FeO	3.53	5.36	6.38	7.20	3.96	5.06	7.39	8.74	7.34
MnO	0.07	0.12	0.11	0.21	0.10	0.10	0.22	0.22	0.18
MgO	1.83	3.30	3.34	5.07	2.28	4.83	4.18	4.96	4.47
CaO	1.34	2.77	1.10	0.94	1.47	3.75	2.61	0.42	0.94
Na_2O	1.52	2.75	1.24	0.81	3.29	4.09	3.56	0.40	1.24
K_2O	2.37	3.09	5.05	5.94	0.48	1.79	3.42	5.16	5.57
P_2O_5	0.08	0.18	0.12	0.06	0.15	0.15	0.07	0.11	0.09
LOI	1.06	1.70	3.45	2.66	1.14	1.23	1.60	2.20	2.67
Total	**100.44**	**100.08**	**100.34**	**100.34**	**100.07**	**100.05**	**100.18**	**100.30**	**100.22**
Fe_2O_3T	4.57	7.68	8.29	9.18	7.25	7.33	10.01	11.20	9.92
Trace elements (ppm)									
Rb	118	191	248	310	20	105	150	249	289
Sr	123	180	110	78	236	361	164	42	79
Y	28	20	21	38	39	42	43	43	24
Zr	206	161	183	140	193	203	210	244	156
V	84	144	150	165	101	140	175	197	171
Ni	24	24	45	48	28	40	49	70	62
Cr	71	89	110	80	62	42	93	215	192
Nb	11	17	21	17	9	16	18	25	25
Ga	14	22	23	25	17	28	23	21	28
Cu	15	70	6	7	5	2	47	6	32
Zn	61	105	111	139	23	58	133	175	155
Co	66	59	49	62	75	57	55	62	63
Ba	546	482	1210	1653	183	328	784	990	1004
La	30	29	24	40	37	32	27	33	22
Ce	59	69	64	140	78	78	61	108	57
U	3	6	1	2	3	3	1	4	<0.5
Th	15	20	26	27	21	20	21	42	20
Sc	9	12	15	21	7	14	22	25	19
Pb	35	21	30	20	<1	3	32	14	27

Fe_2O_3T, Fe^{3+} determined by ferrous titration; LOI, Loss on Ignition

APPENDIX D: REPRESENTATIVE ELECTRON MICROPROBE ANALYSES

Brady Gneiss metapelites

	BG-07B							**BG-08**						**UBG-4B**					
	bi	gt core	gt near rim	gt rim	ilm	mu	pl	bi	gt core	gt near rim	gt rim	mu	pl	bi	gt core	gt near rim	gt rim	mu	pl
SiO_2	35.66	38.18	36.82	37.66	0.02	44.83	60.56	35.20	36.88	37.56	37.09	44.23	56.85	36.06	37.912	36.997	38.041	46.17	61.08
TiO_2	2.49	0.03	0.01	0.02	53.45	1.00	0.01	2.51	0.01	0.01	0.04	0.45	b.d.l.	2.57	-0.023	0.008	0.024	0.60	0.00
$Al2O_3$	18.15	21.63	20.99	21.29	0.05	33.64	24.62	18.33	21.07	21.40	21.08	33.40	25.50	18.96	b.d.l.	20.974	b.d.l.	34.77	24.70
Cr_2O_3	0.03	0.03	0.00	0.04	0.00	0.01	0.00	0.04	0.02	0.01	0.03	0.03	b.d.l.	0.03	21.539	0.027	21.471	0.02	0.00
FeO	19.44	31.32	33.21	33.09	44.14	1.30	0.00	17.01	28.68	29.47	30.83	1.48	0.01	17.71	31.348	31.782	31.670	1.47	0.04
MnO	0.06	3.74	3.08	2.94	1.00	0.01	b.d.l.	0.12	5.68	4.68	4.58	0.00	0.01	0.13	4.796	4.162	4.143	0.03	0.00
MgO	8.99	3.90	3.67	3.02	0.12	0.71	0.01	10.24	4.22	4.30	3.51	0.94	0.00	9.63	4.213	3.922	3.550	0.88	b.d.l.
ZnO	0.04	0.02	0.02	b.d.l.	0.11	0.02	b.d.l.	0.08	0.03	-0.01	0.00	0.03	0.00	0.06	0.045	0.011	0.094	0.00	0.00
CaO	b.d.l.	2.36	2.32	2.71	0.01	b.d.l.	6.78	0.02	2.88	2.82	3.08	0.00	8.66	b.d.l.	1.283	1.939	1.957	b.d.l.	6.61
Na_2O	0.22	0.03	0.02	0.02	0.01	0.81	7.67	0.28	0.02	0.02	0.00	0.75	6.76	0.24	0.013	0.011	0.007	0.62	7.97
K_2O	9.14	0.00	0.00	0.01	0.03	9.95	0.14	8.96	0.00	0.01	0.01	9.99	0.16	9.45	0.002	0.004	0.015	10.25	0.21
Total (wt%)	94.21	101.22	100.15	100.79	98.95	92.24	99.74	92.80	99.51	100.27	100.23	91.31	97.91	94.83	101.13	99.84	100.97	94.78	100.60
No. oxygens	11	12	12	12	3	11	8	11	12	12	12	11	8	11	12	12	12	11	8
Si	2.44	3.01	2.95	3.00	0.00	3.09	2.71	2.42	2.95	2.98	2.96	3.07	2.60	2.44	3.264	2.966	3.290	3.09	2.70
Ti	0.13	0.00	0.00	0.00	1.03	0.05	0.00	0.13	0.00	0.00	0.00	0.02	0.00	0.13	-0.002	0.000	0.002	0.03	0.00
Al	1.46	2.01	1.98	2.00	0.00	2.73	1.30	1.49	1.99	2.00	1.98	2.73	1.37	1.51	0.000	1.981	0.000	2.75	1.29
Cr	0.00	0.00	0.00	0.00	0.00	0.00	0.00	0.00	0.00	0.00	0.00	0.00	0.00	0.00	1.466	0.002	1.468	0.00	0.00
Fe^{3+}	2.42	0.00	0.13	0.00	0.00	0.00	0.00	2.44	0.11	0.04	0.09	0.06	0.04	2.40	0.011	0.087	0.000	0.00	0.00
Fe^{2+}	b.d.l.	2.06	2.09	2.20	0.94	0.08	0.00	b.d.l.	1.81	1.91	1.97	0.03	b.d.l.	b.d.l.	2.246	2.044	2.290	0.08	0.00
Mn^{2+}	0.00	0.25	0.21	0.20	0.02	0.00	0.00	0.01	0.39	0.31	0.31	0.00	0.00	0.01	0.350	0.283	0.303	0.00	0.00
Mg	0.92	0.46	0.44	0.36	0.00	0.07	0.00	1.05	0.50	0.51	0.42	0.10	0.00	0.97	0.541	0.469	0.458	0.09	0.00
Zn	0.00	0.00	0.00	0.00	0.00	0.00	0.00	0.00	0.00	0.00	0.00	0.00	0.00	0.00	0.003	0.001	0.006	0.00	0.00
Ca	0.00	0.20	0.20	0.23	0.00	0.00	0.32	0.00	0.25	0.24	0.26	0.00	0.42	0.00	0.118	0.167	0.181	0.00	0.31
Na	0.03	0.00	0.00	0.00	0.00	0.11	0.66	0.04	0.00	0.00	0.00	0.10	0.60	0.03	0.002	0.002	0.001	0.08	0.68
K	0.80	0.00	0.00	0.00	0.00	0.87	0.01	0.79	0.00	0.00	0.00	0.88	0.01	0.81	0.000	0.000	0.002	0.88	0.01
Total cations	6.90	8.00	8.00	8.00	2.00	7.00	5.00	6.90	8.00	8.00	8.00	7.00	5.00	6.90	8.00	8.00	8.00	7.00	5.00
X_{alm}	-	0.69	0.71	0.74	-	-	-	-	0.61	0.64	0.67	-	-	-	0.690	0.690	0.708	-	-
X_{py}	-	0.15	0.15	0.12	-	-	-	-	0.17	0.17	0.14	-	-	-	0.166	0.158	0.142	-	-
X_{grs}	-	0.07	0.00	0.08	-	-	-	-	0.03	0.06	0.05	-	-	-	0.031	0.013	0.056	-	-
X_{sps}	-	0.08	0.07	0.07	-	-	-	-	0.13	0.11	0.10	-	-	-	0.107	0.095	0.094	-	-
$X_{Mg(total)}$	0.27	0.18	0.16	0.14	-	0.49		0.30	0.21	0.21	0.17	0.53		0.29	0.172	0.168	0.150	0.51	
X_{Na}	-		-	-	-	-	0.67	-	-	-	-	-	0.59	-	-	-	-	-	0.69

Irindina Gneiss mafic granulites

	IG-26B						**IG-23A**						**IG-16A**						**IG-28A**				
	cpx	gt core	gt rim	hb	ilm	pl	cpx	gt core	gt rim	hb	ilm	pl	cpx	gt core	gt rim	hb	ilm	pl	cpx	gt core	gt rim	hb	pl
SiO_2	53.60	38.66	38.22	44.13	0.01	57.50	53.38	38.82	38.27	45.47	0.02	56.17	52.70	38.88	37.87	44.59	0.03	58.33	52.63	38.57	37.89	44.16	57.67
TiO_2	0.15	0.10	0.04	1.82	52.46	0.01	0.13	0.15	0.07	1.12	50.71	0.04	0.14	0.17	0.07	1.24	51.69	b.d.l.	0.12	0.14	0.02	1.01	b.d.l.
$Al2O_3$	1.63	21.75	0.07	11.40	0.03	26.39	1.44	21.33	21.14	10.32	0.03	27.46	1.43	21.70	21.05	11.04	0.03	26.21	1.21	21.51	0.00	11.67	26.31
Cr_2O_3	0.06	0.06	21.16	0.06	0.02	b.d.l.	0.04	0.02	0.01	0.02	0.03	0.02	0.02	0.08	0.07	0.02	0.04	0.00	0.02	0.03	21.21	0.01	b.d.l.
FeO	10.18	23.37	26.64	15.09	45.21	0.03	9.60	24.10	26.29	16.29	45.95	0.06	10.93	24.87	26.04	16.64	45.16	b.d.l.	10.91	24.54	25.58	17.44	0.03
MnO	0.37	0.88	2.04	0.16	0.86	0.01	0.22	1.09	1.96	0.18	1.77	0.02	0.43	1.28	2.76	0.25	0.99	0.01	0.33	1.28	3.55	0.24	b.d.l.
MgO	12.35	5.89	4.63	10.41	0.77	0.00	12.22	5.18	3.61	10.20	0.20	b.d.l.	11.37	4.65	3.01	9.48	0.66	b.d.l.	11.29	4.69	2.48	8.88	0.00
ZnO	0.00	0.03	0.04	0.02	0.00	0.03	0.03	0.01	0.01	0.01	0.05	b.d.l.	0.03	0.07	0.01	0.05	b.d.l.	0.03	0.03	0.05	b.d.l.	0.06	0.02
CaO	23.07	9.72	7.43	11.55	0.01	9.18	23.89	9.79	9.11	12.14	0.01	10.40	22.96	9.75	9.44	11.93	0.01	8.60	23.48	9.85	9.95	11.96	9.00
Na_2O	0.33	0.00	0.01	1.47	0.02	6.43	0.36	0.03	0.01	1.16	b.d.l.	5.81	0.40	0.02	0.02	1.43	0.00	6.70	0.32	b.d.l.	b.d.l.	1.34	6.51
K_2O	0.00	0.00	0.00	0.94	-0.01	0.15	0.01	b.d.l.	0.01	0.61	0.00	0.09	0.04	0.00	0.01	0.74	0.00	0.16	0.02	0.01	0.00	0.86	0.16
Total (wt%)	101.73	100.46	100.27	97.04	99.40	99.72	101.32	100.52	100.50	97.52	98.73	100.05	100.44	101.48	100.34	97.42	98.56	99.97	100.35	100.64	100.67	97.64	99.64
No. oxygens	6	12	12	23	3	8	6	12	12	23	3	8	6	12	12	23	3	8	6	12	12	23	8
Si	1.98	2.98	3.25	7.23	0.00	2.59	1.98	3.00	3.00	7.47	0.00	2.53	1.98	2.99	2.98	7.33	0.00	2.61	1.98	2.99	3.24	7.27	2.59
Ti	0.00	0.01	0.00	0.22	1.00	0.00	0.00	0.01	0.00	0.14	0.97	0.00	0.00	0.01	0.00	0.15	0.99	0.00	0.00	0.01	0.00	0.12	0.00
Al	0.07	1.97	0.01	2.20	0.00	1.40	0.06	1.94	1.95	2.00	0.00	1.46	0.06	1.97	1.95	2.14	0.00	1.38	0.05	1.96	0.00	2.26	1.39
Cr	0.00	0.00	1.42	0.01	0.00	0.00	0.00	0.00	0.00	0.00	0.00	0.00	0.00	0.00	0.00	0.00	0.00	0.00	0.00	0.00	1.44	0.00	0.00
Fe^{3+}	0.00	0.06	0.06	0.00	0.01	0.00	0.00	0.03	0.04	0.00	0.05	0.00	0.00	0.03	0.07	0.00	0.02	0.00	0.00	0.04	0.07	0.00	0.00
Fe^{2+}	0.31	1.44	1.84	2.07	0.95	0.00	0.30	1.52	1.68	2.24	0.93	0.00	0.34	1.57	1.65	2.29	0.95	0.00	0.34	1.55	1.76	2.40	0.00
Mn^{2+}	0.01	0.06	0.15	0.02	0.02	0.00	0.01	0.07	0.13	0.03	0.04	0.00	0.01	0.08	0.18	0.04	0.02	0.00	0.01	0.08	0.26	0.03	0.00
Mg	0.68	0.68	0.59	2.54	0.03	0.00	0.67	0.60	0.42	2.50	0.01	0.00	0.64	0.53	0.35	2.33	0.03	0.00	0.63	0.54	0.32	2.18	0.00
Zn	0.00	0.00	0.00	0.00	0.00	0.00	0.00	0.00	0.00	0.00	0.00	0.00	0.00	0.00	0.00	0.01	0.00	0.00	0.00	0.00	0.00	0.01	0.00
Ca	0.91	0.80	0.68	2.03	0.00	0.44	0.95	0.81	0.77	2.14	0.00	0.50	0.92	0.80	0.80	2.10	0.00	0.41	0.95	0.82	0.91	2.11	0.43
Na	0.02	0.00	0.00	0.47	0.00	0.56	0.03	0.00	0.00	0.37	0.00	0.51	0.03	0.00	0.00	0.46	0.00	0.58	0.02	0.00	0.00	0.43	0.57
K	0.00	0.00	0.00	0.20	0.00	0.01	0.00	0.00	0.00	0.13	0.00	0.00	0.00	0.00	0.00	0.16	0.00	0.01	0.00	0.00	0.00	0.18	0.01
Total cations	4.00	8.00	8.00	17.00	2.00	5.00	4.00	8.00	8.00	17.00	2.00	5.00	4.00	8.00	8.00	17.00	2.00	5.00	4.00	8.00	8.00	17.00	5.00
X_{alm}	-	0.48	0.57	-	-	-	-	0.51	0.56	-	-	-	-	0.52	0.55	-	-	-	-	0.52	0.54	-	-
X_{py}	-	0.23	0.18	-	-	-	-	0.20	0.14	-	-	-	-	0.18	0.12	-	-	-	-	0.18	0.10	-	-
X_{grs}	-	0.24	0.18	-	-	-	-	0.25	0.23	-	-	-	-	0.25	0.23	-	-	-	-	0.25	0.25	-	-
X_{sps}	-	0.02	0.05	-	-	-	-	0.02	0.04	-	-	-	-	0.03	0.06	-	-	-	-	0.03	0.08	-	-
$X_{Mg(total)}$	0.68	0.31	0.24	0.55	0.03		0.69	0.28	0.20	0.53	0.01		0.65	0.25	0.17	0.50	0.03		0.65	0.25	0.15	0.48	
X_{Na}	-	-	-	-	-	0.56	-	-	-	-	-	0.50	-	-	-	-	-	0.59	-	-	-	-	0.57

	IG-23B						**IG-28B**						**IG-26A**						**IG-16B**					
	cpx	gt core	gt rim	hb	ilm	pl	cpx	gt core	gt rim	hb	ilm	pl	cpx	gt core	gt rim	hb	ilm	pl	cpx	gt core	gt rim	hb	ilm	pl
SiO_2	53.15	37.92	38.37	42.68	0.01	57.26	51.93	37.68	37.33	42.43	0.02	56.25	51.15	37.61	37.64	42.84	0.02	54.28	51.71	37.47	37.39	43.91	0.01	56.44
TiO_2	0.05	0.32	0.03	1.53	51.49	b.d.l.	0.08	0.23	0.18	1.50	52.71	b.d.l.	0.23	0.13	0.05	1.87	54.07	0.00	0.14	0.14	0.05	1.78	52.72	0.02
$Al2O_3$	1.42	21.21	0.03	12.64	0.02	26.56	1.08	20.89	20.63	11.21	0.01	26.21	2.08	21.00	20.87	11.68	0.05	27.33	1.30	21.16	20.99	10.01	b.d.l.	25.95
Cr_2O_3	0.02	0.05	21.23	0.06	0.01	b.d.l.	0.02	0.01	0.03	0.01	0.02	b.d.l.	0.04	0.06	0.05	0.11	0.04	0.00	0.00	0.06	0.08	0.09	0.03	0.01
FeO	9.96	24.07	25.71	16.34	45.19	0.01	10.84	25.28	25.27	17.40	45.02	0.06	10.33	24.32	27.09	15.52	44.01	0.05	10.58	24.74	25.44	15.92	45.23	0.00
MnO	0.30	1.37	2.64	0.33	1.28	0.00	0.34	1.68	3.81	0.27	1.62	b.d.l.	0.31	1.27	2.03	0.19	1.20	b.d.l.	0.43	1.59	3.54	0.30	1.42	0.02
MgO	12.09	4.97	3.08	9.21	0.44	0.00	11.33	4.37	2.36	8.91	0.61	0.00	11.99	5.18	3.71	10.01	0.43	b.d.l.	11.84	4.61	3.17	10.17	0.77	b.d.l.
ZnO	b.d.l.	b.d.l.	b.d.l.	0.02	b.d.l.	0.00	0.03	0.02	b.d.l.	b.d.l.	b.d.l.	0.00	0.00	0.01	0.04	0.03	0.06	0.02	0.00	0.04	0.01	0.03	0.08	0.00
CaO	23.62	10.08	9.77	11.64	0.01	9.17	24.42	10.16	10.62	12.24	0.04	9.40	23.21	10.07	8.69	12.00	0.01	10.92	24.22	10.03	9.38	11.95	0.00	9.04
Na_2O	0.29	0.03	0.00	1.44	0.01	6.62	0.30	0.01	0.01	1.45	b.d.l.	6.44	0.43	0.01	b.d.l.	1.57	0.00	5.65	0.37	0.01	0.01	1.54	0.01	6.61
K_2O	0.02	0.00	0.00	0.89	0.00	0.12	0.01	0.00	b.d.l.	0.89	0.00	0.13	0.00	0.00	0.00	0.89	0.00	0.16	0.02	0.00	0.00	0.78	0.00	0.15
Total (wt%)	100.88	99.98	100.84	96.77	98.41	99.72	100.38	100.33	100.21	96.28	100.01	98.42	99.76	99.66	100.17	96.71	99.89	98.40	100.60	99.84	100.04	96.47	100.24	98.25
No. oxygens	6	12	12	23	3	8	6	12	12	23	3	8	6	12	12	23	3	8	6	12	12	23	3	8
Si	1.98	2.95	3.27	7.05	0.00	2.57	1.95	2.94	2.96	7.08	0.00	2.56	1.93	2.94	2.97	7.06	0.00	2.48	1.93	2.93	2.95	7.27	0.00	2.57
Ti	0.00	0.02	0.00	0.19	0.99	0.00	0.00	0.01	0.01	0.19	1.00	0.00	0.01	0.01	0.00	0.23	1.03	0.00	0.00	0.01	0.00	0.22	0.99	0.00
Al	0.06	1.95	0.00	2.46	0.00	1.41	0.05	1.92	1.92	2.21	0.00	1.41	0.09	1.93	1.94	2.27	0.00	1.47	0.06	1.95	1.95	1.95	0.00	1.39
Cr	0.00	0.00	1.43	0.01	0.00	0.00	0.00	0.00	0.00	0.00	0.00	0.00	0.00	0.00	0.00	0.01	0.00	0.00	0.00	0.00	0.00	0.01	0.00	0.00
Fe^{3+}	0.00	0.11	0.03	0.00	0.02	0.04	0.06	0.17	0.14	0.00	0.01	0.05	0.07	0.18	0.12	0.00	0.00	0.08	0.09	0.17	0.13	0.00	0.02	0.06
Fe^{2+}	0.31	1.46	1.80	2.26	0.94	b.d.l.	0.28	1.48	1.53	2.43	0.94	b.d.l.	0.25	1.41	1.66	2.14	0.93	b.d.l.	0.24	1.45	1.55	2.21	0.93	b.d.l.
Mn^{2+}	0.01	0.09	0.19	0.05	0.03	0.00	0.01	0.11	0.26	0.04	0.03	0.00	0.01	0.08	0.14	0.03	0.03	0.00	0.01	0.11	0.24	0.04	0.03	0.00
Mg	0.67	0.58	0.39	2.27	0.02	0.00	0.64	0.51	0.28	2.22	0.02	0.00	0.67	0.60	0.44	2.46	0.02	0.00	0.66	0.54	0.37	2.51	0.03	0.00
Zn	0.00	0.00	0.00	0.00	0.00	0.00	0.00	0.00	0.00	0.00	0.00	0.00	0.00	0.00	0.00	0.00	0.00	0.00	0.00	0.00	0.00	0.00	0.00	0.00
Ca	0.94	0.84	0.89	2.06	0.00	0.44	0.98	0.85	0.90	2.19	0.00	0.46	0.94	0.84	0.73	2.12	0.00	0.53	0.97	0.84	0.79	2.12	0.00	0.44
Na	0.02	0.01	0.00	0.46	0.00	0.58	0.02	0.00	0.00	0.47	0.00	0.57	0.03	0.00	0.00	0.50	0.00	0.50	0.03	0.00	0.00	0.49	0.00	0.58
K	0.00	0.00	0.00	0.19	0.00	0.01	0.00	0.00	0.00	0.19	0.00	0.01	0.00	0.00	0.00	0.19	0.00	0.01	0.00	0.00	0.00	0.16	0.00	0.01
Total cations	4.00	8.00	8.00	17.00	2.00	5.00	4.00	8.00	8.00	17.00	2.00	5.00	4.00	8.00	8.00	17.00	2.00	5.00	4.00	8.00	8.00	17.00	2.00	5.00
X_{alm}	-	0.49	0.55	-	-	-	-	0.50	0.52	-	-	-	-	0.48	0.56	-	-	-	-	0.49	0.52	-	-	-
X_{py}	-	0.19	0.12	-	-	-	-	0.17	0.09	-	-	-	-	0.21	0.15	-	-	-	-	0.18	0.13	-	-	-
X_{grs}	-	0.23	0.26	-	-	-	-	0.20	0.23	-	-	-	-	0.20	0.19	-	-	-	-	0.20	0.20	-	-	-
X_{sps}	-	0.03	0.06	-	-	-	-	0.04	0.09	-	-	-	-	0.03	0.05	-	-	-	-	0.04	0.08	-	-	-
$X_{Mg(total)}$	0.68	0.27	0.18	0.50	0.02		0.65	0.24	0.14	0.48	0.02		0.67	0.28	0.20	0.53	0.02		0.67	0.25	0.18	0.53	0.03	
X_{Na}	-	-	-	-	-	0.57	-	-	-	-	-	0.55	-	-	-	-	-	0.48	-	-	-	-	-	0.57

APPENDIX E: ADDITIONAL GARNET ELEMENTAL X-RAY MAPS

UBG-4 (Upper Brady Gneiss)

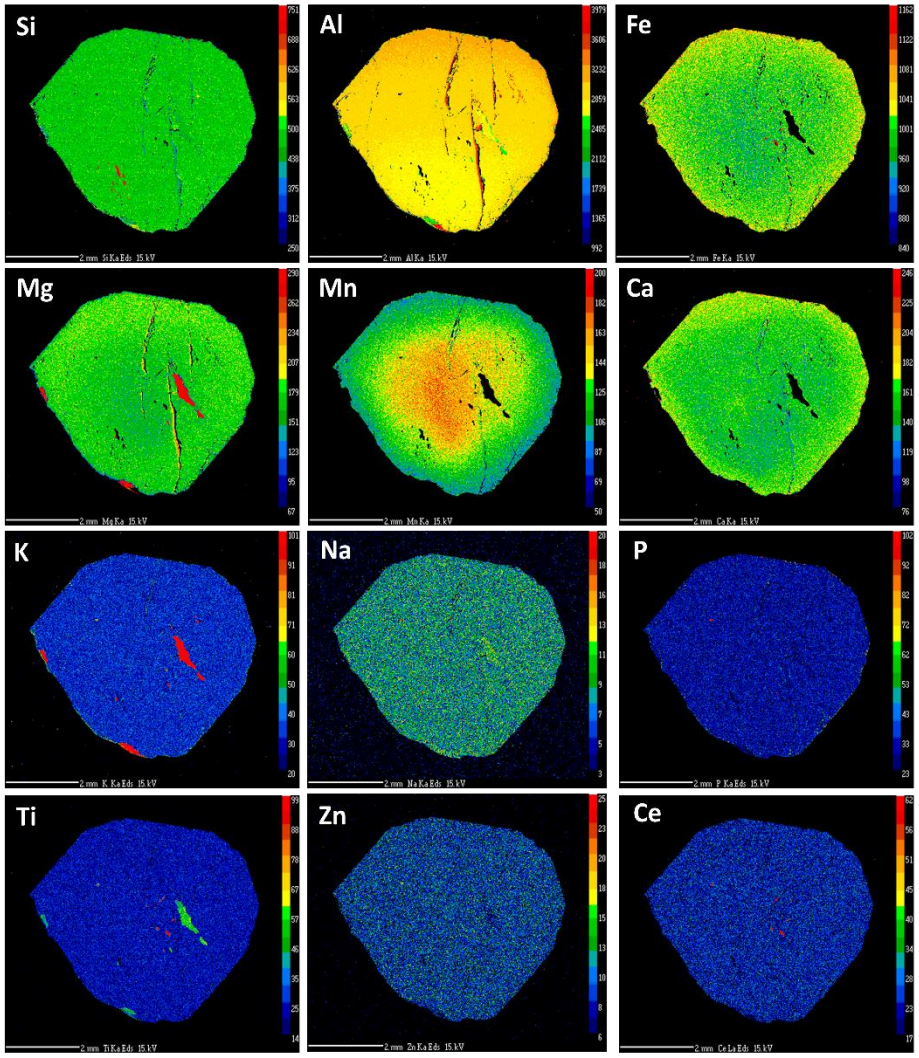

BG-07 (Lower Brady Gneiss)

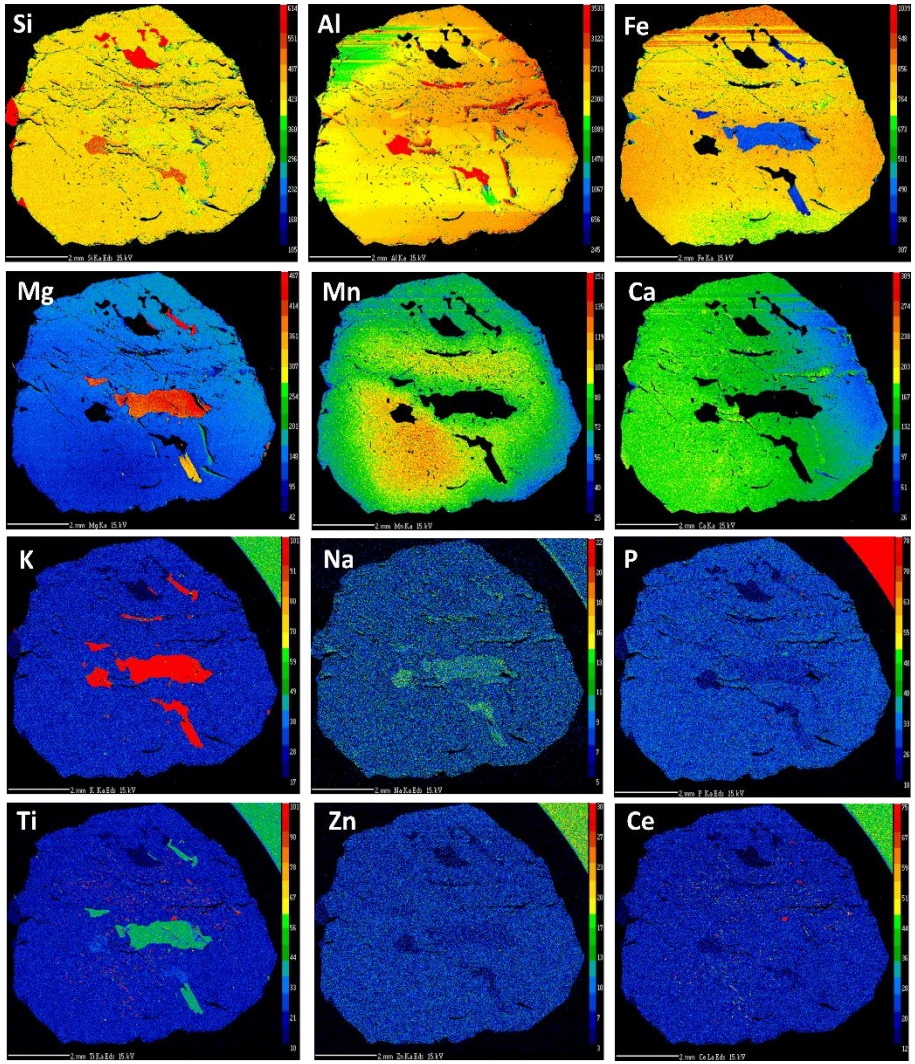

IG-02 (upper Irindina Gneiss)

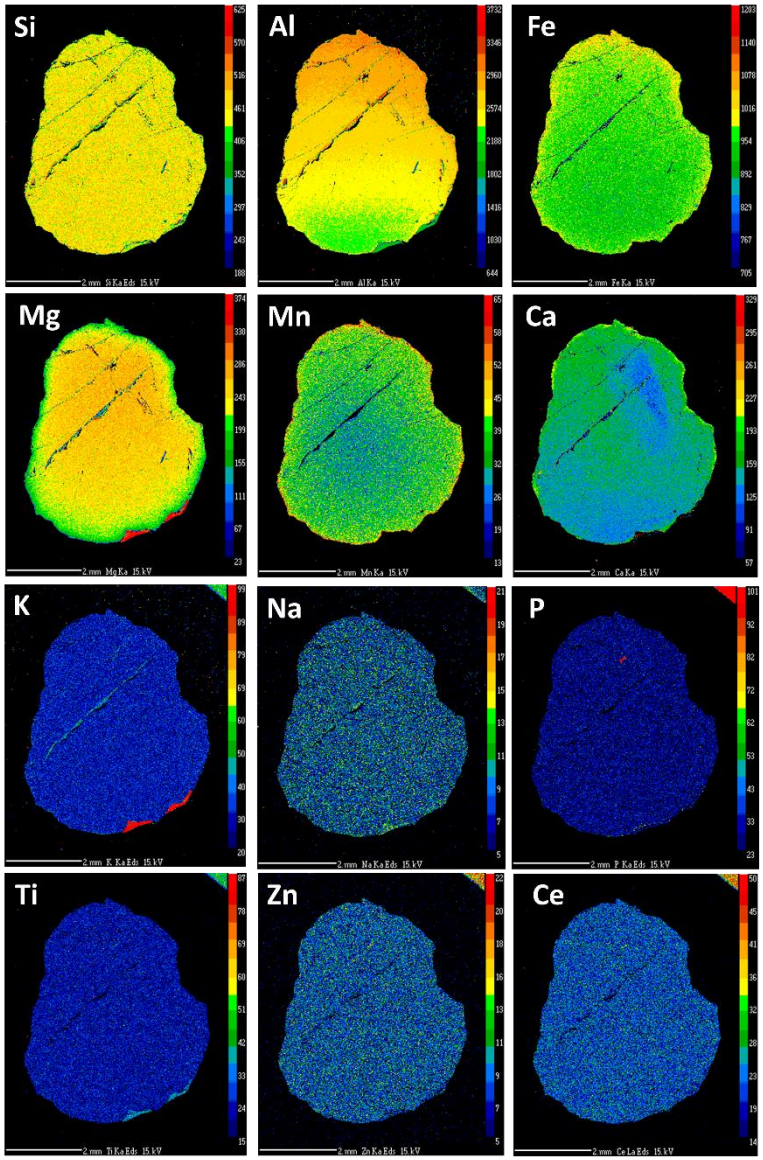

IG-10 (Lower Irindina Gneiss)

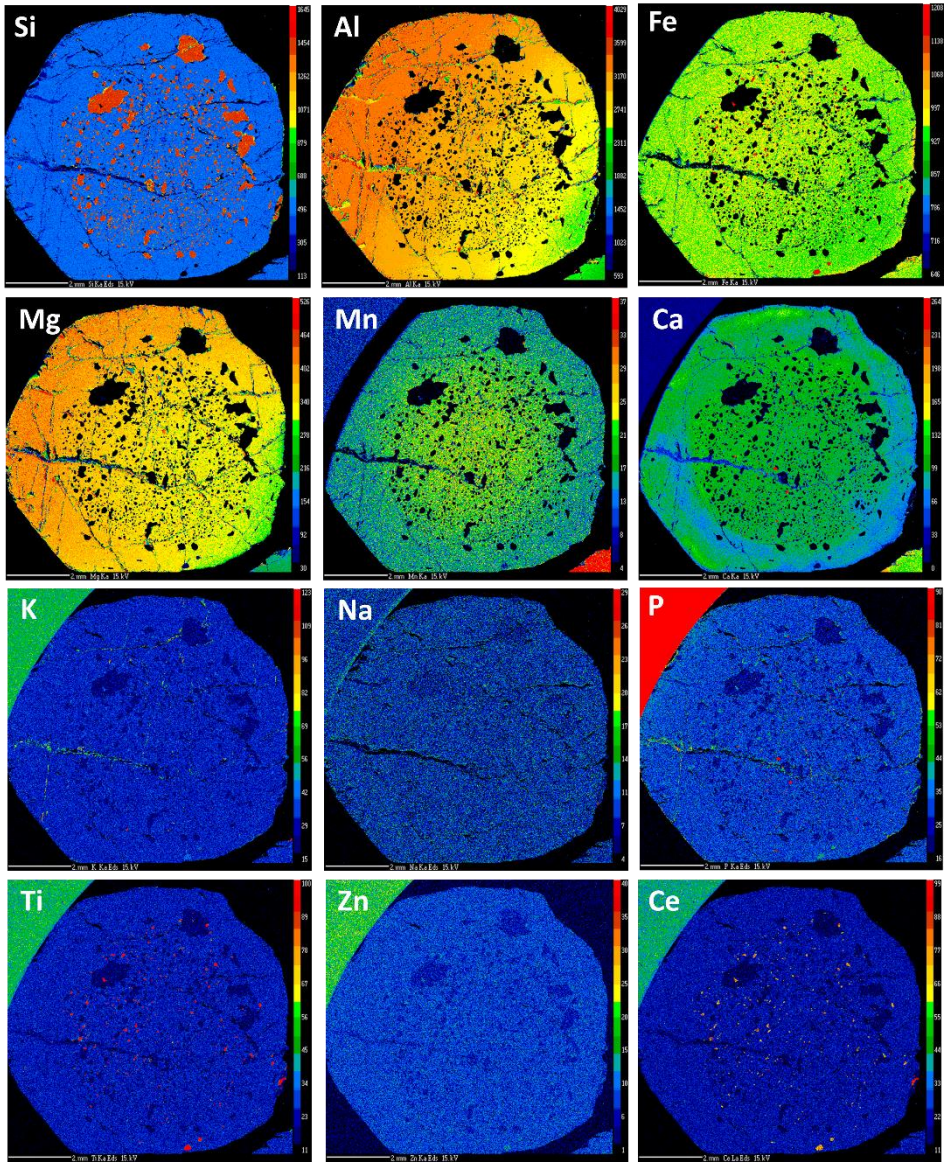

APPENDIX F: LA-ICP-MS MONAZITE U-PB GEOCHRONOLOGY STANDARD ANALYSES

Analysis	207Pb/206Pb	1σ	206Pb/238U	1σ	207Pb/235U	1σ	% Conc.	207Pb/206Pb age (Ma)	1σ	206Pb/238U age (Ma)	1σ	207Pb/235U age (Ma)	1σ	204Pb/206Pb (%)
Standards - session 1														
Madel monazite standard														
STDMADEL01	0.05773	0.00061	0.08508	0.00131	0.67696	0.01041	100	519.3	22.57	526.4	7.79	524.9	6.30	0.02
STDMADEL02	0.05707	0.00060	0.08372	0.00129	0.65860	0.01012	99	493.8	23.33	518.3	7.68	513.8	6.20	0.01
STDMADEL03	0.05740	0.00061	0.08264	0.00128	0.65374	0.01010	100	506.4	23.24	511.9	7.60	510.8	6.20	0.00
STDMADEL04	0.05634	0.00060	0.08410	0.00130	0.65291	0.01015	98	464.8	23.67	520.5	7.75	510.3	6.23	0.01
STDMADEL05	0.05649	0.00061	0.08357	0.00130	0.65070	0.01017	98	471.1	23.82	517.4	7.72	508.9	6.25	0.00
STDMADEL06	0.05645	0.00060	0.08356	0.00130	0.65009	0.01010	98	469.4	23.49	517.3	7.73	508.5	6.22	0.02
STDMADEL07	0.05743	0.00066	0.08404	0.00135	0.66514	0.01105	100	507.8	25.17	520.2	8.00	517.8	6.74	0.02
STDMADEL08	0.05732	0.00063	0.08450	0.00135	0.66755	0.01080	99	503.5	24.09	522.9	8.01	519.2	6.58	0.00
STDMADEL09	0.10867	0.00118	0.09132	0.00146	1.36747	0.02200	155	1777.1	19.72	563.3	8.60	875.1	9.43	0.37
STDMADEL10	0.05647	0.00066	0.08516	0.00137	0.66262	0.01110	98	470.1	25.88	526.8	8.15	516.2	6.78	0.00
STDMADEL11	0.05769	0.00066	0.08176	0.00131	0.64997	0.01076	100	517.7	25.14	506.6	7.82	508.5	6.62	0.00
STDMADEL12	0.05622	0.00063	0.08357	0.00136	0.64773	0.01068	98	460.4	24.78	517.4	8.10	507.1	6.58	0.01
STDMADEL13	0.05612	0.00060	0.08234	0.00135	0.63693	0.01038	98	456.6	23.18	510.1	8.04	500.4	6.44	0.02
STDMADEL14	0.05735	0.00063	0.08128	0.00132	0.64265	0.01055	100	504.7	24.15	503.8	7.89	503.9	6.52	0.02
STDMADEL15	0.05840	0.00068	0.08315	0.00135	0.66944	0.01119	101	544.9	25.20	514.9	8.04	520.4	6.80	0.00
STDMADEL16	0.05621	0.00072	0.08594	0.00141	0.66600	0.01165	98	460.0	28.30	531.5	8.36	518.3	7.10	0.01
STDMADEL17	0.05686	0.00067	0.08468	0.00138	0.66377	0.01120	99	485.3	26.12	524.0	8.19	516.9	6.83	0.00
STDMADEL_18	0.05666	0.00065	0.08109	0.00130	0.63350	0.01049	99	477.5	25.38	502.6	7.77	498.3	6.52	0.00
STDMADEL_19	0.05677	0.00086	0.08369	0.00137	0.65526	0.01250	99	481.8	33.39	518.1	8.16	511.7	7.67	0.00
94-222/Bruna NW monazite standard														
222_01	0.06042	0.00074	0.09370	0.00146	0.78027	0.01289	101	618.6	26.19	577.4	8.61	585.6	7.35	0.00
222_02	0.05990	0.00067	0.09556	0.00149	0.78891	0.01254	100	600.0	24.19	588.3	8.74	590.6	7.12	0.00
222_03	0.05607	0.00066	0.07517	0.00118	0.58085	0.00947	100	454.7	25.62	467.2	7.05	465.0	6.08	0.00
222_04	0.05660	0.00065	0.07161	0.00112	0.55859	0.00898	101	475.1	25.31	445.9	6.72	450.6	5.85	0.00
222_05	0.05608	0.00068	0.07318	0.00116	0.56544	0.00948	100	455.0	26.37	455.3	6.99	455.1	6.15	0.00
222_06	0.05797	0.00073	0.07375	0.00117	0.58910	0.01004	103	528.2	27.81	458.7	7.03	470.3	6.42	0.03
222_07	0.05737	0.00076	0.07323	0.00118	0.57885	0.01018	102	505.2	28.78	455.6	7.08	463.7	6.55	0.02
222_08	0.05630	0.00073	0.07368	0.00119	0.57159	0.01000	100	463.3	28.60	458.3	7.14	459.0	6.46	0.03
222_09	0.05674	0.00074	0.07373	0.00121	0.57667	0.01017	101	480.6	28.72	458.6	7.26	462.3	6.55	0.04
222_10	0.05664	0.00070	0.07423	0.00121	0.57969	0.01001	101	477.0	27.50	461.6	7.28	464.3	6.44	0.00
222_11	0.05713	0.00083	0.07439	0.00122	0.58588	0.01095	101	496.0	31.93	462.5	7.32	468.2	7.01	0.01
Standards - session 2														
Madel monazite standard														
STDMADEL01	0.05667	0.00060	0.08577	0.00144	0.66971	0.01119	98	478.0	23.53	530.4	8.55	520.5	6.80	0.00
STDMADEL02	0.05685	0.00061	0.08440	0.00142	0.66121	0.01105	99	485.2	23.71	522.3	8.42	515.4	6.75	0.02
STDMADEL04	0.05698	0.00061	0.08212	0.00138	0.64479	0.01080	99	490.0	23.87	508.8	8.21	505.3	6.67	0.00
STDMADEL03	0.05729	0.00062	0.08479	0.00142	0.66942	0.01120	99	502.2	23.68	524.7	8.45	520.4	6.81	0.00
STDMADEL05	0.05745	0.00062	0.08164	0.00137	0.64639	0.01086	100	508.6	23.61	505.9	8.17	506.3	6.69	0.02
STDMADEL06	0.05678	0.00060	0.08641	0.00144	0.67650	0.01116	98	482.5	23.30	534.3	8.54	524.7	6.76	0.03
STDMADEL07	0.05717	0.00064	0.08073	0.00135	0.63670	0.01080	100	497.7	24.90	500.5	8.07	500.3	6.70	0.01

Analysis	207Pb/206Pb	1σ	206Pb/238U	1σ	207Pb/235U	1σ	% Conc.	207Pb/206Pb age (Ma)	1σ	206Pb/238U age (Ma)	1σ	207Pb/235U age (Ma)	1σ	204Pb/206Pb (%)
STDMADEL08	0.05751	0.00065	0.08440	0.00142	0.66893	0.01143	100	510.9	24.31	522.3	8.44	520.1	6.95	0.03
STDMADEL09	0.05666	0.00064	0.08416	0.00142	0.65708	0.01125	98	477.6	24.83	520.9	8.43	512.8	6.89	0.01
STDMADEL10	0.05780	0.00068	0.08537	0.00146	0.68002	0.01191	100	522.0	25.88	528.1	8.65	526.8	7.20	0.00
STDMADEL11	0.05684	0.00061	0.08155	0.00136	0.63880	0.01063	99	484.6	23.66	505.4	8.10	501.6	6.59	0.00
STDMADEL12	0.05728	0.00066	0.08271	0.00139	0.65286	0.01122	100	501.9	25.22	512.3	8.30	510.2	6.89	0.00
STDMADEL13	0.05670	0.00067	0.08347	0.00140	0.65229	0.01134	99	479.3	26.27	516.8	8.35	509.9	6.97	0.02
STDMADEL14	0.05683	0.00065	0.08295	0.00137	0.64966	0.01097	99	484.2	25.18	513.7	8.17	508.3	6.75	0.01
STDMADEL15	0.05552	0.00065	0.08360	0.00138	0.63976	0.01089	97	432.8	25.77	517.6	8.21	502.2	6.74	0.01
STDMADEL16	0.05723	0.00062	0.08266	0.00134	0.65202	0.01065	100	499.9	23.91	512.0	8.00	509.7	6.55	0.02
STDMADEL17	0.05699	0.00069	0.08255	0.00128	0.64828	0.01060	99	490.4	26.66	511.3	7.62	507.4	6.53	0.01
STDMADEL18	0.05774	0.00070	0.08815	0.00136	0.70136	0.01145	99	519.6	26.58	544.6	8.06	539.6	6.83	0.00
STDMADEL19	0.05690	0.00069	0.08503	0.00131	0.66675	0.01090	99	487.1	27.02	526.1	7.77	518.7	6.64	0.04
94-222/Bruna NW monazite standard														
222_01	0.05573	0.00060	0.07127	0.00120	0.54734	0.00916	100	441.4	23.24	443.8	7.19	443.3	6.01	0.00
222_02	0.05561	0.00061	0.07261	0.00122	0.55642	0.00939	99	436.6	23.77	451.8	7.32	449.2	6.12	0.02
222_03	0.05657	0.00067	0.07184	0.00120	0.56016	0.00972	101	474.1	26.15	447.3	7.24	451.6	6.33	0.02
222_04	0.05575	0.00064	0.07183	0.00120	0.55194	0.00946	100	442.2	24.69	447.2	7.24	446.3	6.19	0.00
222_05	0.05597	0.00062	0.07058	0.00117	0.54438	0.00914	100	451.0	23.91	439.7	7.07	441.3	6.01	0.01
222_06	0.05613	0.00063	0.07191	0.00119	0.55621	0.00938	100	457.2	24.38	447.6	7.18	449.1	6.12	0.01
222_07	0.05891	0.00089	0.09654	0.00154	0.78392	0.01456	99	563.7	32.72	594.1	9.03	587.7	8.28	0.00
222_08	0.05617	0.00076	0.07041	0.00110	0.54507	0.00947	101	458.6	29.53	438.6	6.65	441.8	6.23	0.00

Rejected analysis

APPENDIX G: SUPPLEMENTARY DATA TABLES – ZIRCON ELEMENT ANALYSES

Grain spot	Inferred age (Ma)	±	SiO_2 (wt%)	Al_2O_3 (wt%)	ZrO_2 (wt%)	CaO (wt%)	Ti (ppm)	Y (ppm)	Hf (ppm)	Yb (ppm)
Upper Brady Gneiss										
UBG 6	2169	24	32.92	0.0160	65.79	b.d.l.	b.d.l.	695.31	12471.21	b.d.l.
UBG 3	863	13	32.01	b.d.l.	65.72	b.d.l.	b.d.l.	4043.50	11211.11	771.06
UBG 7	535	15	32.70	b.d.l.	64.93	b.d.l.	b.d.l.	1361.48	12872.30	485.65
UBG 2	1814	21	31.81	0.0158	64.92	b.d.l.	b.d.l.	2070.97	13377.70	b.d.l.
UBG 11	1238	31	32.68	0.0206	65.81	b.d.l.	b.d.l.	909.49	14147.66	583.13
UBG 13	584	7	32.62	0.0326	66.31	0.0198	b.d.l.	1730.79	12645.04	653.38
UBG 17	788	14	33.06	0.0178	66.30	0.0131	b.d.l.	1512.67	9543.14	b.d.l.
UBG 18	499	6	31.11	b.d.l.	63.16	0.0198	b.d.l.	2407.99	10833.76	555.02
UBG 24	670	11	32.98	0.0203	65.53	b.d.l.	b.d.l.	1249.67	17029.09	488.28
UBG 20	1787	14	32.62	0.0217	65.35	b.d.l.	b.d.l.	1699.30	16340.53	b.d.l.
UBG 26	1769	32	31.01	0.0190	63.05	b.d.l.	b.d.l.	4649.83	10347.03	1017.83
UBG 25	2170	24	32.71	0.0327	65.38	b.d.l.	b.d.l.	449.63	15297.52	b.d.l.
UBG 28	1065	20	32.76	b.d.l.	65.92	b.d.l.	b.d.l.	1315.02	15054.15	b.d.l.
UBG 27	1065	13	32.60	0.0183	64.86	b.d.l.	b.d.l.	684.29	15584.98	b.d.l.
UBG 29	707	13	32.86	0.0175	65.99	b.d.l.	b.d.l.	656.72	13173.34	b.d.l.
UBG 32	693	44	32.42	0.0291	65.49	0.0123	b.d.l.	511.05	13759.29	b.d.l.
UBG 36	1862	16	32.48	0.0209	64.59	b.d.l.	b.d.l.	1133.91	14432.58	566.44
UBG 37	895	11	32.12	b.d.l.	64.32	b.d.l.	b.d.l.	773.27	14455.48	b.d.l.
UBG 33	1232	30	32.66	0.0323	65.40	b.d.l.	b.d.l.	974.06	12524.63	b.d.l.
UBG 34	1937	48	32.80	0.0270	65.73	b.d.l.	b.d.l.	931.54	17632.00	520.77
UBG 35	1585	53	31.43	0.0293	63.60	b.d.l.	b.d.l.	682.71	12478.84	b.d.l.
UBG 39	599	16	32.73	0.0170	65.77	b.d.l.	b.d.l.	922.09	14296.91	b.d.l.
UBG 46	980	12	32.62	b.d.l.	65.00	0.0122	b.d.l.	4801.02	13432.82	1521.92
UBG 45	1043	22	31.05	0.0157	63.34	b.d.l.	b.d.l.	1315.81	14000.11	b.d.l.
UBG 41	899	22	32.33	0.0165	65.77	b.d.l.	b.d.l.	521.29	16639.02	b.d.l.
UBG 42	680	13	31.09	0.0234	63.15	b.d.l.	b.d.l.	2285.94	11995.49	766.67
UBG 43	1189	32	32.99	b.d.l.	65.97	b.d.l.	b.d.l.	823.66	13632.94	b.d.l.
UBG 48	1665	41	32.71	BDL	65.73	b.d.l.	b.d.l.	3573.40	11339.16	707.83
UBG 51	1861	35	32.39	b.d.l.	64.90	b.d.l.	b.d.l.	796.89	11925.11	b.d.l.
UBG 52	1837	16	32.85	0.0297	65.08	b.d.l.	b.d.l.	3826.17	12444.07	855.37
UBG 53	853	19	32.67	b.d.l.	66.25	b.d.l.	b.d.l.	3886.02	7300.24	879.96
UBG 54	651	12	32.88	BDL	66.47	b.d.l.	b.d.l.	1188.25	12815.49	612.98
UBG 55	683	12	32.12	b.d.l.	65.13	b.d.l.	b.d.l.	720.51	14385.10	b.d.l.
UBG 57	583	12	32.43	b.d.l.	66.39	b.d.l.	b.d.l.	1559.13	13886.48	b.d.l.
UBG 56	589	8	33.16	0.0196	66.35	b.d.l.	b.d.l.	311.04	15357.73	b.d.l.
Tomahawk Fm.										
T 4	587	5	31.53	b.d.l.	63.82	b.d.l.	b.d.l.	511.84	15142.34	b.d.l.
T 2	1206	19	32.32	b.d.l.	65.61	b.d.l.	b.d.l.	554.36	13912.77	b.d.l.
T 5	596	11	32.64	0.0187	66.15	b.d.l.	b.d.l.	549.63	11797.92	b.d.l.
T 6	2694	23	31.17	b.d.l.	62.98	b.d.l.	b.d.l.	1061.47	14580.98	b.d.l.
T 7	1309	66	31.17	b.d.l.	63.85	0.0138	b.d.l.	318.13	12606.89	b.d.l.
T 11	2041	34	32.72	b.d.l.	66.29	b.d.l.	b.d.l.	626.80	11818.27	b.d.l.
T 10	1559	32	31.24	b.d.l.	64.64	b.d.l.	b.d.l.	641.76	13788.97	b.d.l.
T 13	2693	34	32.82	b.d.l.	66.42	b.d.l.	b.d.l.	945.72	12523.78	b.d.l.
T 14	555	14	32.72	b.d.l.	66.40	b.d.l.	b.d.l.	b.d.l.	12428.81	b.d.l.
T 19	1776	35	32.53	0.0158	65.84	b.d.l.	b.d.l.	983.51	16170.09	b.d.l.
T 9	1115	38	32.57	0.0183	66.03	b.d.l.	b.d.l.	747.28	15747.80	b.d.l.
T 18	624	14	31.38	0.0442	63.17	b.d.l.	b.d.l.	1124.46	11323.90	b.d.l.
T 17	1723	21	31.66	b.d.l.	65.77	b.d.l.	b.d.l.	1109.50	15250.88	b.d.l.
T 21	520	7	32.40	0.0226	66.00	b.d.l.	b.d.l.	b.d.l.	10598.87	b.d.l.
T 22	3282	7	31.04	b.d.l.	63.54	b.d.l.	b.d.l.	2512.72	14597.09	835.17
T 23	565	8	31.62	b.d.l.	65.69	b.d.l.	b.d.l.	339.39	14525.01	b.d.l.
T 24	1720	33	32.49	b.d.l.	66.20	b.d.l.	b.d.l.	1457.55	13023.24	538.34
T 39	1320	28	31.84	b.d.l.	65.07	b.d.l.	b.d.l.	745.71	14540.28	b.d.l.
T 33	981	28	32.11	0.0177	65.90	b.d.l.	b.d.l.	785.87	14134.94	b.d.l.
T 28	1016	14	31.08	b.d.l.	64.04	b.d.l.	b.d.l.	b.d.l.	14468.20	b.d.l.
T 29	1181	31	32.47	0.0201	65.90	b.d.l.	b.d.l.	433.88	14742.09	b.d.l.
T 36	1162	40	32.15	b.d.l.	65.80	b.d.l.	b.d.l.	849.65	13165.70	b.d.l.
T 40	543	6	32.65	b.d.l.	66.60	b.d.l.	b.d.l.	b.d.l.	10353.81	b.d.l.
T 42	1082	14	31.14	0.0254	63.49	b.d.l.	b.d.l.	3806.48	13114.82	829.90
T 43	2102	41	32.50	b.d.l.	67.00	b.d.l.	b.d.l.	801.61	11614.75	b.d.l.
T 44	646	15	31.61	b.d.l.	64.34	b.d.l.	b.d.l.	555.93	12923.18	b.d.l.
T 46	1951	23	31.42	0.0331	64.54	b.d.l.	b.d.l.	666.17	12879.09	b.d.l.
T 51	628	14	31.15	0.0208	63.84	0.0134	b.d.l.	826.02	11933.59	b.d.l.
T 50	1412	49	31.12	b.d.l.	64.10	b.d.l.	b.d.l.	455.93	13175.88	b.d.l.
T 52	643	15	31.00	b.d.l.	63.70	b.d.l.	b.d.l.	630.74	13190.29	b.d.l.
T 58	1061	11	32.20	b.d.l.	65.08	b.d.l.	b.d.l.	1121.31	12884.17	b.d.l.
T 57	532	14	32.54	b.d.l.	66.40	b.d.l.	b.d.l.	b.d.l.	13292.90	b.d.l.
T 56	1040	12	32.20	0.0166	66.28	b.d.l.	b.d.l.	1059.89	12031.96	551.51
T 61	874	15	32.75	0.0172	66.33	b.d.l.	b.d.l.	512.62	12943.53	b.d.l.
T 65	608	13	32.04	b.d.l.	64.85	b.d.l.	b.d.l.	1232.34	12685.75	b.d.l.
T 67	844	94	31.39	0.0196	63.76	b.d.l.	b.d.l.	344.11	13102.10	b.d.l.
T 68	1860	23	31.34	0.0202	63.82	b.d.l.	b.d.l.	938.63	13311.56	b.d.l.
T 64	3201	39	32.07	b.d.l.	65.80	b.d.l.	b.d.l.	b.d.l.	12042.98	b.d.l.

Grain spot	Inferred age (Ma)	±	SiO_2 (wt%)	Al_2O_3 (wt%)	ZrO_2 (wt%)	CaO (wt%)	Ti (ppm)	Y (ppm)	Hf (ppm)	Yb (ppm)
Pacoota Sandstone										
P 6	1079	30	32.50	b.d.l.	65.52	b.d.l.	b.d.l.	723.66	13852.57	b.d.l.
P 9	3420	12	32.50	b.d.l.	66.08	b.d.l.	b.d.l.	1299.28	10276.64	600.69
P 11	1183	37	32.80	b.d.l.	65.39	b.d.l.	b.d.l.	744.92	13671.10	500.57
P 10	553	13	32.53	0.0350	64.95	b.d.l.	b.d.l.	b.d.l.	16800.14	b.d.l.
P 12	3345	8	31.30	0.0179	63.44	b.d.l.	b.d.l.	1621.34	12048.92	b.d.l.
P 13	588	13	32.42	0.0172	65.77	b.d.l.	b.d.l.	296.86	14956.63	b.d.l.
P 14	556	9	32.92	b.d.l.	65.77	b.d.l.	b.d.l.	b.d.l.	16857.80	b.d.l.
P 18	2712	30	33.04	b.d.l.	66.00	b.d.l.	b.d.l.	860.67	12571.27	b.d.l.
P 23	3279	15	31.98	0.0181	64.69	b.d.l.	b.d.l.	1966.24	16231.14	569.95
P 24	584	18	31.24	b.d.l.	63.63	b.d.l.	b.d.l.	b.d.l.	13978.91	b.d.l.
P 31	1064	133	32.32	0.0195	66.50	b.d.l.	b.d.l.	542.55	10547.15	b.d.l.
P 22	2000	30	32.91	0.0171	65.89	b.d.l.	b.d.l.	1094.54	12349.95	b.d.l.
P 25	3325	20	32.73	0.0157	66.52	b.d.l.	b.d.l.	1233.13	11830.99	466.32
P 28	1482	69	32.23	0.0218	65.29	b.d.l.	b.d.l.	729.96	14836.22	b.d.l.
P 33	2702	46	31.09	0.0212	63.63	b.d.l.	b.d.l.	431.52	13465.89	b.d.l.
P 35	1154	27	32.25	b.d.l.	65.40	b.d.l.	b.d.l.	354.35	15246.64	b.d.l.
P 34	2584	16	31.73	0.0509	64.30	0.0165	b.d.l.	3212.76	11178.89	816.73
P 39	1491	73	31.00	b.d.l.	63.69	b.d.l.	b.d.l.	293.72	13723.67	b.d.l.
P 38	3240	31	31.31	0.0191	63.72	b.d.l.	b.d.l.	468.53	11810.63	b.d.l.
P 40	1376	55	30.99	b.d.l.	63.78	b.d.l.	b.d.l.	512.62	12918.09	b.d.l.
P 42	2169	70	31.43	b.d.l.	63.92	b.d.l.	b.d.l.	729.96	11635.10	b.d.l.
P 44	834	80	32.83	b.d.l.	66.18	b.d.l.	b.d.l.	487.43	12600.10	b.d.l.
P 48	2727	30	32.23	b.d.l.	65.67	b.d.l.	b.d.l.	946.50	13193.69	b.d.l.
P 49	1194	27	32.52	b.d.l.	66.35	b.d.l.	b.d.l.	744.92	14134.09	b.d.l.
P 46	1137	28	32.66	b.d.l.	65.08	b.d.l.	b.d.l.	609.48	14746.33	b.d.l.
P 55	566	7	32.36	0.0450	65.97	b.d.l.	b.d.l.	273.24	16562.70	b.d.l.
P 53	685	25	32.59	b.d.l.	65.89	b.d.l.	b.d.l.	1492.20	11712.27	b.d.l.
P 52	1201	50	31.56	b.d.l.	64.20	BDL	b.d.l.	2314.29	13631.24	734.18
P 51	906	65	31.78	b.d.l.	65.10	BDL	b.d.l.	2670.21	13117.37	610.35
P 56	1073	44	31.36	b.d.l.	63.22	b.d.l.	b.d.l.	629.16	13413.31	b.d.l.
P 60	662	12	31.37	b.d.l.	64.67	b.d.l.	b.d.l.	1252.82	10150.29	b.d.l.
P 61	1118	24	32.41	b.d.l.	65.36	b.d.l.	b.d.l.	536.25	14988.01	b.d.l.
P 58	552	12	32.45	0.0186	65.46	b.d.l.	b.d.l.	694.52	17013.83	b.d.l.
P 57	1043	39	32.34	0.0170	65.99	b.d.l.	b.d.l.	1062.26	10469.13	b.d.l.
P 62	540	7	31.16	0.0321	64.40	b.d.l.	b.d.l.	602.39	15915.70	b.d.l.
P 63	1831	31	31.40	0.0172	64.00	0.0372	b.d.l.	1993.80	12412.70	759.64
P 64	2744	22	31.03	b.d.l.	63.31	b.d.l.	b.d.l.	2107.98	11182.28	b.d.l.
P 65	532	9	31.72	0.0321	64.35	b.d.l.	b.d.l.	b.d.l.	15641.80	b.d.l.
P 66	2704	11	31.42	b.d.l.	64.41	0.0141	b.d.l.	1204.00	14050.99	505.84
P 67	2705	35	31.50	b.d.l.	64.09	b.d.l.	b.d.l.	956.74	10403.84	b.d.l.
P 68	648	16	31.24	0.0282	63.00	0.0149	b.d.l.	2619.03	11280.65	667.43
P 70	989	16	31.24	b.d.l.	64.35	b.d.l.	b.d.l.	603.97	11396.82	b.d.l.
P 71	1103	27	32.61	b.d.l.	65.97	b.d.l.	b.d.l.	1805.60	11364.60	581.37
P 77	603	9	32.16	0.0215	65.52	b.d.l.	b.d.l.	552.00	14206.17	b.d.l.
P 73	1130	108	32.70	0.0178	66.56	b.d.l.	b.d.l.	1453.61	12426.27	b.d.l.
P 74	1172	20	32.71	b.d.l.	65.90	b.d.l.	b.d.l.	595.30	17209.71	b.d.l.
Crossing Bore Schist										
CBS 3	1141	35	32.12	b.d.l.	66.14	b.d.l.	b.d.l.	858.31	14000.96	b.d.l.
CBS 1	1207	60	32.87	b.d.l.	65.93	b.d.l.	b.d.l.	523.65	13835.61	b.d.l.
CBS 5	1209	35	32.42	0.0268	65.67	b.d.l.	b.d.l.	522.86	15326.35	b.d.l.
CBS 8	2037	20	31.53	b.d.l.	63.81	b.d.l.	b.d.l.	317.34	12940.99	b.d.l.
CBS 10	1528	23	31.04	0.0181	63.92	b.d.l.	b.d.l.	1164.62	14610.66	505.84
CBS 13	634	8	31.88	b.d.l.	63.37	b.d.l.	b.d.l.	629.16	14366.44	b.d.l.
CBS 14	1184	19	32.09	0.0269	66.01	b.d.l.	b.d.l.	878.00	15043.97	b.d.l.
CBS 17	1111	25	32.53	b.d.l.	65.45	b.d.l.	b.d.l.	603.18	15030.41	b.d.l.
CBS 18	1707	28	32.67	b.d.l.	64.79	b.d.l.	b.d.l.	546.48	15282.26	b.d.l.
CBS 19	1160	29	32.70	b.d.l.	65.47	b.d.l.	b.d.l.	385.06	14440.21	b.d.l.
CBS 24	1154	23	32.11	b.d.l.	64.96	b.d.l.	b.d.l.	3599.39	10938.07	638.45
CBS 25	1219	26	31.83	b.d.l.	63.38	b.d.l.	b.d.l.	639.40	15000.73	b.d.l.
CBS 31	1252	18	32.48	0.0161	65.46	b.d.l.	b.d.l.	403.96	16187.90	b.d.l.
CBS 29	1213	45	31.34	b.d.l.	64.22	b.d.l.	b.d.l.	442.54	14826.04	b.d.l.
CBS 32	1263	22	31.88	0.0235	63.62	b.d.l.	b.d.l.	567.74	13970.43	b.d.l.
CBS 34	1163	24	31.63	0.0265	63.41	b.d.l.	b.d.l.	872.48	13683.82	503.21
CBS 35	1060	19	31.57	0.0165	64.09	b.d.l.	b.d.l.	1655.20	12451.71	b.d.l.
CBS 36	1637	135	31.00	0.0182	63.94	b.d.l.	b.d.l.	745.71	13745.72	b.d.l.
CBS 37	1125	19	32.08	0.0219	63.43	b.d.l.	b.d.l.	1015.01	14927.80	b.d.l.
CBS 38	2686	18	30.86	b.d.l.	61.89	b.d.l.	b.d.l.	409.47	13225.91	b.d.l.
CBS 39	1211	15	31.33	b.d.l.	63.19	BDL	b.d.l.	1039.42	14497.03	483.01
CBS 43	1212	41	31.67	0.0157	63.97	BDL	b.d.l.	819.73	15368.75	b.d.l.
CBS 44	1103	13	31.35	0.0167	64.13	BDL	b.d.l.	775.63	13177.58	486.52
CBS 46	1763	40	31.85	b.d.l.	65.12	b.d.l.	b.d.l.	1895.37	12567.03	495.31
CBS 45	1201	26	31.90	0.0261	64.91	b.d.l.	b.d.l.	535.46	14850.64	b.d.l.
CBS 48	1504	32	32.15	b.d.l.	65.34	b.d.l.	b.d.l.	2356.81	13842.39	1066.14
CBS 49	1159	29	31.46	0.0229	63.76	0.0146	b.d.l.	677.99	15666.39	b.d.l.
CBS 50	1094	18	32.08	b.d.l.	64.90	b.d.l.	b.d.l.	1515.82	11757.21	b.d.l.
CBS 52	1079	39	31.76	0.0225	64.44	b.d.l.	b.d.l.	1183.52	13922.10	585.76
CBS 51	1130	29	32.83	0.0246	65.09	b.d.l.	b.d.l.	b.d.l.	18129.77	b.d.l.
CBS 55	1185	26	32.99	b.d.l.	65.63	b.d.l.	b.d.l.	811.85	14577.59	b.d.l.
CBS 54	1179	11	32.75	0.0176	65.69	b.d.l.	b.d.l.	1815.84	14245.18	586.64
CBS 57	1084	56	31.87	b.d.l.	65.39	0.0135	b.d.l.	1311.09	12287.20	b.d.l.
CBS 56	1433	25	32.71	0.0173	65.93	b.d.l.	b.d.l.	1170.92	14865.05	b.d.l.
CBS 58	1129	12	31.51	0.0182	64.69	b.d.l.	b.d.l.	996.90	13977.22	b.d.l.

Grain spot	Inferred age (Ma)	±	SiO_2 (wt%)	Al_2O_3 (wt%)	ZrO_2 (wt%)	CaO (wt%)	Ti (ppm)	Y (ppm)	Hf (ppm)	Yb (ppm)
CBS 59	1169	12	31.65	b.d.l.	64.56	b.d.l.	b.d.l.	302.38	16862.04	b.d.l.
CBS 61	1119	11	31.67	b.d.l.	64.54	b.d.l.	b.d.l.	1214.23	14179.04	b.d.l.
CBS 62	1095	41	32.63	0.0184	65.20	b.d.l.	b.d.l.	492.15	15522.23	b.d.l.
CBS 63	1181	20	31.85	0.0226	64.36	b.d.l.	b.d.l.	1266.99	14890.49	642.84
CBS 66	1162	27	31.70	b.d.l.	64.66	b.d.l.	b.d.l.	448.84	13894.96	b.d.l.
CBS 65	724	23	32.70	0.0899	62.57	0.0151	b.d.l.	1115.80	10569.20	b.d.l.
Arumbera Sandstone										
AS_1	1168	25	30.41	0.0252	64.44	b.d.l.	b.d.l.	1152.81	12171.87	b.d.l.
AS_2	1199	34	31.39	0.0231	66.16	b.d.l.	b.d.l.	459.08	12647.59	b.d.l.
AS_3	1507	18	31.35	0.0281	66.37	0.0127	b.d.l.	344.11	10899.91	b.d.l.
AS_4	1161	12	31.46	0.0237	66.06	b.d.l.	b.d.l.	511.05	16685.66	b.d.l.
AS_5	605	14	31.89	b.d.l.	66.01	b.d.l.	b.d.l.	3078.10	11474.84	504.97
AS_6	1592	18	31.26	0.0303	66.33	b.d.l.	b.d.l.	599.24	11638.50	b.d.l.
AS_7	996	28	30.72	0.0244	66.43	b.d.l.	b.d.l.	413.41	10718.44	b.d.l.
AS_8	1188	19	31.33	0.0246	65.63	b.d.l.	b.d.l.	681.14	12834.99	b.d.l.
AS_9	1122	14	31.49	0.0323	65.98	b.d.l.	b.d.l.	2172.55	14018.77	659.53
AS_10	1233	22	31.48	0.0303	66.36	b.d.l.	b.d.l.	1246.52	11912.39	b.d.l.
AS_11	1156	32	31.73	0.0157	66.48	b.d.l.	b.d.l.	552.78	12768.00	b.d.l.
AS_12	1217	25	31.14	0.0159	65.45	b.d.l.	b.d.l.	429.94	16213.34	b.d.l.
AS_13	1170	17	31.16	b.d.l.	65.83	b.d.l.	b.d.l.	1142.58	12527.18	633.18
AS_14	1160	24	30.81	0.0339	65.94	b.d.l.	b.d.l.	1289.83	12367.76	530.43
AS_15	1563	13	30.89	0.0342	65.77	b.d.l.	b.d.l.	1033.12	11901.37	562.93
AS_16	1154	29	30.85	0.0171	66.00	b.d.l.	b.d.l.	596.88	12042.98	b.d.l.
AS_17	1189	24	30.87	0.0290	65.81	b.d.l.	b.d.l.	826.81	11881.86	b.d.l.
AS_18	1797	13	30.63	0.0250	65.99	b.d.l.	b.d.l.	1311.88	11147.52	b.d.l.
AS_19	1227	16	30.74	0.0213	65.89	b.d.l.	b.d.l.	552.78	13677.03	b.d.l.
AS_20	939	39	30.88	0.0175	66.30	b.d.l.	b.d.l.	621.29	12293.98	b.d.l.
AS_21	1184	16	31.61	0.0172	66.17	b.d.l.	b.d.l.	511.84	12751.89	b.d.l.
AS_22	1159	14	31.85	0.0253	65.92	b.d.l.	b.d.l.	775.63	13344.63	b.d.l.
AS_23	1736	10	31.54	0.0182	65.86	b.d.l.	b.d.l.	1213.45	15509.51	662.16
AS_24	1139	21	32.00	b.d.l.	65.37	b.d.l.	b.d.l.	1194.55	12225.30	b.d.l.
AS_25	1199	30	31.05	0.0206	65.83	b.d.l.	b.d.l.	889.02	12639.11	b.d.l.
AS_26	1100	14	31.33	b.d.l.	65.88	b.d.l.	b.d.l.	749.64	10763.38	b.d.l.
AS_27	1141	21	30.54	0.0211	64.64	b.d.l.	b.d.l.	720.51	12125.23	b.d.l.
AS_28	1569	17	31.79	0.0187	65.57	b.d.l.	b.d.l.	671.69	13727.91	b.d.l.
AS_29	1035	18	30.78	0.0276	63.96	b.d.l.	b.d.l.	949.65	12200.70	b.d.l.
AS_30	951	26	31.28	0.0155	66.40	b.d.l.	b.d.l.	499.24	10861.75	b.d.l.
AS_31	2500	6	31.22	b.d.l.	66.92	b.d.l.	b.d.l.	411.83	13067.34	b.d.l.
AS_32	1108	18	30.31	b.d.l.	64.92	0.0309	b.d.l.	1161.47	11526.56	b.d.l.
AS_33	1790	14	30.05	0.0276	65.18	b.d.l.	b.d.l.	2100.89	11364.60	502.33
AS_34	1363	18	30.47	0.0187	65.27	b.d.l.	b.d.l.	1259.12	14617.44	606.84
AS_35	1566	15	31.95	b.d.l.	66.23	b.d.l.	b.d.l.	696.10	12344.86	b.d.l.
AS_36	1190	20	32.13	b.d.l.	66.35	b.d.l.	b.d.l.	1474.88	12634.02	b.d.l.
AS_37	1101	26	30.48	b.d.l.	65.71	BDL	b.d.l.	1115.02	11889.50	598.05
AS_38	1241	33	31.37	b.d.l.	65.64	b.d.l.	b.d.l.	1768.59	11458.72	b.d.l.
AS_39	1651	40	31.21	b.d.l.	65.60	0.0158	b.d.l.	623.65	9494.81	b.d.l.
AS_40	1106	41	31.16	0.0182	66.06	b.d.l.	b.d.l.	858.31	11487.56	b.d.l.
AS_41	1200	27	32.53	b.d.l.	65.68	b.d.l.	b.d.l.	1009.50	12541.59	b.d.l.
AS_42	1157	22	32.18	b.d.l.	66.13	b.d.l.	b.d.l.	1452.83	13050.38	b.d.l.
AS_43	1785	12	31.93	0.0231	65.89	b.d.l.	b.d.l.	1891.43	13387.03	656.89
AS_44	1266	42	32.72	0.0234	66.33	b.d.l.	89.33	300.01	12614.52	b.d.l.
AS_45	1201	37	32.15	0.0649	64.82	b.d.l.	b.d.l.	803.19	11315.42	b.d.l.
AS_46	1106	29	30.56	b.d.l.	66.56	b.d.l.	b.d.l.	1007.14	10651.45	b.d.l.
AS_47	1188	10	31.98	0.0168	66.37	b.d.l.	b.d.l.	359.07	14295.21	b.d.l.
AS_48	1883	20	31.21	b.d.l.	65.99	b.d.l.	b.d.l.	1080.37	11752.12	b.d.l.
AS_49	1182	14	31.64	b.d.l.	65.51	b.d.l.	b.d.l.	1807.96	14191.76	b.d.l.
AS_50	1008	22	30.99	b.d.l.	66.20	b.d.l.	b.d.l.	540.97	10058.71	b.d.l.
AS_51	1601	18	31.36	0.0156	66.14	b.d.l.	b.d.l.	515.77	14515.68	b.d.l.
AS_52	1042	28	31.39	b.d.l.	64.80	b.d.l.	b.d.l.	572.47	14237.55	b.d.l.
AS_53	1775	11	31.13	0.0202	65.42	b.d.l.	b.d.l.	684.29	13205.56	b.d.l.
AS_54	2496	12	31.59	0.0210	66.58	b.d.l.	b.d.l.	332.30	11526.56	b.d.l.
AS_55	1301	79	31.09	b.d.l.	65.36	b.d.l.	b.d.l.	334.66	11828.44	b.d.l.
AS_56	1729	11	31.97	0.0257	66.08	b.d.l.	b.d.l.	853.58	10765.93	b.d.l.
AS_57	1002	27	32.06	b.d.l.	65.60	b.d.l.	b.d.l.	1448.10	13109.74	641.96
AS_58	1182	26	32.03	0.0378	65.70	b.d.l.	b.d.l.	482.70	14547.06	490.91
AS_59	1093	32	31.68	0.0252	65.16	b.d.l.	b.d.l.	850.44	12088.77	b.d.l.
AS_60	1673	18	31.76	0.0218	65.91	b.d.l.	b.d.l.	1027.61	11215.35	b.d.l.
AS_61	1499	10	32.09	b.d.l.	65.60	b.d.l.	b.d.l.	843.35	13333.60	b.d.l.
AS_62	1193	28	31.61	b.d.l.	65.03	b.d.l.	b.d.l.	1074.86	11568.11	b.d.l.
Lower Stanovos Gneiss										
LSG_1	1181	14	32.41	0.0227	66.27	b.d.l.	b.d.l.	1423.69	10668.41	572.59
LSG_2	1786	27	31.79	0.0224	65.62	b.d.l.	b.d.l.	729.96	13030.03	502.33
LSG_3	1535	37	32.00	0.0223	65.35	b.d.l.	b.d.l.	1271.72	13252.20	b.d.l.
LSG_4	1241	6	31.76	0.0214	65.64	b.d.l.	b.d.l.	1595.35	12214.27	b.d.l.
LSG_5	1276	16	31.82	0.0244	65.71	b.d.l.	b.d.l.	3000.93	10658.23	939.68
LSG_6	1497	32	30.18	0.0371	64.41	b.d.l.	b.d.l.	1963.88	10302.08	510.23
LSG_8	1753	22	31.21	0.0218	66.41	b.d.l.	b.d.l.	1349.67	10707.42	b.d.l.
LSG_11	1041	11	30.59	0.0256	65.82	b.d.l.	b.d.l.	984.30	15781.71	b.d.l.
LSG_12	1573	38	30.42	0.0180	65.33	b.d.l.	b.d.l.	1287.46	10859.20	b.d.l.
LSG_13	1393	30	30.25	b.d.l.	66.02	b.d.l.	b.d.l.	998.47	11139.88	b.d.l.
LSG_14	1545	25	30.52	0.0172	65.75	b.d.l.	b.d.l.	1504.01	13231.85	548.00
LSG_15	1842	14	31.82	0.0185	65.77	b.d.l.	b.d.l.	1811.90	13007.13	b.d.l.

Grain spot	Inferred age (Ma)	±	SiO_2 (wt%)	Al_2O_3 (wt%)	ZrO_2 (wt%)	CaO (wt%)	Ti (ppm)	Y (ppm)	Hf (ppm)	Yb (ppm)
LSG_16	2648	10	31.89	0.0273	65.64	b.d.l.	b.d.l.	1712.68	11116.14	b.d.l.
LSG_17	1441	58	31.21	b.d.l.	65.08	b.d.l.	b.d.l.	1320.54	10380.94	b.d.l.
LSG_18	1356	36	31.22	0.0241	64.74	b.d.l.	b.d.l.	2511.15	7810.72	737.69
LSG_20	1583	40	31.20	0.0291	64.86	b.d.l.	b.d.l.	1338.65	12172.72	b.d.l.
LSG_21	1043	29	31.96	b.d.l.	64.96	b.d.l.	b.d.l.	1499.29	16212.49	634.94
LSG_23	1134	21	32.05	0.0161	64.75	b.d.l.	b.d.l.	1580.39	9206.49	b.d.l.
LSG_25	1485	55	31.33	b.d.l.	65.92	b.d.l.	b.d.l.	954.38	11304.39	578.73
LSG_27	1720	42	31.88	b.d.l.	66.18	b.d.l.	b.d.l.	477.98	13161.46	b.d.l.
LSG_28	1558	25	30.96	b.d.l.	65.05	b.d.l.	b.d.l.	850.44	11141.58	b.d.l.
LSG_30	1181	22	30.55	b.d.l.	65.16	b.d.l.	b.d.l.	1392.98	12023.48	697.29
LSG_31	1058	16	30.45	0.0289	65.39	b.d.l.	b.d.l.	2588.32	10246.96	587.52
LSG_32	1885	58	30.90	0.0856	65.94	b.d.l.	b.d.l.	634.68	13131.78	b.d.l.
LSG_33	1463	54	30.94	0.0427	65.13	b.d.l.	b.d.l.	1747.33	11205.18	718.37
LSG_34	1490	20	31.76	0.0218	65.47	b.d.l.	b.d.l.	1668.59	9499.90	743.84
LSG_36	1858	48	31.95	0.0290	65.78	b.d.l.	b.d.l.	557.51	13487.93	b.d.l.
LSG_37	1837	110	32.10	0.0323	65.81	b.d.l.	b.d.l.	332.30	12408.46	b.d.l.
LSG_38	1672	29	31.71	0.0256	65.74	b.d.l.	b.d.l.	416.56	14771.77	b.d.l.
LSG_39	1052	9	31.60	0.0323	65.65	b.d.l.	b.d.l.	1141.79	13926.34	b.d.l.
LSG_41	1090	11	32.18	0.0344	65.02	b.d.l.	128.89	746.49	18240.00	b.d.l.
LSG_42	1779	16	31.97	0.0412	65.24	b.d.l.	b.d.l.	b.d.l.	13114.82	b.d.l.
LSG_43	1665	29	30.98	0.0243	65.81	b.d.l.	b.d.l.	2033.96	12273.63	499.70
LSG_44	1192	24	31.80	0.0376	65.71	b.d.l.	b.d.l.	952.01	14011.99	b.d.l.
LSG_45	1098	22	31.75	0.0279	65.20	b.d.l.	b.d.l.	980.36	14773.47	620.89
LSG_46	1427	20	31.76	0.0213	65.38	b.d.l.	b.d.l.	2333.18	13857.65	598.05
LSG_47	1100	38	31.90	0.1106	64.86	b.d.l.	b.d.l.	2310.35	9729.70	b.d.l.
LSG_48	1394	73	33.21	0.0260	66.23	b.d.l.	b.d.l.	894.53	11877.63	502.33
LSG_49	1747	34	32.02	0.0403	65.82	b.d.l.	b.d.l.	1767.80	8997.89	570.83
LSG_50	1390	91	31.85	0.0295	65.33	b.d.l.	b.d.l.	618.93	10377.55	b.d.l.
LSG_51	1586	47	31.97	0.0268	66.16	b.d.l.	b.d.l.	413.41	10748.12	b.d.l.
LSG_52	1615	22	31.75	0.0194	65.25	b.d.l.	b.d.l.	1065.41	12968.12	b.d.l.
LSG_53	1068	13	32.29	0.0350	65.76	b.d.l.	b.d.l.	710.27	12234.62	b.d.l.
LSG_54	1120	15	31.96	0.0363	65.93	b.d.l.	b.d.l.	922.88	12977.45	b.d.l.
LSG_55	1527	68	30.83	0.0231	65.90	b.d.l.	b.d.l.	889.81	11186.52	b.d.l.
LSG_56	1612	28	31.06	0.0222	65.64	b.d.l.	b.d.l.	549.63	13578.67	b.d.l.
LSG_57	1448	13	31.28	0.0214	64.67	b.d.l.	b.d.l.	995.32	15060.93	535.70
LSG_58	2547	12	31.41	0.0202	65.15	b.d.l.	b.d.l.	b.d.l.	14007.75	b.d.l.
LSG_59	1556	21	31.33	0.0251	65.17	b.d.l.	b.d.l.	975.64	13464.19	479.50
LSG_60	1901	18	31.83	0.0167	65.82	b.d.l.	b.d.l.	1837.88	13626.16	533.95
LSG_62	1196	48	31.74	0.0204	66.32	b.d.l.	b.d.l.	852.80	13392.96	b.d.l.
LSG_63	1119	29	31.06	0.0233	65.76	b.d.l.	b.d.l.	776.42	13133.48	b.d.l.
LSG_67	1587	21	31.67	0.0190	65.42	b.d.l.	b.d.l.	562.23	12843.47	b.d.l.
LSG_68	1657	20	31.57	b.d.l.	65.82	b.d.l.	b.d.l.	b.d.l.	8538.29	b.d.l.
LSG_69	1685	36	30.80	b.d.l.	65.91	b.d.l.	b.d.l.	632.31	12011.61	b.d.l.
LSG_70	1976	26	31.14	0.0198	65.33	b.d.l.	b.d.l.	762.24	14653.90	b.d.l.
Heavitree Quartzite										
HTQ_1	1714	22	32.13	0.0330	65.99	b.d.l.	b.d.l.	1088.24	10762.53	b.d.l.
HTQ_2	1757	23	31.85	0.0162	66.19	b.d.l.	b.d.l.	369.31	13435.36	b.d.l.
HTQ_3	1144	20	32.05	0.0251	66.15	b.d.l.	b.d.l.	636.25	12431.35	b.d.l.
HTQ_4	1679	23	31.99	0.0272	65.92	b.d.l.	b.d.l.	b.d.l.	12943.53	b.d.l.
HTQ_6	1526	17	32.05	0.0254	65.65	b.d.l.	b.d.l.	405.53	13388.72	b.d.l.
HTQ_7	1526	48	32.03	b.d.l.	66.33	b.d.l.	b.d.l.	978.00	10251.20	b.d.l.
HTQ_8	1619	20	31.62	b.d.l.	65.10	b.d.l.	b.d.l.	645.70	12333.84	b.d.l.
HTQ_9	1603	17	31.62	0.0286	66.48	b.d.l.	b.d.l.	391.36	11620.69	b.d.l.
HTQ_10	1601	25	31.40	b.d.l.	65.83	b.d.l.	b.d.l.	1189.82	12800.22	499.70
HTQ_11	1144	24	31.02	0.0271	63.80	b.d.l.	b.d.l.	971.70	11809.79	b.d.l.
HTQ_12	1778	15	31.72	0.0287	66.06	b.d.l.	b.d.l.	420.49	12716.28	b.d.l.
HTQ_13	1601	27	32.23	0.0180	65.97	b.d.l.	b.d.l.	1303.21	10068.89	b.d.l.
HTQ_14	1761	11	31.83	b.d.l.	65.05	b.d.l.	b.d.l.	1192.18	13547.29	b.d.l.
HTQ_15	1588	21	31.58	b.d.l.	65.43	b.d.l.	b.d.l.	3569.47	10572.59	1055.60
HTQ_16	1807	17	31.41	b.d.l.	64.92	b.d.l.	b.d.l.	509.47	12584.84	b.d.l.
HTQ_17	1668	19	32.16	0.0205	65.96	b.d.l.	b.d.l.	511.05	13046.14	b.d.l.
HTQ_18	1509	26	31.87	0.0241	66.00	b.d.l.	b.d.l.	1115.80	11704.64	b.d.l.
HTQ_19	1583	13	32.07	0.0256	66.10	b.d.l.	b.d.l.	855.16	12379.63	b.d.l.
HTQ_20	1735	10	31.48	0.0190	65.63	b.d.l.	b.d.l.	2081.20	12947.77	629.67
HTQ_22	1595	21	32.24	0.0200	65.72	b.d.l.	b.d.l.	922.88	13384.48	b.d.l.
HTQ_23	1321	18	32.09	0.0160	65.73	b.d.l.	b.d.l.	2320.59	11710.57	574.34
HTQ_24	1592	18	32.00	0.0268	66.06	b.d.l.	b.d.l.	708.70	12255.82	b.d.l.
HTQ_25	1565	25	32.02	0.0224	66.07	b.d.l.	b.d.l.	925.24	12504.28	b.d.l.
HTQ_26	1305	21	32.05	0.0202	66.01	b.d.l.	b.d.l.	352.77	12530.57	b.d.l.
HTQ_27	1584	23	31.24	0.0197	64.10	b.d.l.	b.d.l.	573.26	12929.97	b.d.l.
HTQ_29	1218	14	32.09	0.0255	65.99	b.d.l.	b.d.l.	512.62	12907.07	b.d.l.
HTQ_30	1753	11	32.94	0.0177	63.73	b.d.l.	b.d.l.	2074.90	11046.61	597.18
HTQ_31	1597	21	31.79	0.0179	66.12	b.d.l.	b.d.l.	677.99	12879.09	b.d.l.
HTQ_33	1584	31	30.57	0.0160	65.94	b.d.l.	b.d.l.	794.53	10635.34	b.d.l.
HTQ_34	1590	29	32.10	0.0230	65.66	b.d.l.	b.d.l.	978.00	9914.56	b.d.l.
HTQ_35	1772	20	31.10	0.0330	64.89	b.d.l.	b.d.l.	1981.99	12749.35	623.52
HTQ_36	1618	21	31.97	b.d.l.	65.43	b.d.l.	b.d.l.	1007.92	11470.60	b.d.l.
HTQ_37	1674	13	31.26	0.0236	66.01	b.d.l.	b.d.l.	1408.73	11630.86	546.24
HTQ_38	1583	19	31.45	0.0214	65.92	b.d.l.	b.d.l.	989.81	12067.57	b.d.l.
HTQ_39	2076	10	31.72	0.0242	65.83	b.d.l.	b.d.l.	878.78	11624.93	b.d.l.
HTQ_40	1587	15	31.43	0.0198	66.03	b.d.l.	b.d.l.	672.47	12041.28	b.d.l.
HTQ_41	1640	13	31.61	0.0189	66.01	b.d.l.	b.d.l.	807.91	13609.20	b.d.l.
HTQ_43	1743	18	30.75	0.0164	65.06	b.d.l.	b.d.l.	3182.05	13775.40	1109.17

Grain spot	Inferred age (Ma)	±	SiO_2 (wt%)	Al_2O_3 (wt%)	ZrO_2 (wt%)	CaO (wt%)	Ti (ppm)	Y (ppm)	Hf (ppm)	Yb (ppm)
HTQ_45	1597	16	30.81	0.0247	65.18	b.d.l.	b.d.l.	2338.70	14307.93	562.93
HTQ_46	1765	12	31.14	0.0249	65.94	b.d.l.	b.d.l.	882.72	13144.50	b.d.l.
HTQ_47	1565	24	31.36	0.0344	65.57	b.d.l.	b.d.l.	1643.39	11077.13	560.29
HTQ_49	1585	18	32.00	0.0199	65.74	b.d.l.	b.d.l.	621.29	12562.79	b.d.l.
HTQ_50	1662	18	31.45	0.0246	65.94	b.d.l.	b.d.l.	837.05	12889.26	b.d.l.
HTQ_51	1769	21	31.86	b.d.l.	65.84	b.d.l.	b.d.l.	416.56	10961.81	b.d.l.
HTQ_53	1656	13	31.95	0.0164	65.87	b.d.l.	b.d.l.	716.57	12682.36	b.d.l.
HTQ_54	1679	35	31.19	0.0196	66.21	b.d.l.	b.d.l.	872.48	10698.09	b.d.l.
HTQ_55	1619	36	31.11	0.0154	66.17	b.d.l.	b.d.l.	674.05	12193.92	b.d.l.
HTQ_57	1239	39	31.81	0.0227	66.26	b.d.l.	b.d.l.	1400.07	9407.47	b.d.l.
HTQ_58	1212	21	32.03	0.0178	65.85	b.d.l.	b.d.l.	455.93	12983.39	b.d.l.
HTQ_59	1648	25	32.10	0.0258	65.20	b.d.l.	b.d.l.	716.57	13654.99	b.d.l.
HTQ_60	1138	27	31.80	b.d.l.	66.28	b.d.l.	b.d.l.	528.37	11883.56	b.d.l.
HTQ_61	1751	14	31.75	0.0242	66.03	b.d.l.	b.d.l.	933.90	13553.23	b.d.l.
HTQ_62	1233	19	32.03	0.0257	66.08	b.d.l.	b.d.l.	712.63	12450.01	b.d.l.
HTQ_63	1494	27	32.47	0.0227	66.35	b.d.l.	b.d.l.	826.81	11332.38	b.d.l.
HTQ_64	1721	31	31.63	0.0250	66.06	b.d.l.	b.d.l.	340.17	14037.42	b.d.l.
HTQ_65	1628	20	32.31	b.d.l.	65.78	b.d.l.	b.d.l.	1922.93	10005.29	463.69
HTQ_66	1651	34	32.68	b.d.l.	66.00	b.d.l.	b.d.l.	1300.85	11931.90	b.d.l.

Samples in italics excluded from Lu-Hf isotopic analyses due to small grain size (<50 µm).

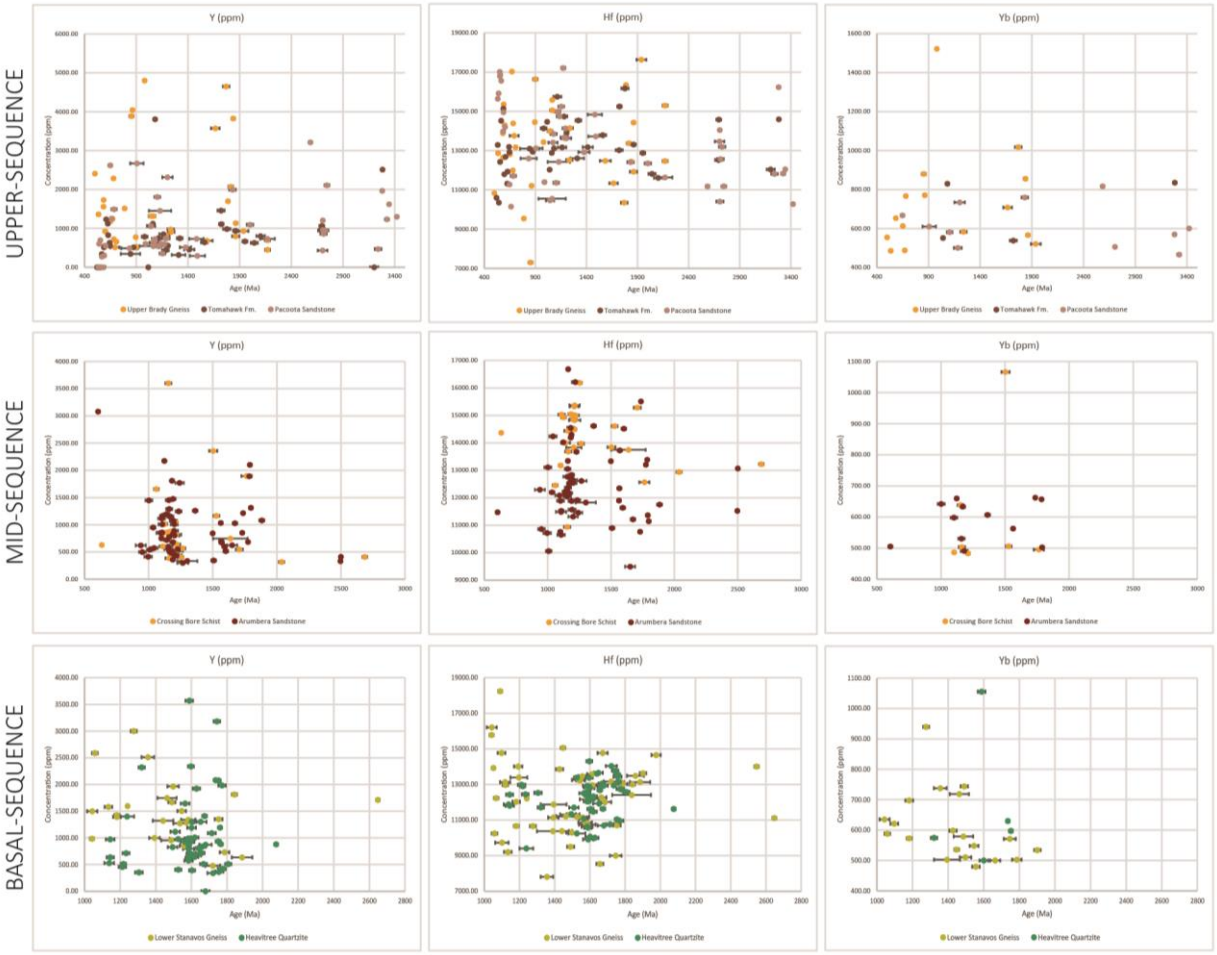

APPENDIX H: THERMOCALC AVERAGE P-T CALCULATIONS

Activities for mineral endmembers were calculated using a representative electron microprobe composition from the interior of each mineral in the equilibrium mineral assemblage of each sample (refer to Appendix X) using software AX 2 (2008 update; Holland & Powell 2000 in Powell & Holland 2002). P-T caluclations were made using the compositions from the interiors of garnets combined with core compositions of matrix minerals away from garnet, to minimise the effects of retrograde re-quilibration. In the metapelite samples, garnet is prograde zoned and therefore near-rim garnet compositions (approximately 1/3 garnet diameter away from rim) were interpreted to reflect more realistic peak metamorphic garnet compositions. Contents of SiO_2, TiO_2, Cr_2O_3, Al_2O_3, FeO, MnO, MgO, CaO, Na_2O and K_2O (as wt% oxides) for each mineral per sample were input into AX 2 as a simple text file using a standard format (Holland & Powell 2000 in Powell & Holland 2002).

For samples BG-07B, BG-08 and UBG-4B, AX 2 was run with a temperature and pressure estimate of 650°C and 6.5 kbar; for the eight mafic granulite samples, input temperature and pressure estimates were 850°C and 9 kbar, based on field observations and petrographic analyses.
Running each sample under the estimated pressure and temperature in AX 2 returns a THERMOCALC-readable output file listing mineral endmember activities and their uncertainties, for rearrangement before direct input into THERMOCALC. Non-solid solution phases also present in each samples' mineral assemblage (i.e. quartz and sillimanite in metapelites, sphene and quartz in mafic granulites) were appended to the rearranged output file assuming activity compositions of 1.0 and uncertainties of 0.0.

Calculation of average P-T conditions was undertaken following the average P-T approaches of Powell and Holland (1994) using the software THERMOCALC v.3.21 (Powell and Holland, 1998; Powell et. al., 1998) with an updated and expanded version of the internally consistent thermodynamic dataset (19 Sept 1999 update) of Holland and Powell (1998). The average P-T method involves using a least-squares method to determine the optimal P-T from the thermodynamics of the reactions in an independent set, including uncertainties and correlations on the activities and enthalpies of formation of the end-members (Holland & Powell 1994). The average P-T is dependent on the calculated and input activity uncertainties.
THERMOCALC was run initially under the average-P mode to calculate an average pressure estimate for a series of pre-defined temperatures in the specified likely temperature range of formation of the rock. This provides an average pressure locus with such calculations being more robust than for the final average P-T determination as only one variable is being solved for and without iteration. Similarly, an average-T estimate was also calculated, followed by the average P-T calculation.

User-specified model parameters for temperature and pressure utilized under each mode for the metapelites and mafic granulites are detailed below. For each sample, the rock was assumed to be non-fluid bearing and utilized the recommended value of 1.0 (Holland & Powell 1998) for the allowed angle change of reaction per kbar (i.e. only linear reactions allowable within the designated P-T space).

Dependence of the average-P, average-T and average P-T result on fluid composition was investigated by systematic variation of the input fluid activity value (aH_2O) within the range 0.1 - 0.9 for all samples. Values of 0.4 and 0.8 were used for mafic granulite and metapelite samples, respectively. The prescence of leucosomes suggests that fluid-absent partial melting prevailed, typically associated with low aH2O, however higher values were selected due to occurrence of relatively hydrous hornblende- and mica-rich mineral assemblages, respectively. The value selected for metapelite samples also resulted in the most realistic temperature estimate (>650ºC) as suggested by the presecence of leucosomes. Since the metapelite samples were also sampled from a inferred stratigraphic higher interval of the Harts Range Group (Maidment et al. 2013), it is plausible that their water activity is also higher than for the mafic granulites at lower crustal depths.

The output value of σ_{fit}, a measure of the scatter in residuals (observed – calculated values) of the enthalpies and activities normalized by their uncertainties, provides an indication of whether the calculated average P-T was consistent with the input data and whether the result can be accepted at a 95% confidence interval. The maximum allowable σ_{fit} is dependent upon the degrees of freedom for the problem (the difference between the number of independent reactions and the number of unknowns). If the value of σ_{fit} is less than the specified maximum allowable cut-off value from the χ^2 test at the 95% confidence level, then the χ^2 test has been passed, indicating that a solution for P-T has been found that is consistent with the input within their uncertainties. Endmembers occurring as significant outliers were omitted from further calculations with the removal of these outliers improving the significant fit of the determined P-T result to pass at 95% confidence if the χ^2 test had failed previously (Powell & Holland 1994). Endmembers were identifiable by noting individual endmember

values of P, T and fit, which were significantly different from the overall average P-T result. The hat value, *h*, for each endmember is direct measure of the degree of influence of that endmember on the least squares result with endmembers having a large value (on a scale of 0-1) having a controlling influence that pertubates in the activities to large changes in the final average P-T. This diagnostic is also examined with the activity residual which is normalized to the uncertainty on the measured activity and denoted as e*. The activity residual is the difference between the measured activity of an endmember based on mineral analysis in a rock and the calculated activity required for all the equilibria to intersect at the average P-T. Large values indicate that the corresponding activities are not being well fitted.
In the majority of samples used in this study ≥ 7 independent reactions were used during the average P-T calculations. In particularily low variance assemblages up to 10 independent reactions could be found. No outlier endmembers were removed from the three Brady Gneiss samples and one outlier was removed from all mafic granulite analyses.

An example output from a THERMOCALC average P-T calculation is shown below.

Example THERMOCALC output from average P-T calculations: Sample IG-28A

THERMOCALC v3.21 running at 14.21 on Mon 7 Oct, 2013

an independent set of reactions has been calculated

Activities and their uncertainties

	di	hed	cats	py	gr	alm	tr
a	0.630	0.360	0.0560	0.0141	0.0290	0.120	0.0198
sd(a)/a	0.05079	0.10000	0.26734	0.51767	0.43194	0.23112	0.47891

	fact	ts	an	q	H2O
a	0.00490	0.00200	0.540	1.00	0.400
sd(a)/a	0.64319	0.75926	0.20000	0	

Independent set of reactions
1) cats + q = an
2) py + 2gr = 3di + 3cats
3) 2gr + alm + 3q = 3hed + 3an
4) 2di + ts = 2cats + tr
5) 3gr + 2ts + 5q = 6di + 7an + 2H2O
6) 10gr + 5alm + 3tr + 15q = 15di + 3fact + 15an

Calculations for the independent set of reactions (for a(H2O) = 0.4)

	P(T)	sd(P)	a	sd(a)	b	c	ln_K	sd(ln_K)
1	12.0	2.36	-18.75	0.23	-0.01626	1.322	2.266	0.334
2	10.0	4.57	53.95	0.91	-0.08260	2.655	1.309	1.296
3	11.4	1.53	51.85	2.11	-0.15240	6.981	4.288	1.118
4	11.2	67.89	24.76	2.16	0.00061	-0.148	-2.548	1.050
5	11.6	2.08	155.12	4.42	-0.38625	11.210	15.965	2.457
6	10.0	1.58	339.39	6.70	-0.82920	35.295	25.643	5.946

Average PT (for a(H2O) = 0.4)
Single end-member diagnostic information

avP, avT, sd's, cor, fit are result of doubling the uncertainty on ln a :
a ln a suspect if any are v different from lsq values.
e* are ln a residuals normalised to ln a uncertainties :
large absolute values, say >2.5, point to suspect info.
hat are the diagonal elements of the hat matrix :
large values, say >0.50, point to influential data.
For 95% confidence, fit (= sd(fit)) < 1.54
however a larger value may be OK - look at the diagnostics!

	avP	sd	avT	sd	cor	fit
lsq	10.3	1.5	837	64	0.236	1.10

	P	sd(P)	T	sd(T)	cor	fit	e*	hat
di	10.30	1.47	836	67	0.268	1.10	0.06	0.04
hed	10.25	1.32	848	59	0.223	0.99	-0.82	0.03
cats	10.10	1.44	826	64	0.290	1.06	0.63	0.12
py	10.23	1.51	829	74	0.338	1.10	0.19	0.29
gr	10.07	1.64	848	74	-0.066	1.09	0.25	0.48
alm	10.58	1.46	833	62	0.195	1.06	-0.44	0.07
tr	10.15	1.54	825	75	0.376	1.09	-0.28	0.32
fact	11.07	1.38	845	59	0.249	0.65	1.79	0.10
ts	10.34	1.45	840	67	0.253	1.10	0.18	0.10
an	9.65	1.91	838	62	0.159	1.07	-0.38	0.42
q	10.32	1.45	837	64	0.236	1.10	0	0
H2O	10.32	1.45	837	64	0.236	1.10	0	0

T = 837°C, sd = 64,
P = 10.3 kbars, sd = 1.5, cor = 0.236, sigfit = 1.10

APPENDIX I: MULTIDIMENSIONAL SCALING (MDS)

Multidimensional Scaling (MDS) has been undertaken following the guidelines of Vermeesch (2013) using the provided MATLAB software tools and input files downloaded from http://mudisc.london-geochron.com. Pairwise dissimilarities between samples produce a MDS 'map' of points in multidimensional dissimilarity-space in which samples with similar datasets cluster and dissimilar samples plot father apart. Vermeesch (2013) employs the Kolmogorov-Smirnov (K-S) sample effect size as an effective measure of statistically significant dissimilarity between two populations. In the context of the detrital zircon ages, the 'sample effect size' of the K-S test is the maximum difference between two empirical cumulative distribution functions of the two observed age populations (ECDFs; Vermeech 2013, Satoski, 2013).
The axes of MDS plots are dimensionless as 'K-S' units of distance ($0 < K\text{-}S < 1$) between samples, and the orientation is arbitrary.

MDS attempts to find the best spatial configuration of points such that a stress-parameter (S) is minimised. Kruskal's Stress criterion is used to evaluate the degree of correspondence between original calculated K-S 'distances' from the input dissimilarity matrix, and those which are predicted (or reproduced) by the MDS configuration (denoted as 'dissimilarities') which are plotted as the axes of corresponding Shephard Plots. Rules for interpreting the goodness of fit using the final value of Kruskal (1964)'s Stress-1 (S) value are given below. The 'stress' is a dimensionless number and can be expressed as a percentage.

Narrow scatter of data points in Shephard Plots about a 1:1 line as reflected by stress approaching zero, indicates that the input proximities and reproduced well by the MDS model while large scatter or non-linear fit and a large stress implies a lack of fit. If the fit of the Shephard Plot is poor then the distances in the MDS configuration are not a reliable indication of the actual sample dissimilarities. For example, large interpoint distances in the MDS representation may therefore not necessarily correspond to larg dissimilarities between samples, and likewise small interpoint distances may not reflect small dissimilarities.

Goodness of fit	Poor	Fair	Good	Excellent	Perfect
S	0.2	0.1	0.05	0.025	0

Metric MDS creates a configuration of points such that the output MDS interpoint distances diretly approximate the original input dissimilarities. In nonmetric MDS, the original dissimilarities are not recreated; nonmetric MDS attempts only to approximate the *relative 'ranks'* of the dissimilarities. Alternatively, nonmetric MDS creates a configuration of points whose interpoint distances approximate a nonlinear *monotonic transformation* of the original dissimilarities. For nonmetric MDS, monotonicity between dissimilarity and distance is ideal with a smaller value of S accordingly corresponding to better monotonicity beween interpoint distances and the experimentally derived rank order of pairwise dissimilarities. Due to the monotonicity, larger or smaller distances on nonmetric MDS correspond to larger or smaller dissimilarities, respectively, however the the model only preserves the ordering of the dissimilarities and consequenty only the *relative*, not absolute, interpoint distances should be considered when interpreting the visualisation. Nonmetric MDS and Shephard plots are provided below for the dataset discussed in-text using metric MDS methods.

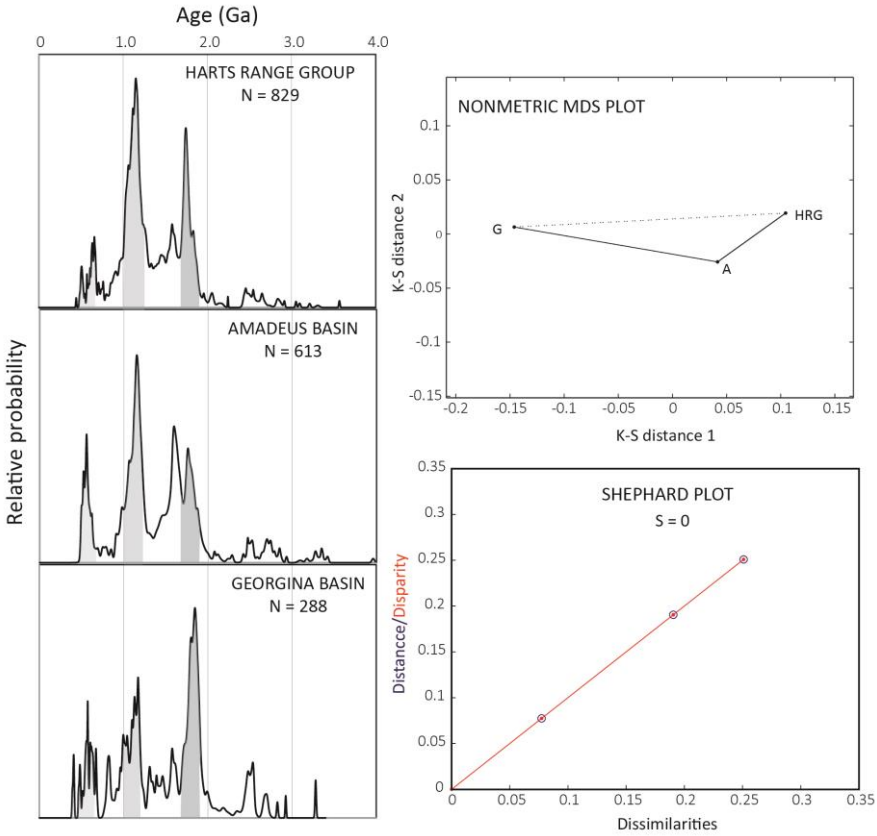
Age (Ga)
0
1.0
2.0
3.0
4.0
HARTS RANGE GROUP
N = 829
AMADEUS BASIN
N = 613
GEORGINA BASIN
N = 288
Relative probability
NONMETRIC MDS PLOT
G
HRG
A
K-S distance 2
K-S distance 1
SHEPHARD PLOT
S = 0
Distancce/Disparity
Dissimilarities

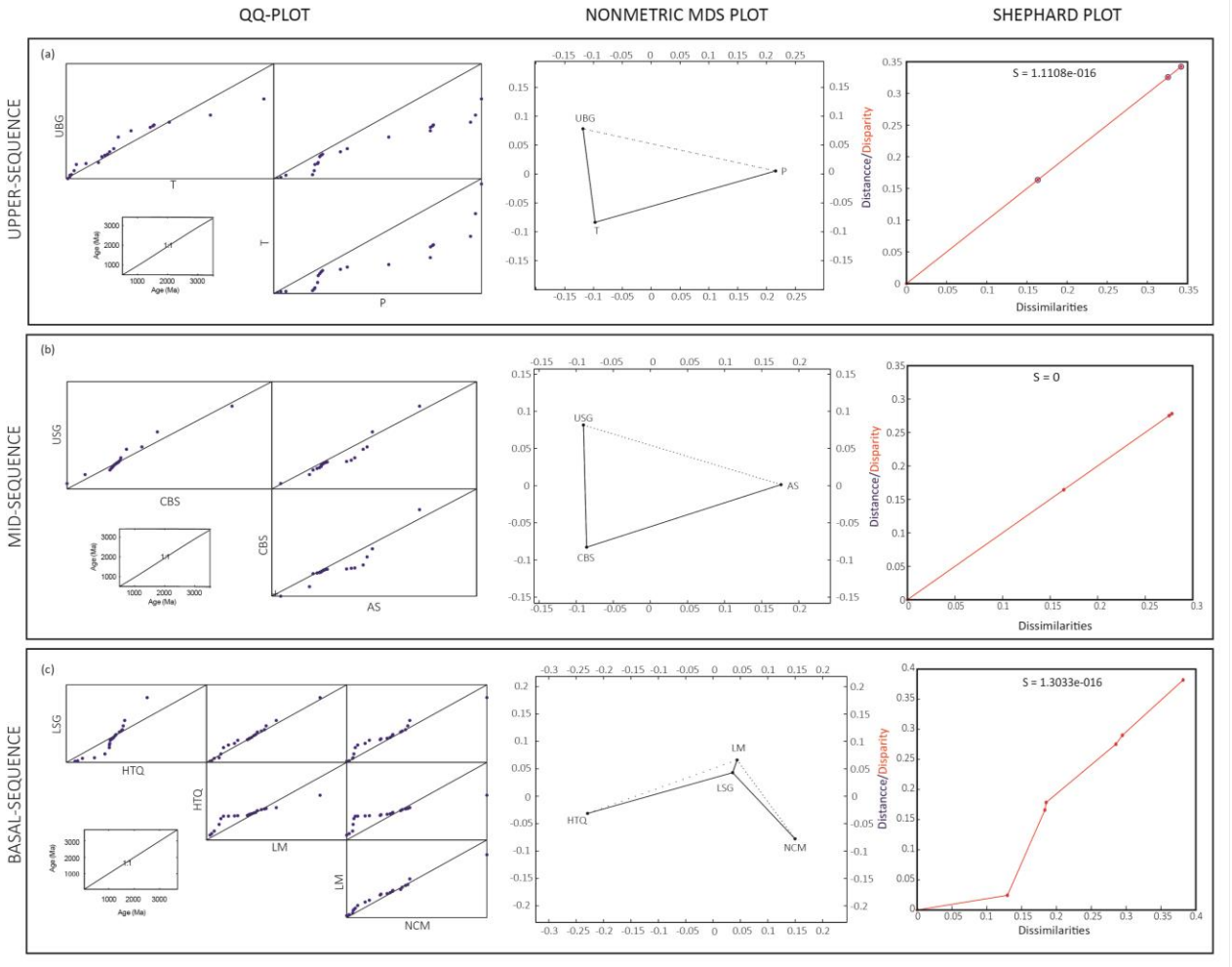
QQ-PLOT
NONMETRIC MDS PLOT
SHEPHARD PLOT
UPPER-SEQUENCE
(a)
UBG
T
P
S = 1.1108e-016
MID-SEQUENCE
(b)
USG
CBS
AS
S = 0
BASAL-SEQUENCE
(c)
LSG
HTQ
LM
NCM
S = 1.3033e-016
Distancce/Disparity
Dissimilarities
Age (Ma)

APPENDIX J: EXTENDED ANALYTICAL METHODS

Zircon major and trace element chemistry

Zircon major and trace element analyses on all zircon samples were performed on a CAMECA SXFive electron microprobe at Adelaide Microscopy, University of Adelaide. Analysis locations were placed as close as possible to concordant SHRIMP spot localities within the same CL zones. Analyses were conducted for CaO, Al_2O_3, SiO_2, ZrO_2, HfO_2, Y_2O_3, Yb_2O_3, and Nb_2O_3 on wavelength dispersive spectrometers, using an accelerating voltage of 20 kV, a beam current of 50 nA and a spot size of 5 µm for all analyses, and a PAP correction was applied to all data. Trace element data are reported as ppm and major elements as wt% oxides. Typical detection limits for trace elements Hf, Yb, Y, Zr, and Ti were 381 ppm, 460 ppm, 286 ppm, 463 ppm and 83 ppm, respectively. All Nb analyses were below detection limit (typically 465 ppm) and have accordingly been excluded from Table X. Typical detection limits for major elements were Si (0.0113%), Al (0.0149%) and Ca (0.0116%). Data from elemental analyses is provided in Appemdix J.

Whole-rock geochemistry

Rock samples were initially trimmed of weathered surfaces using a rock saw, cut into smaller fragments, washed and then dried at low temperature (< 100°C) on a hot plate. Clean, fresh fragments of whole-rock samples were crushed to centimetre-sized fragments using a customized mechanical jaw crusher that is disassembled and thoroughly cleaned with compressed air and ethanol prior to the processing of each sample. The resulting rock fragments are ground in a low-chromium steel ring WC-mill, which is also cleaned prior to use, for approximately three minutes to a fine powder (~3 µm particle size).

Whole-rock geochemical analyses of major and trace elements by Wavelength Dispersive X-ray Fluorescence (WD-XRF) spectrometry were undertaken at the Earth and Environmental Department, Franklin and Marshall College, Lancaster PA. Major and trace elements were analysed using a Philips 2404 XRF vacuum spectrometer equipped with a 4kW Rh X-ray tube following the standard analytical procedures described in Mertzman (2000). XRF analysis for both major and trace element concentrations utilised geochemical rock standards which were prepared in an identical manner to the unknowns, analyses of which were run with the unknown samples to monitor instrument performance.

Loss on ignition (LOI) determination

Prior to preparation of XRF major element disks, loss on ignition (LOI) was determined for each sample, for correction by loss of volatile compounds such as water and organic matter during heating. Approximately 1.0000 g of finely ground sample powder is weighed into a previously weighed, clean and dry porcelain crucible with the total weight of the crucible and sample also then recorded. A maximum of 10 samples may be prepared for one batch. Crucibles were placed into a pre-heated muffle furnace for 60 mins at 900-950°C. After cooling, the weight of the samples before heating less weight after heating was recorded as the initial loss on ignition and is reported as a percent loss. A loss of weight results in a positive value; a negative value corresponds to a gain in weight. Heated LOI sample material is used for subsequent major element analysis since heating reduces organic matter, water and sulphide structures which may otherwise cause interference with the analysis of major elements. The LOI material was placed into a desiccator until required to prevent exposure to moisture.
Each crucible is emptied, cleaned and rinsed with acetone, air-dried and then further dried in a furnace for a few minutes. Chemical waste from this procedure is considered hazardous and is collected for appropriate disposal.

Major element analysis

Major elements were analysed on fused disks using a lithium tetraborate flux. The fusion technique is described briefly. Crushed rock powder (0.4000 ± 0.0001 g of previously heated LOI sample) combined with lithium tetraborate (3.6000 ± 0.0002 g) is mixed gently in a clean glass bottle by rotation by hand, and then for 10 minutes in a Spex Mixer Mill. The homogeneous powder is transferred into a clean 25 cc. 95% Pt-5% Au crucible with 3 drops of a 2% solution of lithium iodide (Lil) to lower the viscosity of the material, and then heated with a Meeker burner until molten whilst mounted on a ring-stand for approximately 10 minutes. During the heating period the sample is swirled vigorously after three and six minutes to remove air bubbles and to homogenise the molten sample. Whilst the sample is not stirred, the crucible is covered with a 95% Pt-5% Au lid which also doubles as the casting dish into which the molten sample is poured and quenched. After sufficient

heating, the Pt-lid is removed from the crucible and itself heated over a bunsen burner until red-hot. The crucible is removed rapidly from the ring-stand and the contents are emptied onto the hot Pt-lid. The emptied hot crucible is immediately dropped into a warmed beaker containing sufficient amount of HCl (4M) to cover the crucible. The lid is allowed to cool for three to five minutes on a flat surface to produce a homogenous glass disc. The flat side of the disc in contact with the Pt lid is used for XRF analysis of the following major element oxides: SiO_2, Al_2O_3, Fe_2O_3, MnO, K_2O, Na_2O, TiO_2, P_2O_5, CaO and MgO.

Iron content determination – ferrous iron titration techniques

FeO contents were analysed by ferrous (Fe^{2+}) iron titration. Sample powder (0.5000 ± 0.0002 g) is placed into a large alumina crucible and covered. Up to 11 samples and one standard geochemical sample may be analysed at any given time. Deionised water (5 ml), concentrated sulphuric acid (5 mL) and hydrofluoric acid (5 ml) are placed into each alumina crucible using a pipette, covered immediately and heated over a Meeker burner until boiling. The covered crucible is moved to a warmed hot plate and left to stand for 10 minutes. Boric acid solution (450 ml), prepared in a 15 L batch from boric acid (50 g), phosphoric acid (65 ml) and sulphuric acid (100 mL) for each 5 L of distilled water, is combined with 3-5 drops of a 3.0% indicator solution of sodium diphenyamine sulfonate. The heated crucible is lowered and tilted into the boric acid solution so that it is completely covered by the solution as quickly as possible whilst minimising contact between the tongs and boric acid solution. The solution is promptly titrated with a 2.730 g/L standard solution of potassium chromate ($K_2Cr_2O_7$) to a purple end point.

Trace element analysis

Total contents of trace elements Rb, Sr, Y, Zr, V, Ni, Cr, Nb, Ga, Cu, Zn, Co, Ba, La, Ce, U, Th, Sc and Pb are reported in ppm and were determined from analysis of a pressed powder briquette. Sample preparation for trace element analysis is accomplished by mixing whole-rock powder (7.0000 g ± 0.0004) and high purity copolywax powder (1.4000 g ± 0.0002) using the same mixing procedure outlined for XRF major element preparation to ensure the sample and powder are thoroughly homogenised. Using a pressing machine, the homogenous powder was pressed at approximately 40,000 psi for about three minutes. The pressed briquette is cleaned with compressed air of which either side can be analysed. Prior to all analysis, all XRF major element glass discs and trace element pellets are stored in a desicator to prevent hydration and accordingly mass changes from hydration.

Detection limits

Detection limits for all major elements were < 0.01 wt% with Mn, Ca and K having detection limits of 0.001 wt%. The detection limit for the trace element Ba was typically 3-5ppm, for trace elements Rb, Sr, Y, Zr, Nb and Ga was 0.5 ppm, and for U, Th, Cu, Zn, Pb, Cr and Ni was within 0.5-1 ppm. Results of geochemical analyses are provided in Appendix X. Details regarding sample preparation and analyses methods are described as follows.

Sequential (petrographic) thin section preparation

Rock samples were initially trimmed of weathered material and cleaned of organic matter, and cut into small slabs approximately 25mm x 55mm x 8mm, using a 250 mm diameter rock-cutting saw blade with a continuous diamond rim. The rock specimen is pushed into the spinning blade with a slow, even pressure whilst water supplied to the blade completely bathes the sample for maximum lubrication and cooling. Moist, cut samples are dried at a low temperature (<100°C) on a hot plate. Rocks which are altered, badly weathered, contain a high clay content or show a tendency to fracture during cutting are impregnated with epoxy resin (Epo-tek 301 2-part epoxy) on a hot plate prior to cutting. The epoxy is left to set for a minimum 24 hours before cutting.

Subsequent sample preparation was undertaken by Pontifex & Associated Pty Ltd. *Pontifex Petrographic Services*, Adelaide. The surface of the slab to be stuck onto a glass slide was manually ground flat on a bench-mounted, horizontal diamond grinding wheel Habit-brand using a grit size of 64. This coarse ground top surface is warmed to 50°C on a hot plate and is then surface coated with an epoxy mix of Araldite LC191 resin with HY951 hardener in a ratio of 8:1. The surface is manually ground flat using a finer 600 SiC grit on a zinc-lap or glass plate using water as a lubricant. This flat finely ground surface is cleaned and inspected. A second veneer of epoxy is applied if open pore spaces are noted. This surface is glued onto a clean, dry glass slide using a UV curing cyanoacrylate liquid adhesive “Locite Impriv 36331” and ground to a known thickness. Exposure to UV

light of the glued interface through the back of the glass slide cures the adhesive in 2 to 3 minutes. This is a permanent bond, and the rock wafer can never be separated from the glass slide.
The rock slab mounted on glass is cut to a thickness of approximately 1mm using a trim saw with a thin continuous diamond rimmed sawblade (Diatrenn E2-G). The slab is further reduced to a wafer of about 120 micron (0.12 mm) on a diamond wheel (Habit D76) held within a special jig attachment by vacuum using water as a lubricant.
The rock slide is loaded into and held in place on the face of a jig and lapped flat on a Logitech machine to a final petrographic thickness of 30 micron using a 600 SiC grit as the grinding abrasive, and water as a lubricant. The quality of the rock wafer is assessed also optically checked for the required 30 micron thickness.
Prepared thin sections were manually polished to a shiny finish at the University of Adelaide to enhance optics and yield a greatly increased resolution. Polishing was undertaken using a soft Struers DP-44 cloth lap using a combination of alumia slurry (using 600-grit alumina) and Kemet 3 µm-grit diamond compound polishing abrasives, using water as the lubricant. Periodically the slide was rotated 180° and additional alumina slurry and water added, until the minerals exhibited an oily appearance, at which point the slide was polished to a shiny finish using the Kemet 3 µm-grit diamond polishing compound.

Elemental garnet x-ray mapping preparation

Garnet grains were removed from fresh surfaces of whole rock samples using an engraving tool taking care not to damage the individual grains. Garnets were then washed and dried. Double-sided tape (approximately 7 cm width) was stuck onto a large glass slide taking care to prevent air pockets forming. The inside of rubber moulds are sprayed using a Kemet premium silicone mold release spray and are pressed onto the tape to create an imprint of the mould outline. Individual grains are placed onto the tape within the bounds of the mould outline, and the moulds then placed back onto the tape in their previously designated positions. A mixture of epoxy and epoxy hardener in a ratio of 5:1 (by weight) is mixed slowly, taking care to prevent formation of air bubbles. In the instance of air bubbles forming, the mixture is placed into a 100°C oven for a short time and stirred again. The epoxy is poured slowly into the centre of the mould to a thickness of about 3 cm. A weight is placed on top of each mould to prevent leakage and the mounts are left to set in a warm, dry place. The moulds are removed after approximately 24 hours, or when the top of the epoxy mount feels firm. After a minimum of 36 hours the set mounts are removed from the slide using a blade, and the tape removed. Approximately 5 mm of the top surface of the mount was cut away using a rock-cutting Gemmasta diamond saw, using water as the lubricant. Grains held within epoxy were cross-sectioned by sequential grinding of the top surface using a Gemmasta diamond grinder to approximately half size, followed by 800-, 1000- and 2400-grit sandpaper laps, and polished to a shiny finish using a Kemet 3 µm-grit diamond compound polishing abrasive on a Struers DP-44 cloth lap for 10 minutes. At each stage, the grains were examined under transmitted light to inspect whether scratches from the previous polishing step had been reduced. Mounts were polished manually by grinding against the direction of rotation from the centre to the edge of the lap, turning the mount 90° periodically to ensure an even polish.